# ABSTRACT


| | |
|---|---|
| Title of Dissertation: | Effects of Rest Time and Temperature on Graphite/$LiCoO_2$ Battery Degradation |
| | Saurabh Saxena, Doctor of Philosophy, 2020 |
| Dissertation directed by: | Professor Michael Pecht, Department of Mechanical Engineering |



Lithium-ion batteries are used as energy storage devices in a variety of applications ranging from small portable electronics to high-energy/high-power electric vehicles. These batteries degrade and lose their capacity, defined as the amount of charge the battery holds, as a result of charge–discharge operations and various degradation mechanisms. Degradation of lithium-ion batteries is affected by various operational and environmental conditions, including temperature, discharge and charge current, and depth of discharge. Another factor, which has not been given due attention, is the open rest period after full charge during the cycling operation of the batteries. This study investigates the effects of open rest period after full charge on the performance degradation behavior of graphite/$LiCoO_2$ pouch batteries under four different ambient temperatures. Battery degradation is quantified in terms of the capacity fade and shifts in the peaks of the differential voltage curves, which also provide inferences about the individual electrode degradation. The interplay between rest time, battery

state of charge, and number of cycles is investigated to explain the capacity fade trends. A capacity fade trend model is then developed and applied to the experimental data, and the applicability of rest time as an accelerating stress factor for Li-ion battery testing is presented. The degradation mechanisms are investigated using differential voltage analysis, X-ray diffraction, scanning electron microscopy, and energy dispersive X-ray spectroscopy techniques.

# EFFECTS OF REST TIME AND TEMPERATURE ON GRAPHITE/$LICOO_2$ BATTERY DEGRADATION

by

Saurabh Saxena

Dissertation submitted to the Faculty of the Graduate School of the
University of Maryland, College Park, in partial fulfillment
of the requirements for the degree of
Doctor of Philosophy
2020

Advisory Committee:
Professor Michael Pecht, Chair
Professor Eric Wachsman
Professor Abhijit Dasgupta
Professor Peter Sandborn
Professor Mark Fuge

# Acknowledgements

I would like to take this opportunity to, first and foremost, thank my advisor Prof. Michael Pecht for his constant support and guidance throughout my doctoral journey.

I can't thank enough my late grandmother, grandfather, parents, siblings, uncle, and aunts, who always supported my decisions and motivated me to strive for the best in life. I thank my flat mates and friends in the United States and friends in India for keeping my social life alive.

I am extremely grateful to my committee members for their comments in improving my dissertation work and for providing me their valuable time. I would also like to express my gratitude to Dr. Michael Azarian, Dr. Michael Osterman, Dr. Diganta Das, Dr. Yinjiao Xing, Dr. Robert Utter, Cheryl, fellow graduate students, and visiting students and scientists at CALCE for their extensive support, help, and feedback on my research.

I would also like to thank the more than 150 companies and organizations that support research activities at the Center for Advanced Life Cycle Engineering (CALCE) at the University of Maryland annually. I would also like to express my gratitude to Timothy Diethrich and Dr. Peter Zavalij of X-ray Crystallographic Center at Department of Chemistry & Biochemistry, University of Maryland, College Park for offering their lab services for conducting the XRD tests, for their guidance, and for Rietveld refinement analysis.

# Table of Contents

# Chapter 1: Introduction

A battery is an electrochemical device which stores electrical energy in the form of chemical energy and supplies the electrical current when a load is connected across its terminals. The earliest examples of battery date back to 1800 when Italian physicist Alessandro Volta built and introduced the first electrochemical battery, the Voltaic Pile [1]. Since then, many battery chemistries and technologies have been developed and commercialized, which can be classified into two types: primary (non-rechargeable) and secondary (rechargeable) batteries.

Primary batteries are one-time-use batteries which cannot be recharged due to the irreversibility of their intrinsic electrochemical reactions. These batteries are used in variety of applications including wrist watches, calculators, toys, flashlights, radios, and many medical devices. Some popular types of primary batteries include alkaline batteries and lithium batteries. Secondary batteries can be recharged multiple times and hence they can facilitate a reversible transformation between chemical energy and electrical energy. Lead-acid, Nickle Cadmium (NiCd), Nickle Metal Hydride (Ni-MH), and Lithium-ion (Li-ion) are well known secondary batteries.

Since their commercialization in 1991, Lithium-ion batteries continue to penetrate deeper into consumer electronic markets and find new application markets including automotive, renewable energy storage and aerospace due to their higher energy and power density. The market for lithium-ion battery is expected to register a compound annual growth rate (CAGR)

of approximately 22%, during the forecast period (2019-2024) [2]. The increasing demand is also favored by the continuous decline in battery prices. The volume weighted average battery pack fell 85% from 2010-18, reaching an average of $176/kWh [3].

The Li-ion chemistry is based on the transport of $Li^+$ ion between negative and positive electrodes in a non-aqueous electrolyte solution. In the past two decades many electrode and electrolyte (lithium salt and solvent) materials have been developed for Li-ion chemistry. Graphite is the most widely used negative electrode material due to its high theoretical specific capacity of 372 $mAhg^{-1}$ and ability to intercalate lithium within its layers with just 9-10% volume change resulting in good mechanical stability. One of the most common positive electrode materials used in Li-ion batteries is $LiCoO_2$ (LCO) which offers high theoretical specific capacity of 274 mAhg−1, high discharge voltage, and good cycling performance. Lithium cobalt oxide (LCO) batteries are one of the most used batteries in a range of portable electronic applications including mobile phones, laptops, and digital cameras. LCO dominated the global lithium-ion battery market share in 2018 [4].

The two electrodes in the Li-ion battery are porous in nature and provide sites within their crystal structures for housing the Li-ions, a process known as intercalation. These electrodes exhibit different chemical potentials depending upon the amount of lithium and participate in redox reactions (Equations (1.1-1.2)) during battery charge and discharge operations. The difference of chemical potentials of the two electrodes result into the overall battery terminal voltage. The two electrodes are glued on two current collectors with the help of binder materials. Poly vinyl difluoride (PVDF) is one of the popular binder materials in Li-ion batteries. A conductive agent such as carbon black is also added to electrodes in small amount to increase the overall electrode conductivity. The negative and positive current collectors are made of copper (Cu) and aluminum (Al), respectively. The current collectors are connected to external battery terminals through welded metallic tabs.

**Negative Electrode (graphite):**

$$Li_xC_6 \underset{\text{Charge}}{\overset{\text{Discharge}}{\leftrightarrow}} C_6 + xLi^+ + xe^- \quad (1.1)$$

**Positive Electrode (lithium cobalt oxide):**

$$Li_{1-x}CoO_2 + xLi^+ + xe^- \underset{\text{Charge}}{\overset{\text{Discharge}}{\leftrightarrow}} LiCoO_2 \quad (1.2)$$

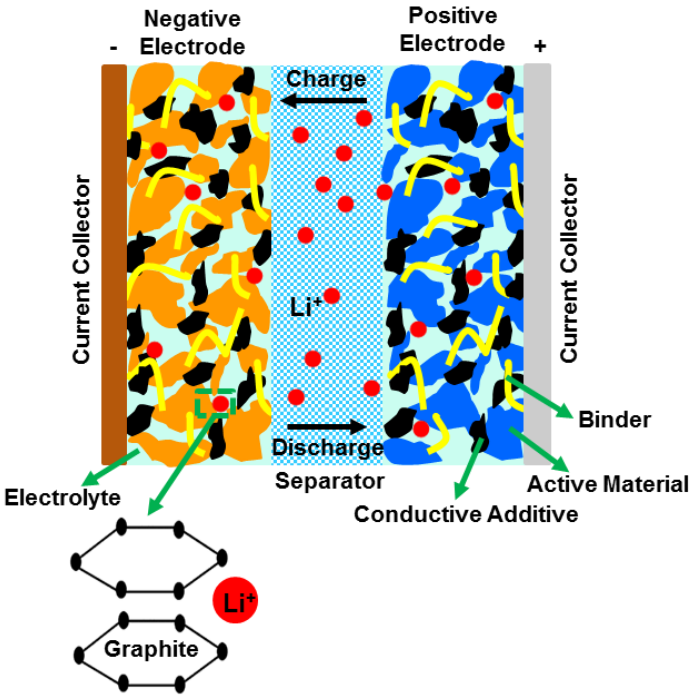


**Figure 1.1.** Schematic of a Li-ion battery.

The separator is usually made of a porous polymeric material such as polyethylene and polypropylene and is in the middle of the two electrodes. It provides electrical insulation between the negative and positive electrode but at the same time allows the transportation of

$Li^+$ ions through its pores. The separator remains soaked into liquid electrolyte. The electrolyte is usually a mixture of organic solvents such as ethylene carbonate and dimethyl carbonates (EC:DMC) and lithium salts such as lithium hexafluorophosphate ($LiPF_6$). The electrolyte serves as a transport medium for the $Li^+$ ions to travel between the two electrodes. The entire cell structure can be stacked, rolled, or wound and put in a cell housing to produce batteries in different geometries and form factors including coin, prismatic, pouch and cylindrical batteries. Figure 1.1 shows the internal schematic of a Li-ion battery.

During the charge operation, electrical energy is supplied to battery using external power source. The electrons from external power source combine with Li+ ions at negative electrode, which reach there from the positive electrode. During discharge operation Li+ ions from negative electrode travel back to positive electrode and combine with the electrons (Equations (1.1) - (1.2)). Battery supplies electrical energy to external load during the discharge operation.

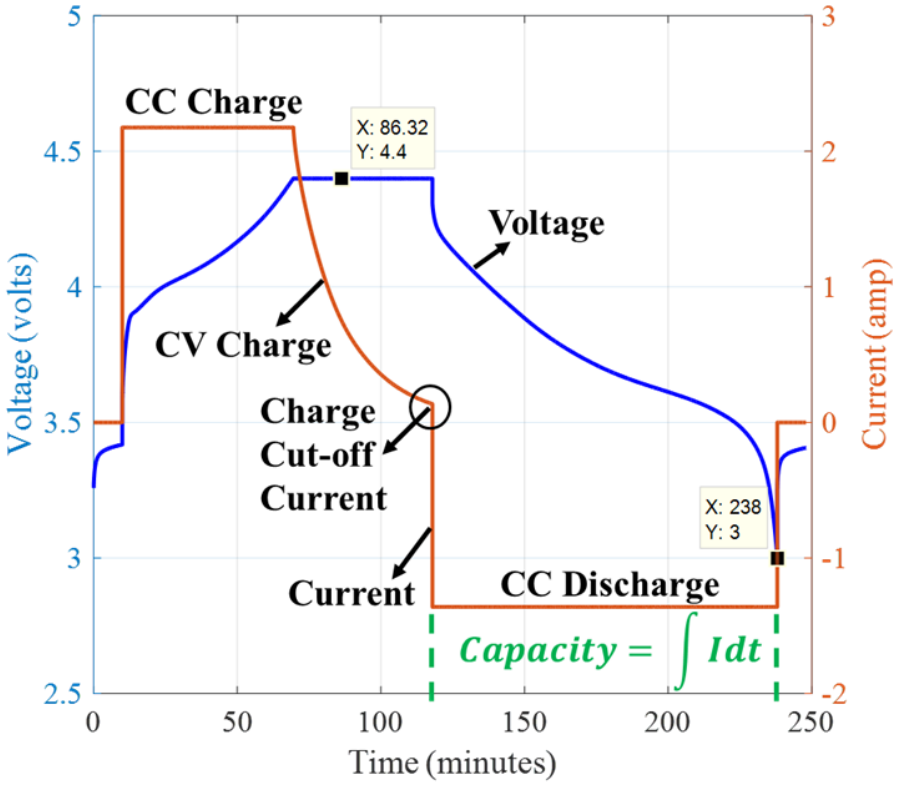


**Figure 1.2.** Full charge-discharge cycle (4.4V –3V) of a battery to calculate the capacity.

The batteries are usually rated in terms of their electrical parameters such as capacity, voltage and impedance. The battery capacity is the total amount of charge (Amp-hours) available when the battery is discharged at a certain current from a prescribed end-of-charge voltage to a prescribed end-of-discharge voltage. Capacity is not directly measurable and can only be calculated by conducting a full charge – discharge cycle on a battery (Figure 1.2). Batteries are usually charged using a standard constant current constant voltage profile. In this profile the battery is charged using prescribed constant charge C-rate[1] up to the end-of-charge voltage followed by the 'top-up' using constant voltage charging until the charging current drops below the prescribed charge cut-off current. Once the battery is fully charged, it is discharged at a prescribed constant C-rate until the end-of-discharge voltage. Capacity can be calculated by multiplying the discharge current (in Amps) with the total discharge time (in hours). Capacity is an important indicator of the amount of energy stored in a battery. For each Li-ion battery depending upon its electrode chemistry, battery manufacturers specify an end-of-charge voltage (usually 4.4V, 4.2V or 3.6V) and an end-of-discharge voltage (usually 3.0V, 2.75V or 2.5V). These voltage limits are driven by the safety considerations to prevent overcharge and overdischarge of the battery.

Battery performance parameters such as capacity and impedances change over time due to various degradation mechanisms such as solid electrolyte interphase (SEI) layer formation and growth, electrode particle cracking, electrolyte decomposition, and lithium deposition [5]–[8]. Battery failure is usually defined in terms of certain thresholds related to battery capacity or impedance changes. For example, 20% reduction in battery initial capacity is considered as

[1] The battery current is usually expressed in terms of C-rate, e.g., the battery current normalized to the rated capacity (C) of the battery. For a 1 Ah battery, a C-rate of 1C represents a 1 Amp current; a 0.5C rate represents a 0.5 Amp current.

battery failure in some of the applications. Figure 1.3 shows a typical capacity fade curve for a Li-ion battery.

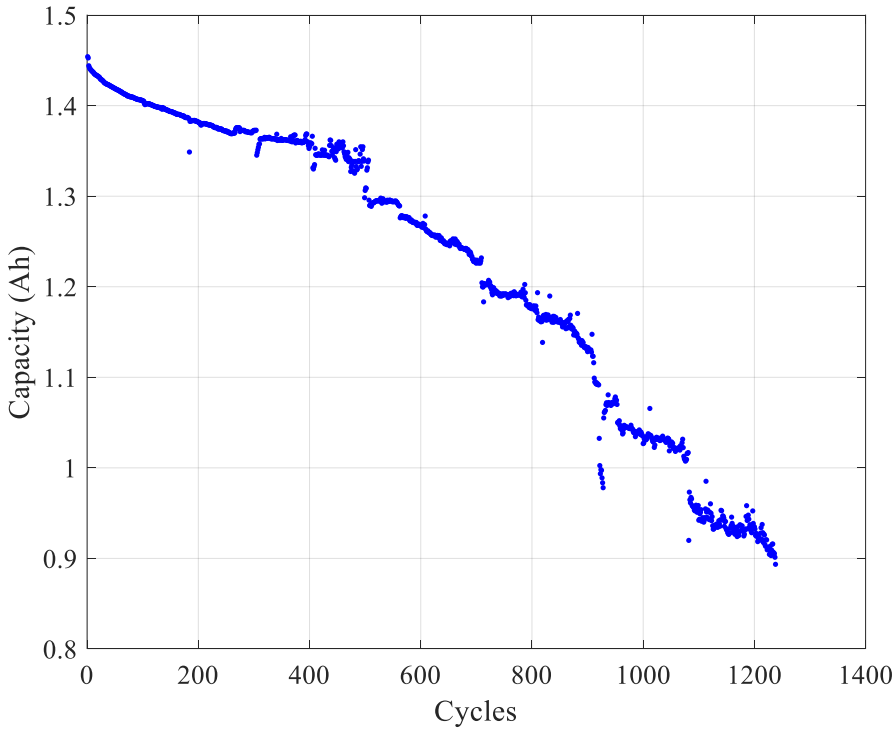


**Figure 1.3.** A typical capacity fade curve for a Li-ion battery.

Performance testing of battery is conducted to qualify a population of batteries according to the performance requirements and the life expectation for its targeted application. In most cases, companies aim to determine the number of cycles to end-of-life (EOL). In some cases, companies aim to determine the amount of capacity fade for a number of required cycles. For critical applications that require extremely high reliability, some companies conduct charge-discharge tests beyond the EOL to understand the full capacity fade profiles of the batteries.

As more and more battery powered products enter the market, the challenges for battery manufactures, supplier and product manufacturers increase exponentially. A survey [9] covering professionals from a broad spectrum of industry segments, including battery cell producers, battery pack and component developers, academic and national labs, and companies

involved in transportation, consumer electronics, and energy storage revealed time-to-market as the biggest concern among respondents followed by battery reliability. More than a quarter of respondents—nearly 27%—listed the amount of time required to estimate battery life as a key bottleneck.

## 1.1 Degradation Mechanisms

The degradation mechanisms in Li-ion batteries can be broadly classified into four types: electrochemical side reactions, mechanical stress-based mechanisms, thermally induced mechanisms, electrically induced mechanisms. Some of these mechanisms lead to gradual degradation of battery involving drop in capacity or rise in the impedance, while the others may cause catastrophic failures such as venting, fire or explosion[2]. In this work, the focus will be on the mechanisms causing gradual degradation at room temperature (~25 $^{o}$C) or above. The relevant degradation mechanisms have been briefly described as follows:

### *1.1.1 Solid Electrolyte Interphase (SEI) Layer*

One of the prominent mechanisms responsible for gradual degradation is solid electrolyte interphase (SEI) layer formation and growth on the negative electrode (Figure 1.5). SEI layer forms on the graphite surface due to the electrolyte reduction process during the first few charge – discharge cycles of the battery after the assembly process. The electrolyte reduction process consumes active $Li^{+}$ ions and produces both organic and inorganic products. While loss of

[2] Lithium-ion batteries pose safety risks due to the presence of flammable electrolyte and oxidizing agent (metal oxide cathode) and can cause fires and explosion if subjected to abusive conditions such as internal/external short circuit, overheating, overcharge, and overdischarge. Manufacturing defects in batteries can also cause these similar types of catastrophic failures. Device manufacturers perform safety testing of batteries to evaluate the catastrophic failure modes. However, this work will mainly focus on the long-term performance and gradual degradation of battery.

active $Li^+$ ions causes loss of capacity in the battery, the production of these insoluble solid byproducts increases the battery impedance. SEI is typically ~20 Å to several hundreds of Angstroms thick layer which is made of a dense inorganic matrix consisting mainly of LiF and $Li_2CO_3$ close to the electrode surface and a porous organic or polymeric layer extending further out from the electrode surface [10]. However, a stable SEI layer is necessary for battery performance and long cycle life as it protects the graphite electrode from further reacting with the electrolyte.

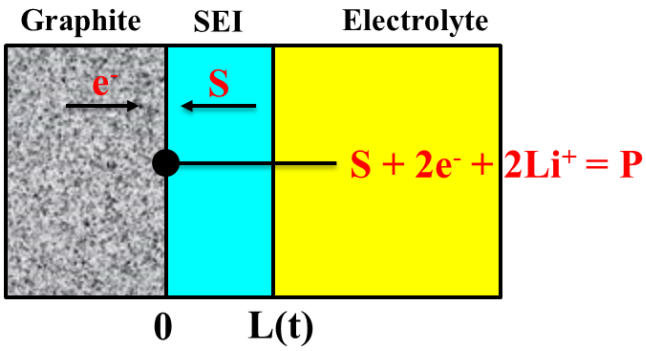


**Figure 1.4.** A simplified schematic of SEI layer on graphite electrode (redrawn from [11]) where S represents electrolyte solvent and P represent electrolyte reduction reaction byproducts.

An ideal SEI layer should have high electronic resistance and good ionic conductivity for the $Li^+$ ion transport and should be impermeable to the electrolyte solvent to prevent its further with graphite electrode. It should also be able to tolerate the mechanical stresses from the volume expansion and contraction of graphite electrode due to lithium insertion and removal during charge and discharge operation, respectively [12]. However, this is not the case. During the cycling operation, cracks in the SEI layer [13] and electrode particles [5], [14] due to mechanical stresses provide fresh new sites for reaction between graphite electrode and electrolyte. Hence there is a continuous growth of SEI layer during the cycling operation leading to loss of capacity and rise of impedance in the battery.

### *1.1.2 Mechanical Degradation of Electrodes*

The mechanism of mechanical degradation is central to the cycling operation of battery and affects both the electrodes. Li insertion and de-insertion into the electrodes during the cycling process cause volumetric changes leading to mechanical stress and strain. Also, phase transitions can occur, which leads to distortion of the crystal lattice and further mechanical stress [7]. Electrode particle fracture can occur especially in high power applications due to mechanical stresses [5]. Gradual structural degradation of the graphite due to cycling was observed in, which was most pronounced on the electrode surface [15]. These disorder and fractured areas provide new sites for SEI layer formation.

Other mechanical degradation modes include loss of contact in the electrode and changes in electrode porosity. Contact loss (i) between electrode active material particles, (ii) between current collector and active material, (iii) between binder and active material, and (iv) between binder and current collector can occur leading to rise in battery impedance [7]. The changes in electrode porosity can occur due to both the volume change and SEI layer formation. The porosity affects the penetration of electrolyte into electrode structure and have a significant influence on battery impedance.

### *1.1.3 Lithium Plating*

Slow lithium-ion diffusion into the negative electrode active material and/or reduced lithium ion diffusion in the electrolyte can result in lithium plating or lithium dendrite formation [7]. While the plated lithium can further react with electrolyte to form SEI layer and cause loss of active lithium (capacity), the dendritic structures of lithium can also lead to internal short-circuits between negative and positive electrodes causing catastrophic failures. The low temperature or fast charging are the most favorable conditions for lithium plating on the negative electrode. Overcharge is also a condition that can lead to lithium deposition.

### *1.1.4 Electrolyte Oxidation*

Stability of electrolyte on the positive electrode interface has not been a cause of concern in the conventional Li-ion batteries. The positive electrode materials within these batteries operated in voltage ranges where their electron energy was above the highest occupied molecular orbital (HOMO ~ 4.3V vs. Li/Li+) of the nonaqueous electrolyte components [16]–[18]. However, as the conventional positive electrode materials like $LiCoO_2$ are pushed beyond their voltage limits and new high voltage positive electrode materials are developed, the electrolyte oxidation becomes a degradation mechanism. This oxidative decomposition of electrolyte can lead to a loss of active mass and Li ions, an increase in the internal resistance, and modification of surface properties of the active material [7]. The reaction products include semicarbonates, polycarbonates, alkoxides, ethers, LiF, $Li_2CO_3$, $Li_xPO_yF_z$, $RCF_x$, etc. [18]–[20]. This process will be accelerated by higher temperature and by high end of charge voltages. Some surface electrolyte reactions are also accompanied by the evolution of gaseous species [21], which can lead to swelling in the pouch batteries.

### *1.1.5 $LiCoO_2$ Structural and Chemical Degradation*

Capacity of $Li_{1-x}CoO_2$ remains limited due to the structural and chemical degradation issues beyond the removal of half mole of lithium ($x > 0.5$) resulting in the end of charge voltage limit of 4.2V. $LiCoO_2$ has rhombohedral $R\bar{3}m$ rock-salt structure with hexagonal symmetry. Beyond $x = 0.5$, a lattice distortion was observed from hexagonal to monoclinic symmetry [22]. Voltage beyond 4.2V have also resulted in abrupt drop in c-parameter of the lattice and accelerated the cobalt dissolution [23]. $Li_{1-x}CoO_2$ was also found prone to losing oxygen at deep lithium extractions ($x > 0.5$) limiting the practical capacity to only 140 mAh/g [24].

# Chapter 2: Li-ion Battery Reliability Testing and Modeling

The life cycle conditions of lithium-ion batteries can be broadly classified into storage and cycling (charge-discharge) operations. During these operations batteries continue to degrade and lose their capacity due to a variety of degradation mechanisms. Many researchers have investigated the storage and cycling operation reliability, life, and performance degradation of different battery chemistries of Li-ion family under different stress factors and hence the literature in this area is vast with several articles published in the last 25 years. There has been extensive effort to understand battery degradation mechanisms and to model the degradation behavior both empirically and analytically. These past studies have been conducted on commercially available Li-ion batteries as well as on prototype batteries developed in the research labs.

Commercial Li-ion batteries are available in various sizes and form factors, which utilize different electrode material compositions and offer different nominal voltages. Some well-known types of Li-ion batteries include lithium cobalt oxide ($LiCoO_2$), NCA ($LiNi_xCo_yAl_{1-x-y}O_2$), NMC ($LiNi_xMn_yCo_{1-x-y}O_2$), and lithium iron phosphate ($LiFePO_4$) positive electrode-based batteries. The commercial batteries from two different manufacturers utilizing same electrode materials and electrolyte solvent may also differ in terms of binder materials and electrolyte additives. Depending upon the electrode materials, electrolyte solvents and additives, these batteries can provide different end of charge voltages including 4.2V and 4.4V. There is a strong push to develop and market high voltage positive electrode and electrolyte materials to improve battery energy density. High energy graphite-$LiCoO_2$ batteries with end

of charge voltage of 4.4V are increasingly being used in portable electronic devices such as smartphone and laptops.

## 2.1 Battery Reliability Literature

There have been several experimental studies with multiple operating conditions on different Li-ion chemistries to understand the effects of different stress factors on battery performance degradation, life and degradation mechanisms. Some of the studies with multiple stress factors and large test matrices have been briefly described in this section.[3] Some of the commonly used physics-based and empirical models to describe battery degradation have also been discussed.

In a cycle life study limited to 500 cycles on 4.2V graphite/$LiCoO_2$ cells by Choi and Lim [25], they concluded that high charge cut-off voltages (tested up to 4.35V) and a long float-charge period at 4.2V or above had the most severe effects on cycle life. They found that the depth of discharge (DOD[4] or ΔSOC) did not affect the cycle life.

Ning et al. [26] studied the effects of discharge rates at three different C-rates (1C, 2C, and 3C) on 4.2V carbon/$LiCoO_2$ battery capacity fade and concluded that at higher C-rates growth of the solid electrolyte interphase (SEI) layer accelerated. The capacity losses were estimated after 300 cycles at 2C and 3C discharge rates and were found to be 13.2 and 16.9% of the initial capacity, respectively. They proposed that the increased temperature due to ohmic heating could cause the evaporation of electrolyte and buildup of pressure due to generation of gaseous

[3] Part of this literature review has been reproduced from [36].

[4] DOD (ΔSOC) is defined as the ratio of amount of charge (Ah) taken out from a battery from a given charge condition (usually 100%, fully charged) to the true battery capacity. For example, if from a full charged 1Ah battery, 0.4Ah charge is taken out during discharge, then the DOD will be 40%. SOC is state of charge of battery which shows how much charge is remaining in the battery. 100% SOC means fully charged battery and 0% SOC means fully discharged battery.

products, resulting in the cracks in the surface film. These cracks provide new sites for the side reaction between lithiated carbon and electrolyte, resulting in the thickening of SEI layer.

Wang et al. [27] studied the cycle life of 3.6V graphite/$LiFePO_4$ cells under five DODs (10% - 90%), five temperatures (-30 $^oC$ – 60 $^oC$) and four discharge rates (C/2 – 10C) and found a power law relation between capacity fade and charge throughput. They defined the charge throughput as the amount of charge delivered by the battery during cycling. Their results showed that the capacity loss was strongly affected by time and temperature, while the effect of DOD (ΔSOC) was less important at C/2 discharge rate.

Ecker et al. [28] conducted an accelerated study on 4.2V graphite/$Li(NiMnCo)O_2$ cells to analyze the influence of cycle depth and mean SOC on cycle aging. They observed that rate of aging increased with increasing cycle depth (ΔSOC) almost linearly. Also they found that for a given cycle depth, minimum aging occurred in cells cycled around 50% mean SOC. However, the generalization of these results to other cathode materials and cell technologies requires more investigation.

Wang et al. [29] investigated the influence of DOD (ΔSOC) (10%-90%), temperature (10 $^oC$ – 46 $^oC$) and discharge rate (0.5C – 6.5C) on the cycle life of 4.2V graphite/$LiNi_{1/3}Co_{1/3}Mn_{1/3}$ + $LiMn_2O_4$ cells. They found that although capacity loss increased at higher DODs, temperature and discharge rate had more significant impacts on capacity fade. Also, they observed a linear relation between capacity loss and charge throughput.

Guan et al. [30] conducted the cycle life testing of 4.2V mesocarbon microbeads (MCMB)/ $LiCoO_2$ commercial cells at different rates (0.6C, 1.2C, 1.5C, 1.8C, 2.4C and 3.0C) and proposed the capacity fade mechanism by analyzing the structure, morphology and electrochemical performance evolution at the capacity retention of 95%, 90%, 85%, 80%.. They concluded that the decay in cathode and cell imbalance caused by the loss of active

lithium irreversibly and the polarization in the full cell dominated the degradation during cycling.

Stroe et al. [31] conducted accelerated calendar and cycle life tests on lithium iron phosphate batteries which are used for wind power plant applications. Four stress factors were used for cycle life tests including temperature (high or low temperature), SOC-level (low or high SOC), cycle depth (big cycle depth), and C-rate (high C-rates). However, the corresponding labels for these factors were not clearly discussed. A power law type model was presented for capacity fade during cycling:

Cui et al. [32] conducted aging experiments of the 4.2V MCMB /$LiCoO_2$ Li-ion batteries with charge-discharge rates (0.6C-1.2C), DOD (20% to 30%), end of charge voltage (4.2V – 4.1V), and operating temperature from 25 $^oC$ to 45 $^oC$ to investigate the lifetime evolution process. This work only considered shallow cycling of battery. They identified temperature, followed by discharge rate and DOD as the most impactful stress factors for battery capacity loss. The orthogonal design did not include end-of-charge voltage stress factor, and its effects were separately investigated and included in the lifetime model.

Baghdadi et al. [33] studied the calendar and power cycling aging of 4.2V graphite/ [$LiNi_{1/3}Mn_{1/3}Co_{1/3}O_2$+$LiMn_2O_4$] and 4.2V graphite/ $LiNi_{0.8}Co_{0.15}Al_{0.05}O_2$ batteries. These batteries were designed for high power application with maximum current ratings of 108 A and 130 A, respectively. Battery aging rate was found to be exponentially dependent on current, temperature, battery state of charge. The maximum DOD in this testing was limited to 40%.

Wu et al. [34] conducted a lithium-ion battery aging study in which pouch cells with 4.2V graphite/ $LiCoO_2$/$LiNi_{0.8}Co_{0.15}Al_{0.05}O_2$ blended chemistry were examined at 3 different temperature (10 $^oC$ – 40 $^oC$) and 3 different discharge levels (1C – 5C). The results showed that high temperature (>25°C) accelerated the aging, however, the effect of discharge rates on aging was not significant.

Diao et al. [35] conducted a multifactor design of experiment (DOE) to study the effects of temperature, discharge C-rate, and charge current cut-off on 4.4V rated commercial graphite/$LiCoO_2$ batteries and found that only temperature influenced the capacity fade rate.

The author of this dissertation has also worked on 3 studies in the past, which have been briefly summarized in the next three chapters and have addressed the research gaps concerning the effects of partial state of charge cycling on graphite/$LiCoO_2$ battery degradation [36], application of battery discharge current for accelerated degradation testing and corresponding model development [37], and development of a methodology of selecting significant stress factors for accelerated test planning, respectively. The main dissertation study of the author addresses the research gaps associated with the effects of rest time on graphite – $LiCoO_2$ battery degradation, which have been summarized in the next section of this chapter.

In addition to various cell level empirical or semi-empirical models fitted using the test data and supported by physics of battery degradation, many researchers have also developed material level physics-based degradation models for individual degradation mechanisms and combined them with either pseudo 2 dimensional (P2D) [38], [39] or single particle models to simulate the battery performance degradation with time/cycles. The most common empirical relation is the exponential Arrhenius type dependency of battery degradation rate on the temperature supported by the effects of temperature on the rate of chemical side-reactions (SEI, electrolyte oxidation) occurring in the battery. The empirical relation between capacity degradation and time/number of cycles has been described mainly by power law (diffusion limited SEI), linear (kinetically limited SEI + material loss), and double exponential models (two-stage degradation – different mechanisms in different stages of degradation) depending upon the presence of various degradation mechanisms. Some of the physics-based degradation models include diffusion based SEI growth model predicting square root dependency of capacity fade over time [11], kinetically limited SEI growth model using a Tafel equation [40],

surface film crack model based on fatigue and Wohler curves [13], and positive electrode dissolution using Tafel kinetics [41]. A detailed review of these models can be found in [42].

### *2.1.1 Studies on Rest Time*

The rest time refers to a time period during which the battery can be either in open rest condition where the battery current is zero and battery terminal voltage can change, or a float rest condition where a constant battery terminal voltage is maintained. Figure 2.1 shows an example of an open rest condition after full charge in a Li-ion battery charge/discharge cycle.

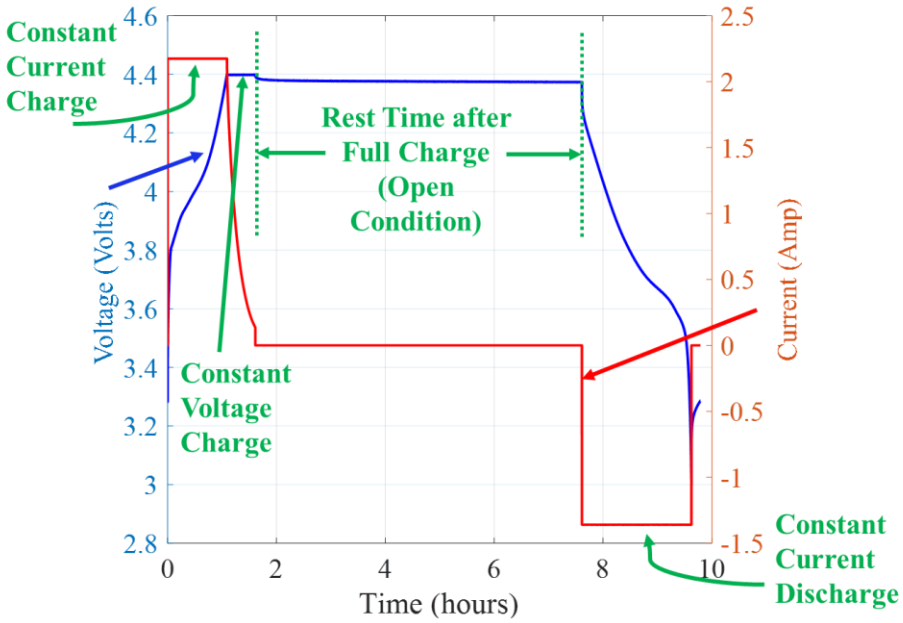


**Figure 2.1.** Rest time after full charge (open condition) in a Li-ion battery charge/discharge cycle.

When a battery-powered device is plugged-in to the charger, depending on the Li-ion battery management system, it may be in a float or open condition once the battery terminal voltage reaches its end-of-charge voltage, a cut-off voltage usually defined based on the battery chemistry to prevent unsafe situations like gas generation or overheating in batteries. The float

condition occurs when the charger continues to act as a constant voltage source and continues to trickle charge the battery. During the float condition, the battery charge current gradually reduces. In todays advanced electronic devices including laptops, cell phones and portable consumer appliances, the charger charges the battery at constant voltage (float condition) until the current drops below C/20, a common charge cut-off current specified in battery datasheet to achieve “Full Charge” status. This charge termination is conducted to ensure battery safety and long life. After the charge termination battery stays in open rest condition and its open circuit voltage starts to drop due to charge redistribution, self-discharge, and internal side-reactions. If the device remains in plugged-in condition for long durations and the battery open circuit voltage drops by more than 200 mV during this period, then the charger usually starts the float operation again to compensate for the voltage drop [43]. A similar open rest condition after full charge also occurs in applications such as satellites and solar energy storage systems where batteries are charged during exposure to the sun and are used (discharged) only when solar energy is not available.

Considering this real-life charging condition, there is a great interest in device manufacturers to understand the relationship between open rest durations after full charge and performance degradation, defined in terms of capacity fade, of Li-ion batteries. The key questions are: is keeping the electronic devices plugged-in to chargers for long durations (open rest) more detrimental for batteries compared to removing the device immediately after the full charge and using it on battery power (continuous cycling)?; does the answer to first question depend upon operating temperature?; if there are differences in the capacity fade rate under two conditions, then what are the reasons for those differences?; and is there a model to quantify the effects of rest time on battery capacity fade?

As of this writing, three research teams have looked into rest time: Reichert et al. [44], Rashid and Gupta [45], and Nelson et al. [46]. Reichert et al. [44] investigated the influence of open

rest time conditions on the lifetime of commercial Li-ion batteries. They studied rest periods of 0 s, 60 s, and 7200 s (2 h) after full discharge and one level (2 h) of rest period after full charge. These rest periods were applied after every 5 full cycles. They also studied micro vs macro breaks by applying 12 s of rest period after full discharge in each cycle (dividing 60 s equally over 5 cycles) for a group of batteries. Their results showed that there was no difference in the capacity fade behavior of batteries irrespective of whether the rest period was applied after full charge or after full discharge. No observable differences between the capacity fade trends of batteries with and without rest periods were found.

Rashid and Gupta [45] discussed the effects of open rest time in mesocarbon microbeads/$LiMn_2O_4$ batteries using simulation results from a solid electrolyte interphase (SEI) layer model. They simulated rest periods ranging from 5 min to 2 h after charge/discharge operations. They concluded that the rest after charge had only marginal effects compared to the rest after discharge, which resulted in a thicker SEI film due to the presence of higher lithium concentration in the negative electrode.

Nelson et al. [46] compared the performance of graphite/$LiNi_{0.4}Mn_{0.4}Co_{0.2}O_2$ batteries with commercially available 4.2–4.4 V end-of-charge voltage rated graphite/$LiCoO_2$ batteries under charge-24 h float rest-discharge cycling operation at 40 $^oC$. The $LiNi_{0.4}Mn_{0.4}Co_{0.2}O_2$ cell operated to 4.4 V had up to 8% capacity loss after 40 cycles and was comparable to the 4.2 V $LiCoO_2$ cell. The 4.35 V and 4.4 V $LiCoO_2$ cells had up to 10% and 20% capacity fade, respectively after 40 cycles. The authors used differential voltage analysis to theorize that degradation caused damage to the positive electrode. This study investigated only one float rest duration of 24 h at full charge.

The past studies tested/simulated open rest period of only up to 2 h after charge and found either no or marginal effects on battery degradation. Nelson et al. [46] tested only one long rest time of 24 h under float condition. Hence there has been no study on the effects of open rest

conditions with durations longer than 2 h. Additionally, none of these studies used the real-life charging conditions for the electronic devices in their test profiles. Reichert et al. [44] added open rest time after charge only after every 5 cycles and also limited the constant voltage phase of charging by charging time rather than by charge cut-off current. Rashid and Gupta [45] did not use constant voltage charging phase in their simulation. Nelson et al. [46] used float condition for the entire duration of 24 h which is also not the case in the modern electronic devices.

This study evaluates batteries from 5 of the world's leading manufacturers of batteries (the names are not given). All the batteries were tested under similar conditions using the real-life charge conditions, and their capacity fade trends are presented to evaluate the relationship between open rest time and battery performance degradation. The research objectives of the study have been summarized in the next section.

## 2.2 Research Objectives

- To determine the effects of open rest time after full charge on graphite/$LiCoO_2$ battery performance degradation at different ambient temperatures.

- To evaluate the generalization of these effects across graphite/$LiCoO_2$ batteries from different manufacturers

- To perform capacity fade trend modeling analysis and to understand interplay between the rest time induced degradation and cycling induced degradation

- To identify degradation causes and mechanisms of individual electrodes in the battery

- The study includes the differential voltage analysis of full cells to non-destructively infer the individual electrode degradation causes, cell disassembly, X-ray diffraction (XRD) to understand electrode structural degradation and to identify nature of possible surface depositions, scanning electron microscopy (SEM) to inspect surface morphologies of electrodes, and energy dispersive X-ray spectroscopy (EDX) to identify elemental composition of electrodes and surface deposits.

# Chapter 3: Effects of Partial State of Charge Cycling

This study [36] quantifies the effect of partial charge-discharge cycling on Li-ion battery capacity loss by means of cycling tests conducted on 4.2V graphite/$LiCoO_2$ pouch cells under different state of charge (SOC) ranges and discharge currents. The results are used to develop a model of capacity fade for batteries under full or partial cycling conditions. This study demonstrates that all the variables studied including mean SOC, change in SOC (ΔSOC) and discharge rate have a significant impact on capacity loss rate during the cycling operation.[5]

## 3.1 Experimental Test Procedure

Commercial graphite/$LiCoO_2$ pouch cells with a nominal capacity of 1.5 Ah (at C/5 rate) and a nominal voltage of 3.7 V were used in the study. An end-of-charge voltage of 4.2 V and an end-of-discharge voltage of 2.75 V were specified by the manufacturer. The charging and discharging of the cells were carried out using an Arbin BT2000 Battery Tester with 16 independent channels. All the tests were conducted in a semi-temperature controlled room with temperature of $25\pm2^{o}$C. The initial characterization tests for the cells included constant current constant voltage (CCCV) charge - constant current (CC) full discharge (4.2V-2.7V) at C/2 rate to determine battery discharge capacity.

[5] This work has been published in the Journal of Power Sources [36] and part of the published article has been reproduced here in this chapter.

## 3.2 Test Matrix

Different SOC ranges with different mean SOC and ΔSOC values were selected between 0% and 100% to understand the battery degradation behavior in different regions of full SOC range. The primary objective of this study is to find the effects of SOC ranges on battery cycle performance at a constant discharge rate of C/2. However, for the SOC ranges with mean SOC of 50%, the tests were conducted at two different discharge rates of C/2 and 2C. The purpose behind using two different discharge rates is to find if the relative performance of cells cycled under different SOC ranges gets affected from discharge rate. For 1.5 Ah cells used in this study, C/2 and 2C rates refer to 0.75 A and 3A, respectively. Five SOC ranges were selected while keeping in mind the requirement of having enough data points to find the capacity loss model constants. Table 3.1 provides the number of cells that were tested under each of the mean SOCs, ΔSOCs and discharge C-rates.

**Table 3.1.** Sample distribution in the test matrix for this study.

| SOC Range | Mean SOC | ΔSOC | Discharge C-rate | |
|---|---|---|---|---|
| | | | C/2 | 2C |
| 0%-100% | 50% | 100% | 2 | 2 |
| 20%-80% | 50% | 60% | 2 | 2 |
| 40%-60% | 50% | 20% | 2 | 2 |
| 40%-100% | 70% | 60% | 2 | × |
| 0%-60% | 30% | 60% | 2 | × |

## 3.3 Results and Discussion

The capacity loss results from the testing at different SOC ranges are presented in this section. In Figure 3.1-3.2, normalized discharge capacity is plotted against equivalent full cycles. The normalized discharge capacity denotes the percentage ratio of the discharge capacity of a degraded battery to the initial (first cycle) battery discharge capacity. It is an indicator of battery state of health (SOH). The testing results are presented here up to around 800 equivalent full cycles (approximately 1000Ah cumulative discharge) for all the SOC ranges except 40%-60% range. For the 40%-60% range results only up to around 450 equivalent full cycles (approximately 600Ah cumulative discharge) have been presented considering a slow cumulative discharge (Ah) accumulation rate. Intuitively, it may seem that for a given time period, no. of partial cycles for 40%-60% SOC range should be three times that for 20%-80% SOC range. However, that is not the case in the testing due to the inclusion of 30 minutes rest period after every charge and discharge steps.

In Figure 3.1, the mean SOC during cycling is fixed at 50% for the three cycling ranges (0%-100%, 20%-80%, and 40%-60%). ΔSOC is the varying parameter with values 100%, 60%, 20% respectively. Also, two discharge rates of C/2 and 2C are used. The results presented are the average values of two cells chosen for each cycling range. It is evident from Figure 3.1 a) that cells cycled at 40%-60% range outperform the cells cycled at the other two ranges up to 450 equivalent cycles. If we look at the long-term cycling operation at C/2 rate, the 20%-80% cells outperform the 0%-100% cells in terms of retaining their capacity by an 8% margin after approximately 800 equivalent full cycles.

For cells discharged at 2C (Figure 3.1 b)), the cells cycled in the 40%-60% range perform far better than the cells under the other two ranges up to 450 equivalent cycles. However, the capacity loss (%) difference between cells under 20%-80% and 0%-100% ranges is almost negligible at the end of 800 equivalent cycles. This is quite different from what is observed at

C/2 rate. At high discharge rates such as 2C, cells see a significant temperature rise due to ohmic heating. The high temperature may be playing a larger role than ΔSOC, and hence diminishes the performance gap between the cells cycled in the 20%-80% and 0%-100% ranges.

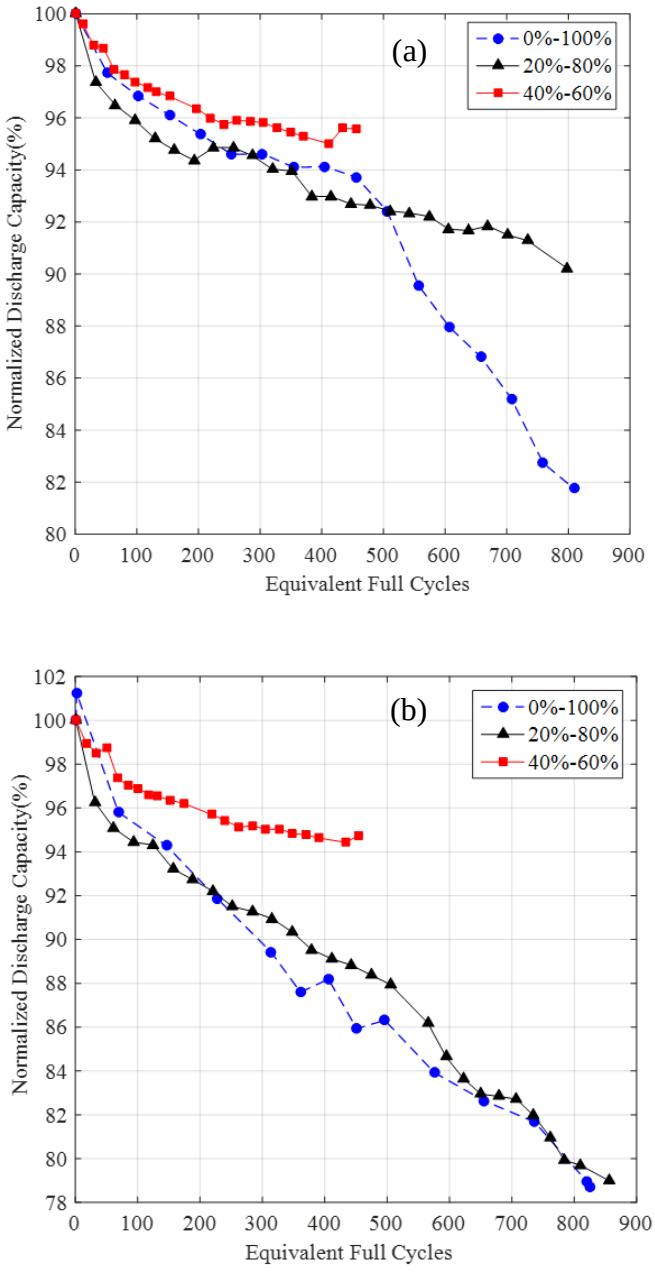


**Figure 3.1.** Capacity fade results for Mean SOC = 50%, ΔSOC = 100%, 60%, 20%, (a) C/2 rate, (b) 2C rate.

Figure 3.2 shows average results for three cycling ranges (0%-60%, 20%-80% and 40%-100%) with a fixed ΔSOC value of 60% and varying mean SOC values of respectively 30%, 50% and 70% at a C/2 discharge rate. It can be observed that lowering the mean SOC reduces the rate of degradation. The cells cycled at 0%-60% perform far better than the other cells in terms of retaining the capacity. Even after 700 equivalent cycles the capacity retention is more than 97% for 0%-60% range. However, the degree of performance improvement in case of 0%-60% range is quite unexpected. The results suggest either the absence of a degradation mechanism for 0%-60% range that is present in other SOC ranges or the presence of a different degradation mechanism with a very slow degradation rate.

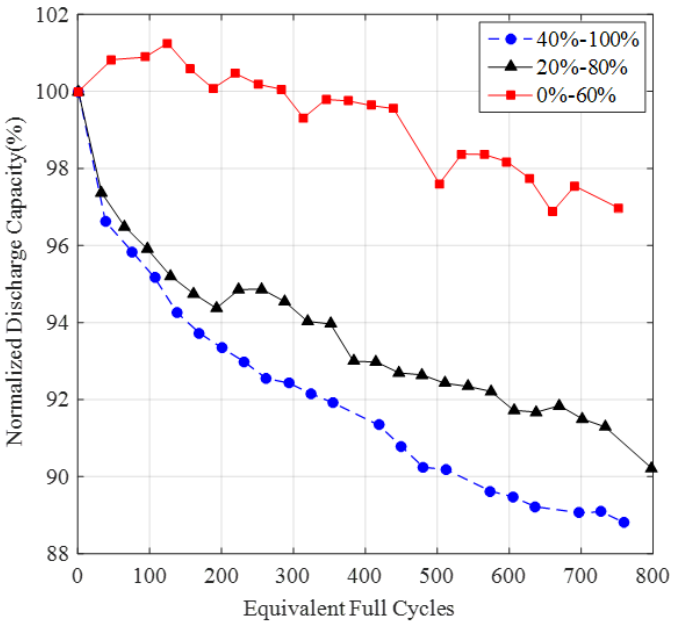


**Figure 3.2.** Capacity fade results for Mean SOC = 30%, 50%, 70%, ΔSOC = 60%, C/2 rate.

## 3.4 Capacity Fade Modeling

Based on the values of *A* for all the SOC ranges except 0%-60%, a curve fit for *A* has been obtained and presented in Equation (3.1). In Equation (3.1) mean SOC and ΔSOC are used as a fraction rather than as a percentage. The $R^2$ value for curve fitting of *A* is 0.97. A final normalized discharge capacity model is presented in Equation (3.2). Values of constant *k1*, *k2* and *k3* are respectively 3.25, 3.25 and -2.25 in Equation (3.2).

$$A = 3.25 \cdot SOC_{mean} \cdot (1 + 3.25 \cdot \Delta SOC - 2.25 \cdot \Delta SOC^2) \quad (3.1)$$

$$NDC\ (\%) = 100 - k1 \cdot SOC_{mean} \cdot (1 + k2 \cdot \Delta SOC + k3 \cdot \Delta SOC^2) \cdot \left({}^{EFC}/_{100}\right)^{0.453} \quad (3.2)$$

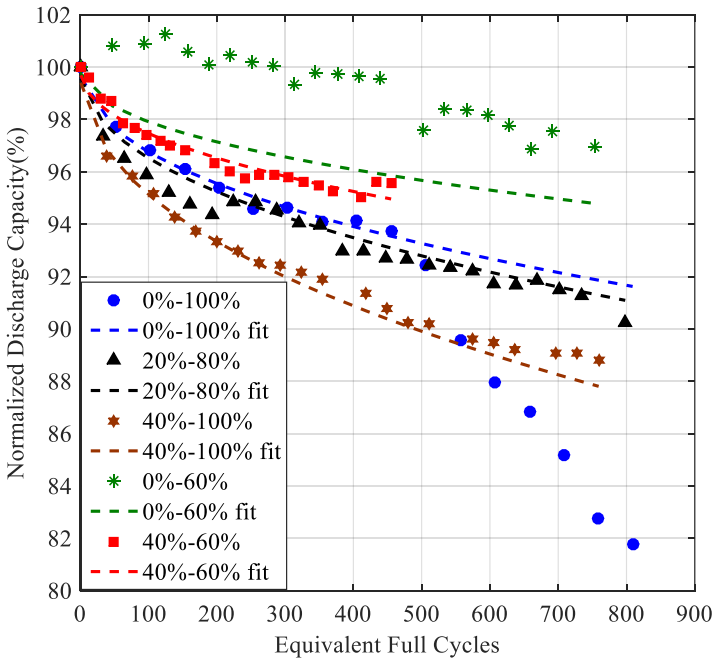


**Figure 3.3.** Comparison of experimental data with the power law model curve fit.

Figure 3.3 shows the experimental data from testing as well as the curve fits from power law model (Equation (3.1)). Power law model fits the experimental observations for the first 500 equivalent full cycles for all the SOC ranges except 0%-60%. Even after 500 equivalent full cycles, normalized discharge capacity trends for the SOC ranges 20%-80% and 40%-100% seem to follow the derived power law model. However, 0%-100% range shows a sudden acceleration in capacity loss rate after 500 equivalent full cycles suggesting the initiation of a new degradation mechanism with almost linear capacity fade model. Hence the developed power law model cannot fit the experimental data for 0%-100% range after 500 equivalent full cycles. One of the possible causes behind this increase in degradation rate in 0%-100% may be the generation of cracks in electrode and SEI layer and thus providing the fresh new sites for side reactions with electrolyte to cause loss of active lithium. Since 0%-60% SOC range exhibits a quite unexpected capacity fade behavior with the minimal capacity loss (%) among all the tested ranges, more testing in low mean SOC region will be required to extend the developed model to all possible SOC ranges. The current model is suitable for only static SOC range cycling conditions where the battery is being cycled under nearly constant SOC ranges.

# Chapter 4: Discharge Current based Accelerated Battery Testing

Cycling at a nominal charge/discharge current requires an extensive amount of time and resources, and hence a battery qualification process based on battery cycle testing may cause delays in time to market. Discharge current can be used for accelerating Li-ion battery cycle testing. This study [37] develops an accelerated capacity fade model for Li-ion batteries under multiple current loading conditions, to translate the performance and degradation of a battery population at accelerated current conditions to normal current conditions. A nonlinear mixed-effects regression modeling technique is used to consider the variability of repeated capacity measurements on individual batteries in a population.[6]

## 4.1 Capacity Fade Model Development

To assess the reliability of a product quickly, accelerated testing is conducted by increasing the loading (stress) conditions on the product. In the case of Li-ion batteries, testing at a high discharge current (C-rate) is one approach to accelerated testing. During the testing capacity fade is recorded at different number of cycles, which serves as the indicator of degradation for batteries. The capacity fade measurements of batteries can be used to model the degradation process, which can further be used for failure time prognosis.

[6] This work has been published in the International Journal of Electrical Power & Energy Systems [37] and part of the published article has been reproduced here in this chapter.

Capacity degradation in Li-ion batteries occurs due to a multitude of degradation mechanisms. The side reactions between anode and electrolyte result in loss of active lithium and formation of an SEI layer on the anode. In particular, Ning et al. [26] studied the effects of discharge rates at three different C-rates (1C, 2C, and 3C) on Li-ion battery capacity fade and concluded that at higher C-rates growth of the solid electrolyte interphase (SEI) layer accelerated.

Christensen and Newman [5] developed a mathematical model that calculated volume expansion and contraction and concentration and stress profiles during lithium insertion into and extraction from a spherical particle of electrode material. Their simulation showed that high-power (high current) applications, such as HEVs, had an increased likelihood of particle fracture compared to low-power applications. This stress-induced cracking can provide new sites for the growth of SEI layer. These results suggest that the SEI layer remains the prominent degradation mechanism in Li-ion batteries during cycling and higher discharge rates further accelerate the growth of SEI layer by means of overheating and mechanical stress induced surface film and electrode particle cracking.

Various studies have proposed a power law relationship for SEI layer growth modeling with square root dependence on time based on physics-based principles [11], [47]. As per [11],

$$L(t) = 2\delta\sqrt{D_S t} \tag{4.1}$$

$$D(t) = \frac{N_L(t)}{N_0} = \frac{Z_P c_P A_{NE}}{N_0} L(t) = \frac{2\delta Z_P c_P A_{NE}}{N_0}\sqrt{D_S t} \tag{4.2}$$

where, L(t) denotes SEI thickness in cm and D(t) is fractional capacity loss at time, t; $D_S$ is the effective diffusivity of solvent S in SEI phase; $\delta$ is a constant; $Z_P$ is the stoichiometric coefficient of Li in P; $c_P$ is the constant molar density of P in SEI layer; the negative electrode

area ($A_{NE}$) is a cell design parameter and represents the actual carbon surface area that is both electrochemically active and accessible to electrolyte; and the initial capacity ($N_0$) is a measured value. It has been assumed that cell capacity is proportional to the moles of Li available for cycling and all capacity loss ($N_L$) is due to the Li consumption associated with SEI layer growth process.

For cycling operation, no. of cycles, $N_c$, should be considered as the independent transient variable in place of variable t. Additionally, the model presented in [11] is based on the assumption of storage under float charge condition with constant voltage and state of charge (SOC). It has been shown in a detailed physics-based SEI layer growth simulation [48] that the value of power law exponent can also assume values other than 0.5 in case of decrease in negative electrode SOC, which decreases the potential and driving force for film growth. In a cycling study, the negative electrode SOC does not remain constant and can vary from 0% to 100% and hence the experimental data may not always fit a power law exponent of 0.5. Hence in order to make the model general and provide an additional parameter for fitting the data, a generalized power law model with an exponent of *b* and number of cycles as independent variable has been adopted in this paper.

$$D = K.N_c^{\,b} \tag{4.3}$$

$$NDC = 1 - K.N_c^{\,b} \tag{4.4}$$

where *NDC*, normalized discharge capacity, is defined as the ratio of battery capacity at a given cycle count to its initial capacity; and *K* is the power law coefficient. Here, *K* is proportional to the diffusivity $D_s$ of solvent component S in SEI layer and the negative electrode area, $A_{NE}$ (Equation (4.2)). Diffusivity, $D_s$ is considered a function of battery temperature which will

depend upon environment temperature (*T*) and battery current (C-rate) during cycling due to ohmic heating. As the battery current is increased, the susceptibility of SEI layer cracking and electrode particle cracking is also increased. These cracks can provide new sites (areas) for electrolyte reduction and hence C-rate can affect the effective negative electrode area ($A_{NE}$) accessible to electrolyte. Hence, the effects of environment temperature (*T*) and battery current (C-rate) are included in the model in the form of parameter *K* as follows:

$$K = f(T, C_{rate},) \tag{4.5}$$

where *f(.)* is a continuous function; $C_{rate}$ covers both charge and discharge current rates. In this accelerated testing study charge $C_{rate}$, has been considered constant and hence its effects have not been investigated. In order to model the effects of *T* (thermal stress) and discharge $C_{rate}$ (non-thermal stress) on $D_s$ and $A_{NE}$, a generalized Eyring model form [49], [50] is being adopted for *K*. Generalized Eyring model is widely used in the field of reliability to model life-stress relationship under chemical reactions based mechanisms when both thermal and non-thermal stresses are involved and their interaction can be of interest.

$$K = A.T^{\alpha}.\exp\left(-\frac{B}{T} + \left(C + \frac{D}{T}\right).g(C_{rate})\right) \tag{4.6}$$

where α, *A, B, C,* and *D* are model constants and are independent of *T* and discharge $C_{rate}$; *T* is environment temperature in Kelvin; and $C_{rate}$ represents only the discharge current rate; g(.) is a function of nonthermal stress, $C_{rate}$ and has been chosen as identity function ($g(C_{rate}) =$

$C_{rate}$) based on empirical evidences from the testing data used in this study. Equations (4.4) and (4.6) can be combined to provide a model for *D*:

$$D = A.T^{\alpha}.\exp\left(-\frac{B}{T} + \left(C + \frac{D}{T}\right).C_{rate}\right) * {N_c}^{b} \tag{4.7}$$

$$D = \left(A.T^{\alpha}.\exp\left(-\frac{B}{T}\right)\right).\exp\left(\left(C + \frac{D}{T}\right) * C_{rate}\right) * {N_c}^{b} \tag{4.8}$$

If the environment temperature, *T*, is kept constant during the accelerated testing study, then the model terms *B/T* and *D/T* in Equation (4.8) will also become constants to reduce the model to just one stress variable of discharge $C_{rate}$.

$$D = \beta_0 * \exp(\beta_1 * C_{rate}) * {N_c}^{b} \tag{4.9}$$

Therefore,

$$NDC = 1 - \beta_0 * \exp(\beta_1 * C_{rate}) * {N_c}^{b} \tag{4.10}$$

$$K = \beta_0 * \exp(\beta_1 * C_{rate}) \tag{4.11}$$

$$\beta_0 = \left(A.T^{\alpha}.\exp\left(-\frac{B}{T}\right)\right),\ \beta_1 = C + \frac{D}{T} \tag{4.12}$$

Equations (4.9, 4.11) show normalized capacity fade and the normalized discharge capacity models respectively with $\beta_0$, $\beta_1$, and $b$ as final model parameters. The proposed model with constant temperature condition has a power law type relation with the number of cycles and an exponential relationship with the discharge C-rate.

## 4.2 Acceleration Factor

Once the capacity fade model is obtained, the acceleration factor can be calculated for the discharge C-rate stress factor. The acceleration factor provides a quantitative measure of amount of change in degradation rate corresponding to the change in a stress variable. It can be calculated by comparing either the battery capacity fade trends or the times to failure at two different values of the stress variable. Using the capacity fade trends, the acceleration factor corresponding to the discharge C-rate stress variable is given by the following equations:

$$AF = {D(C_{rate}, N_c)}\Big/{D(C_U, N_c)} \tag{4.13}$$

$$AF = \frac{\beta_0 * \exp(\beta_1 * C_{rate})}{\beta_0 * \exp(\beta_1 * C_U)}$$

$$AF(C_{rate}) = \exp\left(\beta_1 * (C_{rate} - C_U)\right) \tag{4.14}$$

where, *AF* is the acceleration factor, $C_U$ represents use (normal) level discharge C-rates and $C_{rate}$ is the accelerated level discharge C-rate. Equations (4.11) and (4.14) can be used to show the relation between normalized capacity fade, *D*, and acceleration factor, *AF*:

$$D(C_{rate}, N_c) = \beta_0 * \exp(\beta_1 * C_U) * AF * {N_c}^b$$

$$D(C_{rate}, N_c) = K_U * AF * {N_c}^b \tag{4.15}$$

$$NDC(C_{rate}, N_c) = 1 - K_U * AF * {N_c}^b$$

where, $K_U$ represents the power law coefficient for use level discharge C-rate, $C_U$; and $AF$ is the function of accelerated discharge C-rate, $C_{rate}$ and use level discharge C-rate, $C_U$.

The acceleration factor, $AF$, in Equation (4.14) signifies by what amount the capacity fade will be accelerated at an accelerated discharge C-rate level with respect to the use level discharge rate, $C_U$, at a given number of cycles, $N_c$. As evident from Equation (4.14), the value of the acceleration factor will be less than 1 for C-rate values less than $C_U$. If the acceleration factor is calculated on the basis of time (cycles) to failure (TTF) of the battery, then a different approach should be adopted. For example, if the failure threshold for a battery is defined as $D_{FT}$, then the acceleration factor based on the time (cycles) to failure can be calculated as follows:

$$AF_T = {TTF(C_U, N_c)}\Big/{TTF(C_{rate}, N_c)} \tag{4.16}$$

$$AF_T = \frac{\left({D_{FT}}/{(\beta_0 * \exp(\beta_1 * C_U))}\right)^{1/b}}{\left({D_{FT}}/{(\beta_0 * \exp(\beta_1 * C_{rate}))}\right)^{1/b}}$$

$$AF_T = (\exp(\beta_1 * (C_{rate} - C_U)))^{1/b} \tag{4.17}$$

$$AF_T = (AF)^{1/b}$$

It is clear from Equation (4.17) that $AF_T$ is different than AF in magnitude. Hence, the developed accelerated degradation model does not qualify as the scale-accelerated failure-time (SAFT) model [51]. In a SAFT model the degradation of a product at a given stress level can be transformed to degradation at any other stress level just by scaling the time (cycle) axis by the acceleration factor. In other words, the acceleration factor calculated using degradation (capacity fade) value and that calculated using time (cycles)-to-failure value remains the same

for SAFT models. This is not the case with the proposed capacity fade model for Li-ion batteries. Since both the battery capacity fade and cycles-to-failure are important parameters for the battery reliability, the type of acceleration factor should be chosen based on the requirements of the application. When there is no hard failure threshold, $D_{FT}$, defined for the batteries, then the capacity-fade-based acceleration factor should be used. In this paper, the capacity-fade-based acceleration factor, *AF*, has been used in the subsequent analysis.

## 4.3 Non-linear Mixed Effect Modeling

Individual batteries in a population such as the one belonging to the same production lot exhibit variability in their capacity fade paths even when they are subjected to same operating conditions. This variability is usually caused by inherent design, manufacturing, and material differences. Depending upon the manufacturing quality control, these variations can be small or large in magnitude. Mixed-effects modeling is useful in considering the variation among individual batteries and captures these variations in the form of fixed and random effect components of the degradation model parameters. Each model parameter value is represented as a combination of a fixed-effect value and a random-effect value. The parameters that do not vary across batteries within a population have only a fixed-effect component. The main idea is to find the distribution of model parameters to consider the uncertainty around the mean degradation process of the whole population of batteries. Hence this method is suitable for analyzing the degradation behavior of the population of batteries.

If the capacity measurements of batteries have been taken at different cycle instances denoted by $Nc_j$, where $j$ = 1, 2, 3, …, then for battery $i$ at cycle instance $j$, the capacity fade can be considered as below:

$$y_{ij} = D_{ij} + \epsilon_{ij}\ , \quad \text{i} = 1,2,3,\ldots.\text{n}, \text{j} = 1,2,3,\ldots\text{m}_{\text{i}}, \qquad \epsilon_{ij} \sim N(0, {\sigma_{ij}}^2) \tag{4.18}$$

where $y_{ij}$ is the measured (calculated) normalized capacity fade, $D_{ij}$ (= $D(Nc_j, \alpha)$) is the actual normalized capacity fade for battery $i$ at cycle count $j$, $\epsilon_{ij}$ is the error term with zero mean and variance ${\sigma_{ij}}^2$ and $\alpha$ is a vector of $k$ unknown parameters for battery $i$. The proposed capacity fade model under accelerated C-rate loading can be embedded with mixed effect model as below:

$$D = K_U * AF * {N_c}^b$$

$$D = K_U * \exp(\beta_1 * (C_{rate} - C_U)) * {N_c}^b \tag{4.19}$$

$$Y_{ij} \sim \mathcal{N}(\mathrm{D}(\mathrm{N}_{cj}; \alpha_i), \sigma^2) \qquad i = 1,2,\dots,n \text{ and } j = 1,2,\dots,m_i$$

$$\mathrm{D}(\mathrm{N}_c; \alpha_i) = \alpha_{1i} * \exp(\alpha_{2i} * (C_{rate} - C_U)) * {N_c}^{\alpha_{3i}} \tag{4.20}$$

$$H(\alpha_i) = H\left(\begin{bmatrix}\alpha_{1i}\\ \alpha_{2i}\\ \alpha_{3i}\end{bmatrix}\right) = H\left(\begin{bmatrix}K_U\\ \beta_1\\ b\end{bmatrix}\right) \sim \mathcal{N}\left(\begin{bmatrix}\mu_1\\ \mu_2\\ \mu_3\end{bmatrix}, \Sigma\right) \tag{4.21}$$

$$H(\alpha_{ki}) = fixed\ effect\ (H(\alpha_k)) + random\ effect_i\ (H(\alpha_k)), \qquad k = 1,2,3 \text{ and } i = 1,2,\dots,n$$

where, $Y_{ij}$s are the capacity measurements; $\sigma^2$ is the constant error variance across a given battery population; $n$ is the number of batteries in a population; $m_i$ is the number of tested cycles for battery $i$ in a population; $H(.)$ is a reparametrization function to ensure the joint normality assumption of random effects of model parameters; $\mu_k$, k = 1, 2, 3 represents the mean or fixed-effect values of the three model parameters; and $\Sigma$ is the diagonal covariance matrix with the assumption of zero off-diagonal covariance between the random effects of model parameters.

Also the model parameter with only fixed-effect component will have zero variance in the $\Sigma$ matrix.

The maximum likelihood estimation of model parameters for non-linear mixed effect model is numerically complex exercise since it involves the evaluation of a multiple integral in loglikelihood function, which in most cases does not have a closed form expression [52]. The methods developed in [52], [53] provide computationally efficient approximations to maximum likelihood (ML) estimates for parameter estimations. In this work, the likelihood of the non-linear model has been approximated by the likelihood for the linear mixed-effects (LME) model using MATLAB function nlmefit which implements the methods from [52], [53]. For detailed explanation on parameter estimation methods for non-linear mixed-effect models, please refer to [52], [53].

## 4.4 Experimental Studies and Test Results

Li-ion batteries were tested by a device manufacturer for capacity fade at four different discharge C-rates: 0.2C, 0.5C, 1C, and 2C while keeping the other stress factors constant. The idea behind testing at different discharge C-rates was to collect data on the effects of discharge C-rates on the battery capacity fade trends. The testing procedure involved charge-discharge cycling between 3.0 V to 4.1 V. The batteries were discharged at the designated C-rate values. Table 4.1 provides the tested discharge C-rate conditions and number of samples for each condition. The cycle testing was conducted under fixed and controlled environmental temperature of 37 $^{o}$C.

**Table 4.1.** Test conditions and sample distributions.

| Discharge C-rate | No. of Samples |
|---|---|
| 0.2C | 2 |
| 0.5C | 14 |
| 1C | 5 |
| 2C | 3 |

The testing data was limited to 250 cycles. Figure 2.4 shows the normalized discharge capacity profiles for batteries. It is clear from the figures that even for same discharge C-rate condition, there are variations among the capacity fade profiles for individual batteries from a population.

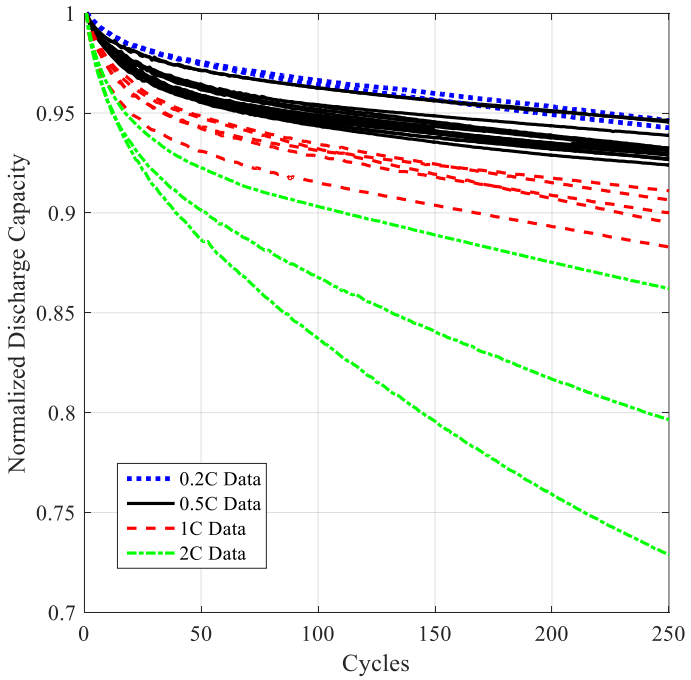


**Figure 4.1.** Normalized discharge capacity testing data at different C-rates for battery population type A.

## 4.5 Model Validation

To demonstrate the suitability of the model developed (Equation (4.15)), it has been fitted against the testing data using MATLAB function nlmefit. It has been suggested in [54] that stability and robustness of the approximate ML algorithm can be improved by estimating the power law coefficient, *K*, (Equation (4.12)) at a level of discharge rate that is central to experimental discharge C-rates rather than at use level discharge C-rate, $C_U$. This is required to reduce the correlation between the estimates of $\beta_1$ and the parameters relating to power law coefficient, *K*. Hence 1C is chosen as the central discharge rate providing new parametrization with $[\alpha_1 \quad \alpha_2 \quad \alpha_3] = [K_{1C} \quad \beta_1 \quad b]$, where $K_{1C} = K_U \times AF(1C)$. In order to ensure the joint normal distribution of random effects of model parameters, [55] suggested to apply reparametrization techniques such as Box-Cox transformation. In this study log reparametrization, a special case of Box-Cox transformation, has been applied to the model parameters with random effects. The selection of log transformation is driven by the prior knowledge about the possible range of values that the model parameters and model output can take and the trial-and-error based normality assumption testing. For example, the model parameter, *b* is expected to be a real number with value possibly between 0 and 1. The log transformation ensures that the model does not lose the physical meaning associated with it and produce erratic estimates such as complex or negative values for *b*. The reparametrization needs to be applied to only those model parameters which exhibit random effects. Hence, initially without any reparametrization ($H(\alpha) = \alpha$), the mean and covariance matrices of original capacity fade model parameters ($[K_{1C} \quad \beta_1 \quad b]$) for battery population A were obtained as below:

$$\mu_A = \begin{bmatrix} \mu_1 \\ \mu_2 \\ \mu_3 \end{bmatrix} = \begin{bmatrix} 0.0107 \\ 0.4163 \\ 0.3959 \end{bmatrix}$$

$$\Sigma_A = \begin{bmatrix} 9E-06 & 0 & 0 \\ 0 & 0 & 0 \\ 0 & 0 & 0.0032 \end{bmatrix}$$

As can be seen from covariance matrix, $\Sigma_A$, the two parameters $K_U$ and $b$ are mixed effects and vary across batteries within the population and the parameter $\beta_1$ is a fixed effect. Hence, parameter $\beta_1$ can be assumed to be a material property which does not vary from battery-to-battery. A fixed-effect value of $b$ (= $\mu_3$) close to 0.5 suggests the presence of SEI layer degradation mechanism [11], [47]. After applying a log transformation to model parameters with random effects, the new parameters which need to be estimated are as follows: $H(\alpha) = [logK_{1C} \quad \beta_1 \quad logb]$. The joint distribution for these transformed model parameters is provided in Equation (4.22) using nlmefit function. This function also provides the transformed model parameter values for each battery in the population which can be used to plot the model output. Figure 4.2 compares the model fits for individual batteries with the testing data. It is clear from the figure that the mixed-effect modeling method is capable to capture the variability among the capacity fade profiles of the battery. The maximum root mean square error (RMSE) for the fits in Figure 4.2 is limited to 0.0027.

$$H(\alpha) = \begin{bmatrix} logK_{1C} \\ \beta_1 \\ logb \end{bmatrix} \sim \mathcal{N}\left(\begin{bmatrix} -4.5472 \\ 0.5625 \\ -0.9359 \end{bmatrix}, \begin{bmatrix} 0.0937 & 0 & 0 \\ 0 & 0 & 0 \\ 0 & 0 & 0.0178 \end{bmatrix}\right), \ \hat{\sigma}^2 = 3.14E-06 \tag{4.22}$$

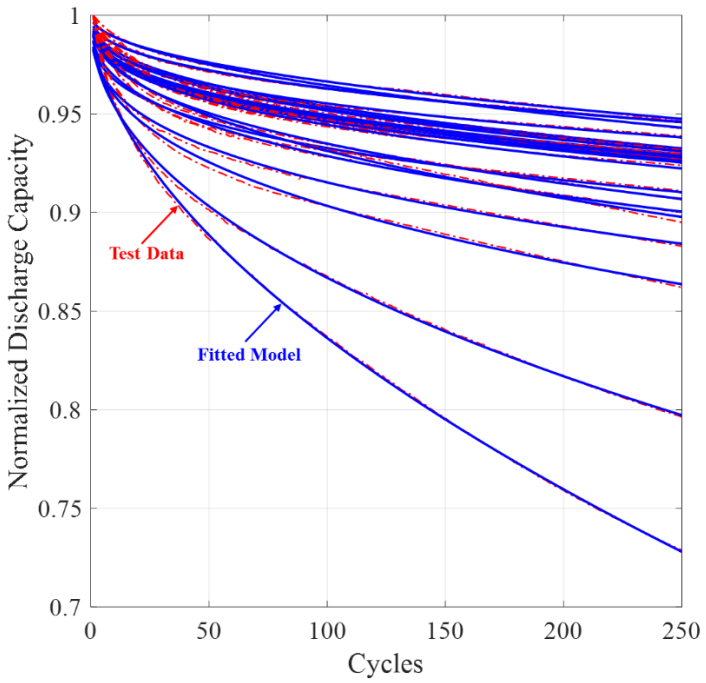


**Figure 4.2.** Comparison of model fits with individual battery capacity fade data (all C-rates) for a battery population.

The estimated individual values of transformed model parameters $logK_{1C}$ and *logb* for 24 batteries in have been used to perform Royston's H Test [56] for multivariate normality using R-package MVN [57]. A p-value of 0.09 shows that the transformed parameters $logK_{1C}$ and *logb* have bivariate normal distribution at a significance level of 0.05 and hence the assumption of normality in Equation (4.21) is reasonable after the log transformation.

The modeling framework presented in this study is generic enough for its application to any Li-ion battery accelerated capacity fade data and is useful for extrapolating and analyzing the capacity fade at lower (normal) operating C-rates based on the available testing data at accelerated C-rate levels up to 2C. The modeling approach considers the capacity fade trends and not the failure time distribution as required in conventional accelerated life analysis. Hence,

the capacity fade data of batteries that have not reached the failure threshold can be used in this modeling avoiding the need for running the tests up to end of life (EOL).

# Chapter 5: Stress Factor Ranking

Accelerated testing is conducted by increasing certain stress factors to increase the degradation rate and precipitate failure earlier than normal [51],[35]. The cyclic operation of batteries can be characterized by seven primary stress factors: ambient temperature, discharge C-rate, charge C-rate, constant voltage charge cut-off C-rate, depth of discharge (DOD), rest time after charge, and rest time after discharge. Some or all these stress factors can be selected to accelerate the battery degradation process. However, the effects of these stress factors on battery degradation are not uniform, and some factors can have more of an impact than others. Additionally, multifactorial and interdependent stress factors may work in combination to accelerate certain failure modes. It is not usually feasible to design a test matrix with many factors due to limited testing resources. Therefore, to achieve an optimal time reduction with the fewest stress factors, it is necessary to identify the most impactful stress factors and utilize them for accelerated testing.

The findings from the past studies reveal that there is no one general rule that can describe the effect of a particular stress factor on battery degradation due to the wide variety of Li-ion battery chemistries. Even for the same chemistry, different manufacturers use different designs (pouch, stacked/jellyroll, cylindrical, coin) and material additives (electrode coatings, electrolyte additives) that can change the long-term capacity fade behavior of batteries. Hence, the conclusions from each of these experimental studies are limited in terms of generalization. With continuous advances in battery materials, additives, and designs, it is difficult to predict

the effect of various stress factors on battery degradation based on the literature and thus the most influential stress factors cannot be determined.

The prior studies have also been limited in terms of the number of factors and the statistical interpretation of the effects of the factors on battery degradation, which is critical due to the variabilities associated with different batteries, production lots, manufacturers, and chemistries. Prochazka et al. [58] and Su et al. [59] are the two studies that attempted to fill this research gap. Advancing on their work, this study presents a methodology to conduct a multi-stress DOE consisting of stress factors that are relevant for the practical cycle testing of batteries. This includes the selection of the range of stress factors that can be represented by just 2 levels, a reduction in the number of tests using half-fractional designs, and the utilization of machine learning technique least absolute shrinkage and selection operator (LASSO) in addition to conventional least squares linear regression, to identify the statistical significance and ranking of main and two-way interaction of stress factors for accelerated battery test planning in a short period of time (i.e., limited to 2 months). This stress factor ranking approach uses data from commercial Li-ion pouch batteries. The approach is designed to be transferable and can be used for any type of battery chemistry. Five different stress factors of ambient temperature, discharge C-rate, charge C-rate, constant-voltage charge cut-off current, and DOD are investigated. These stress factors constitute the conventional cycling profile used in most of the battery qualification test plans, and their impact in terms of battery capacity fade acceleration is ranked using DOE.

## 5.1 Design of Experiment

A design of experiment (DOE) has been used to conduct the cycle testing of batteries with 5 different stress factors: ambient temperature, discharge C-rate, charge C-rate, charge cut-off current, and DOD. The DOE approach is designed to be general in its architecture as to enable

the inclusion of additional factors or to exclude some of the selected factors. Two levels for each selected stress factor have been chosen to cover the entire range of the stress factor. The purpose of this study is to screen the stress factors and rank them in terms of their importance for battery capacity fade acceleration, therefore, two levels are sufficient for each stress factor. The DOE for the testing is as follows:

**Factors:** $k = 5$, $X_1 = T,\ X_2 = Discharge\ C-rate,\ X_3 = Charge\ Cut-off,$

$$X_4 = Charge\ C-rate,\ X_5 = DOD$$

$$DOD = \frac{I*t}{Q_N} \tag{5.1}$$

where $k$ is the number of stress factors, $I$ is the constant discharge current, $t$ is the discharge time, $Q_N$ is battery capacity after $N$ cycles, and $T$ is the test (environmental) temperature.

**Levels:** $L_1 = 2,\ L_2 = 2,\ L_3 = 2,\ L_4 = 2,\ L_5 = 2$

A full factorial DOE is considered the most comprehensive as it considers all the main and higher-order interaction effects. A full factorial design ($2^k$) for this test will involve $N = L_1 \cdot L_2 \cdot L_3 \cdot L_4 \cdot L_5 = 32$ test cases. Third or higher-order interaction effects of stress factors are usually insignificant in most practical cases and can be aliased with main and two-way interaction effects. A half-fractional factorial design is sufficient to extract individual and two-way interaction effects of stress factors and also helps reduce the number of test cases by half compared to full factorial design. In half-fractional design one of the stress factors is represented as a logical multiplication of the remaining four or a lower number of stress factors.

**Table 5.1.** Half fractional factorial DOE.

| Experiment No. | Temperature (ºC) (X1) | Discharge C-rate (X2) | Charge Cut-off (X3) | Charge C-rate (X4) | DOD (X5 = X1·X2·X3·X4) |
|---|---|---|---|---|---|
| 1 | 25 (L) | 0.5C (L)* | 0.01C (H)* | 0.8C (L) | 0.5 (L) |
| 2 | 25 (L) | 0.5C (L) | 0.01C (H) | 1.2C (H) | 1 (H) |
| 3 | 25 | 0.5C | 0.2C (L) | 0.8C | 1 |
| 4 | 25 | 0.5C | 0.2C | 1.2C | 0.5 |
| 5 | 25 | 1.3C (H) | 0.01C | 0.8C | 1 |
| 6 | 25 | 1.3C | 0.01C | 1.2C | 0.5 |
| 7 | 25 | 1.3C | 0.2C | 0.8C | 0.5 |
| 8 | 25 | 1.3C | 0.2C | 1.2C | 1 |
| 9 | 55 (H) | 0.5C | 0.01C | 0.8C | 1 |
| 10 | 55 | 0.5C | 0.01C | 1.2C | 0.5 |
| 11 | 55 | 0.5C | 0.2C | 0.8C | 0.5 |
| 12 | 55 | 0.5C | 0.2C | 1.2C | 1 |
| 13 | 55 | 1.3C | 0.01C | 0.8C | 0.5 |
| 14 | 55 | 1.3C | 0.01C | 1.2C | 1 |
| 15 | 55 | 1.3C | 0.2C | 0.8C | 1 |
| 16 | 55 | 1.3C | 0.2C | 1.2C | 0.5 |

*H – High (+1), L – Low (-1)

Table 5.1 shows the process of representing DOD (X5) as a function of the remaining four stress factors in the proposed design. The generator or word for the design in Table 1 is +X1·X2·X3·X4·X5 as the multiplication of all these variables will always be I (+1 or H). The design in Table 1 is resolution V design, where the main effects are aliased with at least fourth-order effects and the second-order effects are aliased with at least third-order effects. In order to understand the repeatability of results, 3 samples per test case have been considered and a total of 48 batteries have been tested.

All the test cases described in Table 5.1 involved continuous cycling of a Li-ion battery under the specified stress factors to characterize the capacity fade trend. The cycling profile included charge/discharge operations. The charging operation was conducted using a constant-current/constant-voltage (CCCV) standard charge algorithm. The battery was charged using the prescribed constant-charge C-rate up to the end-of-charge voltage (4.4 V) followed by the 'top-up' using constant voltage charging until the charging current dropped below the prescribed charge cut-off. The discharge operation was performed using the prescribed constant discharge C-rate until the prescribed DOD was achieved. 100% DOD has been defined as the discharge to 3 V at 0.5C discharge current rate. Hence, for high discharge current tests (1.3C), the batteries were further discharged to 3 V at 0.5C after hitting the 3 V threshold at the prescribed high level (1.3C) of discharge C-rate. Rest times after discharge and after charge were not considered as stress factors in this study and were kept fixed at 10 min for the testing.

The cell characterization testing was conducted at the beginning of cycling testing (Table 5.1) to set up the baseline and intermediately between the cycling tests for comparison with baseline characteristics. The characterization testing included the measurements of "true" battery discharge capacity. This true value of discharge capacity has been defined at a standard condition for comparison across different tests in Table 5.1. Discharge capacity measurement tests were conducted by cycling the battery at 25 $^{o}$C ambient temperature using a standard full

charge/discharge cycle. The battery was charged at 0.8C constant current up to the end-of-charge voltage (4.4 V) followed by the constant voltage charging until the charging current dropped below C/20. Following the 10 min of rest after the charging, the battery was discharged at C/2 constant current up to the end-of-discharge voltage (3 V). After discharge, a 10-min rest period was provided before charging the battery for the next cycle. For the initial capacity measurements of fresh cells, 5 cycles were conducted, and the average value of the discharge capacities was used as the initial capacity. For the capacity measurements at prescribed intervals and at the end of the cycling testing, 2 cycles were conducted and the discharge capacity from the second cycle was used as the real capacity measurement. The intermediate characterization of discharge capacity was conducted at fixed intervals of 100 cycles.

## 5.2 Algorithms for Stress Factor Ranking

Two statistical and machine learning algorithms, including least squares linear regression and LASSO regression were considered for evaluating the effects of the stress factors on battery capacity fade and for ranking them in terms of their impact. The task of identifying the highest contributing features for prediction is termed “feature selection” and is generally applied in datasets where the number of features exceeds the order of hundreds. The primary goal of feature selection is a reduction in computational time and memory. However, the present work makes use of feature selection for stress factor ranking in order of importance to capacity fade. Linear regression has mainly been used for comparison as a conventional method for evaluating the DOEs. The problem can be specified mathematically as follows:

$$Y = f(X) + \varepsilon \tag{5.2}$$

$$X = (X1, X2, X3, X4, X5) \tag{5.3}$$

where $Y$ is the response variable; $X$ is the matrix of predictor variables (stress factors); and $\varepsilon$ is the random error term, which is independent of $X$ and has zero mean. The purpose of all three algorithms is to learn the unknown function $f$ and understand how $Y$ is affected by $X1, X2,..,X5$. Hence these algorithms were used in this paper mainly for *inference* rather than *prediction* [60].

The average capacity fade rate was used as the response variable $Y$ in Equation (5.2). It was calculated by dividing the total drop in capacity (Ah) with the cumulative discharge (Ah), which is defined as the total amount of charge (Ah) delivered by the battery during the discharge operations of the entire testing. Cumulative discharge was selected in the denominator of Equation (5.4) in place of number of cycles because a cycle with 50% DOD cannot be directly compared with a cycle with 100% DOD.

$$Y = \frac{\Delta\, Capacity\ (\text{Ah})}{Cumulative\ Discharge\ (\text{Ah})} \tag{5.4}$$

The estimation of $f$ requires training data generated by the cycle testing of batteries as per the DOE described in Table 5.1. The least squares linear regression and LASSO regression fall into the parametric category, where an assumption about the functional form of $f$ is made in advance and then training data is used to estimate the coefficients.

$$f(X) = \beta_0 + \beta_1 X1 + \beta_2 X2 + \beta_3 X3 + \beta_4 X4 + \beta_5 X5 + \varepsilon \tag{5.5}$$

The linear regression for five stress factors can be described by Equation (5.5), where $\beta_0, \beta_1,..,\beta_5$ are the regression coefficients that need to be estimated. The most conventional algorithm to

estimate these coefficients is least squares, which tries to minimize the residual sum of squares (RSS), which is defined as follows:

$$RSS = \sum_{i=1}^{n}\left(y_i - \widehat{f(x_i)}\right)^2 \tag{5.6}$$

$$= \sum_{i=1}^{n}\left(y_i - \widehat{\beta_0} - \widehat{\beta_1}x_{i1} - \widehat{\beta_2}x_{i2} - \widehat{\beta_3}x_{i3} - \widehat{\beta_4}x_{i4} - \widehat{\beta_5}x_{i5}\right)^2$$

where $\hat{f}$ is an estimate of function *f*; $\widehat{\beta_0}, \widehat{\beta_1}, \ldots, \widehat{\beta_5}$ are estimates of $\beta_0, \beta_1, .., \beta_5$, respectively; *n* is the number of training observations. The first question of *inference* is whether any of the predictor variable is required to explain the output. This is usually answered using hypothesis testing based on F-statistics described as follows:

$$H_0: \beta_0 = \beta_1 = \beta_2 = \beta_3 = \beta_4 = \beta_5 = 0$$

$$H_1: At\ least\ one\ \beta_j\ is\ non - zero$$

$$F = \frac{(TSS - RSS)/p}{RSS/(n-p-1)} \tag{5.7}$$

$$TSS = \sum_{i=1}^{n}(y_i - \bar{y})^2$$

where TSS is the total sum of squares, *n* is the number of observations in the training data, and *p* is the number of predictor variables. Based on F-statistic, a *p*-value is calculated to decide on the null hypothesis. If the *p*-value is less than 0.05, then the null hypothesis will be rejected. The second question is which of these variables are statistically significant to explain the output. This has been addressed using the backward selection approach where all the variables

are first used for the model fit and then the variables with the largest *p*-values are removed one by one until a stopping criterion of model fit is met [60]. The model fit has been evaluated using an adjusted $R^2$ statistic which also takes into account the number of predictor variables and is based on the idea that after all the relevant variables have been included in the model, adding more variables would lead to only fitting the noise.

$$Adjusted\ R^2 = 1 - \frac{RSS/(n-p-1)}{TSS/(n-1)} \tag{5.8}$$

LASSO regression, a regularization technique developed for liner regression problems, has been widely used in the literature as a predictor variable selection algorithm due to its simplicity and ease of interpretation [61],[62]. The key assumption is that the best possible prediction rule is sparse, that is, only a few of the coefficients are different from zero. Coefficients different from zero are directly proportional to the variable's importance, the higher the regularizer at a non-zero weight, the more important the variable for the prediction. In LASSO regression, sparsity is achieved by adding a term that penalizes the loss based on convex relaxation via the $l_1$ norm and a regularization term $\lambda$. The loss function formula thus becomes:

$$min \sum_{i=1}^{n} \left(y_i - \widehat{f(x_i)}\ \right)^2 + \lambda \sum_{j=1}^{p} |\beta_j| \tag{5.9}$$

Equation (5.9) represents the summation of RSS (Equation (5.6) and a $l_1$ norm penalty term. $\lambda$ represents the regularization term. The higher the regularization term, the more the weights of the model shrink to zero, thus revealing the important predictor variables. A value of $\lambda = 0$ will make the LASSO regression the same as the least squares linear regression. In a way, LASSO

is an alternative to the variable selection approach such as backward selection discussed for the linear regression model. The value of $\lambda$ has been chosen based on the 10-fold cross-validation approach. In this approach, the training data is randomly divided into 10 parts or folds, and the first fold is treated as the validation set while the remaining 9 folds are used for training purposes. This process is repeated 10 times to choose each one of those 10 folds as the validation set, and the mean squared error is calculated for each validation set. The final mean squared error is calculated as follows:

$$MSE = \frac{1}{10}\sum_{i=1}^{10} MSE_i \tag{5.10}$$

A value of $\lambda$ that minimizes the MSE can be chosen. However, in order to use a slightly larger value of $\lambda$, which allows stricter penalty on coefficients, a value of $\lambda$ corresponding to the MSE, which is higher by one standard deviation from the minimum MSE, is chosen in this paper. Additionally, unlike the linear regression, the LASSO regression does not perform any statistical hypothesis testing to evaluate whether the individual variables are statistically significant for the response. Hence, a non-parametric bootstrap method [63] has been used to calculate the probability of each coefficient in the regression model being zero using a 1000-sample size. In the bootstrap method, a training sample of size *n* same as that of the actual training data is randomly sampled with replacement and for this sample the 10-fold cross-validation is conducted to select $\lambda$ corresponding to MSE at one standard deviation and calculate corresponding estimates of coefficients. This process is repeated 1000 times, and then the probability of 0 is calculated for each coefficient.

$$Bootstrap\ Probabilty\ of\ (\beta_j = 0) = \frac{1}{1000}(number\ of\ times\ \beta_j = 0) \tag{5.11}$$

## 5.3 Results and Discussion

The pouch graphite-$LiCoO_2$ batteries with a minimum capacity of 4.45 Ah at 0.2C rate and voltage range of 4.4 V to 3 V have been used for the testing. The capacity fade results are presented in Figure 5.1. Data for all three samples under each test case are plotted. The batteries show a large capacity fade rate for 55 $^oC$ and 1.3C test conditions (Tests 13-15) in Figure 5.1. Surprisingly, batteries under test cases 9 and 10 at 55 $^oC$ and 0.5C test conditions show more capacity fade than that at Test 16 under 55 $^oC$ and 1.3C conditions. Test 9 has higher stress in terms of charge cut-off current and DOD as compared to Test 16, while Test 10 has only higher charge cut-off as higher stress as compared to Test 16. One of the 25 $^oC$ and 2C cases (Test 8) also shows a higher capacity fade rate. The average capacity fade rate for each test case and sample is plotted in Figure 5.2. The capacity fade rate is much higher for test cases at 55 $^oC$ (Tests 9-16).

The inclusion of DOD leads to 5 main effects and 10 two-way interaction effects of stress factors, which should be estimated from the 16 test conditions described in Table 5.1. The number of test conditions is sufficient to estimate all the relevant effects in one step using least squares linear regression. While fitting the model, it was observed that $ln(Y)$ provides a better fit for a linear model, and hence for these batteries $ln(Y)$ has been used as the response variable subsequently for linear and LASSO regression. All the predictor variables have been standardized using the z-score method prior to model fitting. Using the least squares linear regression, the response $ln(Y)$ is fitted as a function of all 15 predictor variables. The model fit results in an adjusted $R^2$ value of 0.89, which suggests a decent fit. Figure 5.3 shows the ordering of the coefficients based on the negative $\log_{10}()$ of *p*-values associated with the *t*-statistic. The *t*-statistic is defined as the ratio of coefficient estimate and corresponding standard error and is used for testing the null hypothesis that the coefficient estimate is zero, and hence the predictor variable has no effect on the response *Y*. A *p*-value of less than 0.05 suggests that

this null hypothesis can be rejected, therefore, the predictor variable is related to the response after adjusting for the other predictor variables.

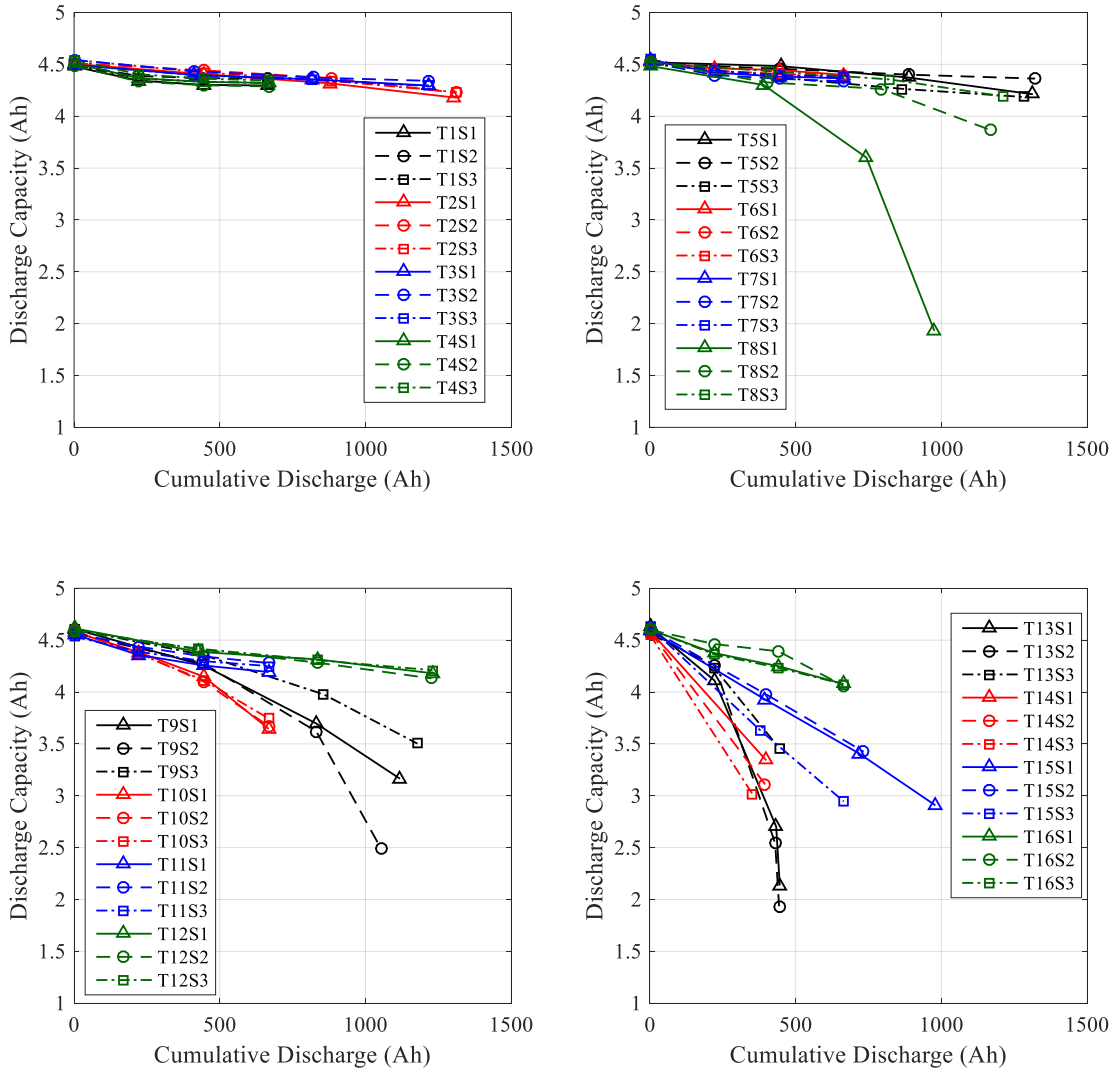


Figure 5.1. Variation of normalized discharge capacity with cumulative discharge (Ah).

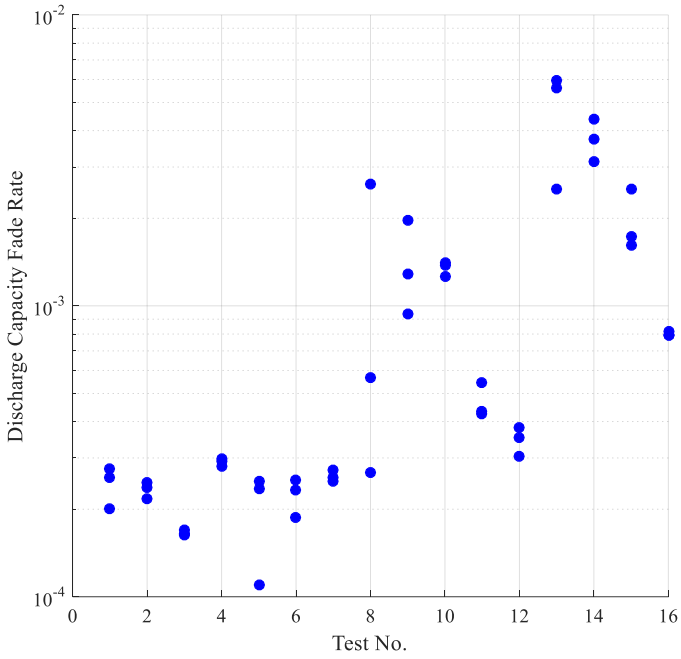


Figure 5.2. Capacity fade rate (*Y*) of batteries for Tests 1-16.

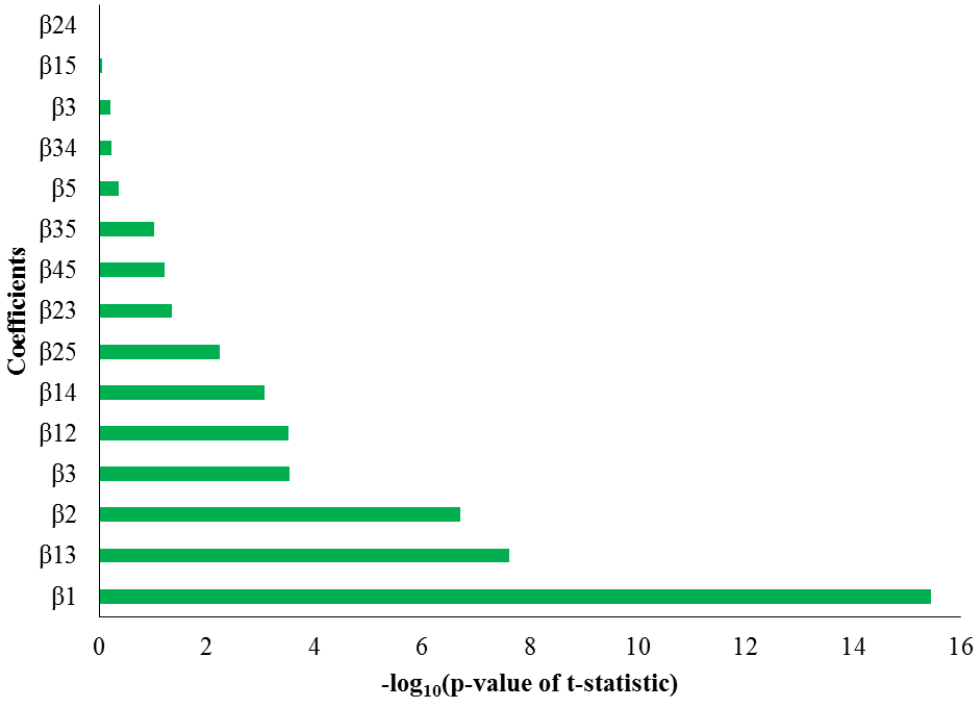


Figure 5.3. Bar graph with ordering of predictor variable estimates based on the *p*-value of the *t*-statistic.

**Table 5.2.** Results from the least squares regression model fit using the selected main and interaction effects of stress factors.

| Predictor Variable | Coefficient | Estimate | Std Error | *t*-statistic | Prob>\|*t*\| |
|---|---|---|---|---|---|
| Intercept | β0 | -7.456353 | 0.050295 | -148.3 | <.0001 |
| Temperature | β1 | 0.8033906 | 0.050827 | 15.81 | <.0001 |
| Discharge C-rate | β2 | 0.3485357 | 0.050827 | 6.86 | <.0001 |
| Charge Current Cut-off | β3 | -0.215292 | 0.050827 | -4.24 | 0.0002 |
| Charge C-rate | β4 | 0.0259805 | 0.050827 | 0.51 | 0.6125 |
| DOD | β5 | 0.0420996 | 0.050827 | 0.83 | 0.4131 |
| Temperature × Discharge C-rate | β12 | 0.2168985 | 0.051365 | 4.22 | 0.0002 |
| Temperature × Charge Current Cut-off | β13 | -0.392352 | 0.051365 | -7.64 | <.0001 |
| Temperature × Charge C-rate | β14 | -0.196501 | 0.051365 | -3.83 | 0.0005 |
| Discharge C-rate × Charge Current Cut-off | β23 | 0.1112182 | 0.051365 | 2.17 | 0.0373 |
| Discharge C-rate × DOD | β25 | 0.1580237 | 0.051365 | 3.08 | 0.0041 |
| Charge Current Cut-off × DOD | β35 | 0.0917828 | 0.051365 | 1.79 | 0.0826 |
| Charge C-rate × DOD | β45 | 0.1040126 | 0.051365 | 2.02 | 0.0506 |

Using the backward selection approach, one predictor variable at a time was removed and its effect of adjusted $R^2$ was evaluated. The variable with the least $-\log_{10}$(p-value) was removed first. It is important to note that as a rule the main effects should not be excluded if their

interaction effects are included in the model. During this backward selection process, it was observed that adjusted $R^2$ increases up to 0.90 and then it starts to decrease again. Hence the model associated with the highest adjusted $R^2$ value was finally chosen and corresponding coefficient estimates are shown in Table 5.2. The *F*-statistic (Equation (5.7)) for the fit is 35.67, which corresponds to a *p*-value of less than 0.05, and hence the null hypothesis that none of the variables are useful in predicting the response can be rejected. Table 5.2 shows that charge C-rate, DOD, and their interaction are not statistically significant ($p > 0.05$) for modeling the response $ln(Y)$ and can be further removed with very little drop in the value of adjusted $R^2$.

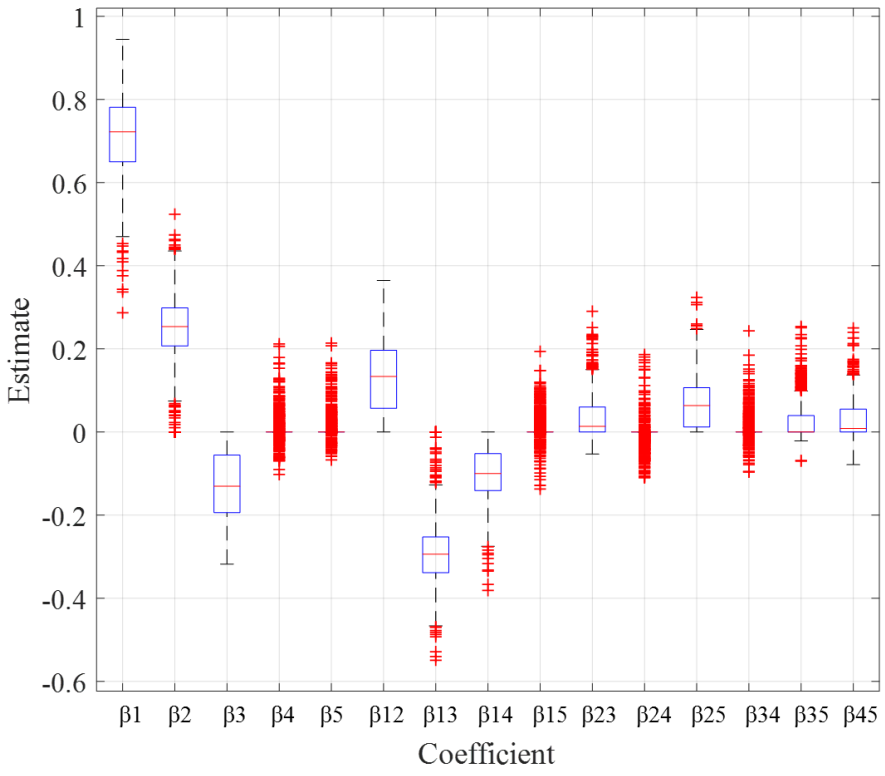


Figure 5.4. Box plots of coefficient estimates generated from bootstrap LASSO.

LASSO regression analysis was performed with all 15 main and two-way interaction effects predictor variables using data from all 16 test conditions mentioned in Table 5.1. Figure 5.4

shows the box plots of all 15 coefficient estimates generated from bootstrap LASSO using $\lambda$ corresponding to one standard deviation MSE in a 10-fold cross-validation. The median estimate is roughly zero for coefficients β4, β5, β15, β24, β34, β35, and β45. Among these coefficients, β15, β24, and β34 were dropped in the backward selection approach and the remaining β4, β5, β35, and β45 show *p*-values greater than 0.05 in Table 5.2. Hence, LASSO automatically identifies the predictor variables useful for describing response $ln(Y)$. Figure 5.5 shows the ordering of predictor variables using a bootstrap probability of 0. The ordering is close to what is observed in Figure 9 with a few exceptions. As per LASSO also, temperature, interaction of temperature and charge current cut-off, and discharge C-rate are the three most influential predictor variables.

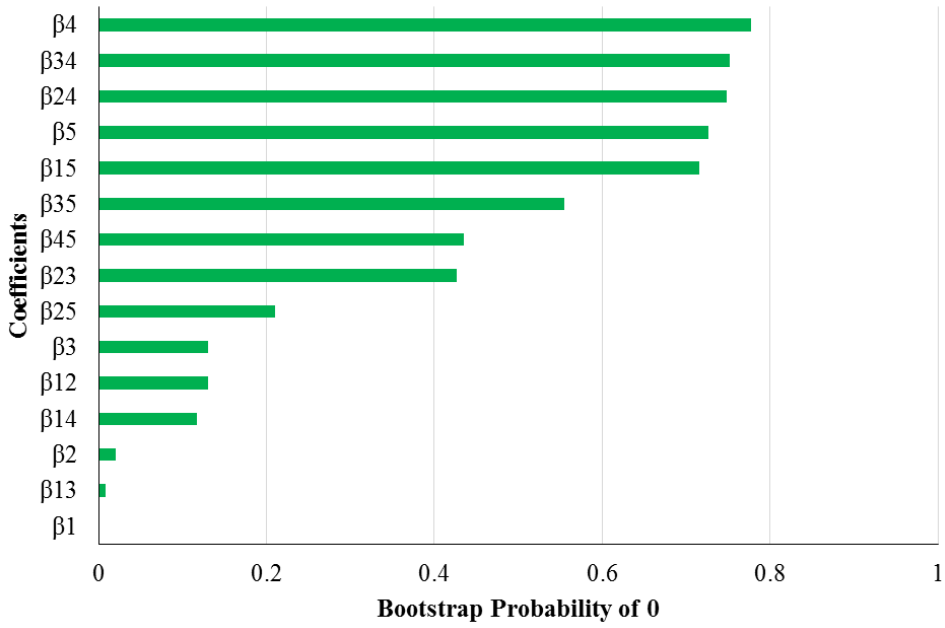


Figure 5.5. Ordering of coefficients in terms of their bootstrap probability of 0.

## 5.4 Conclusions

This chapter presents a methodology to select the most significant stress factors which can be used to plan accelerated degradation testing. The approach requires a one-time implementation of the design of experiments for each new type of battery. Two algorithms including least squares linear regression and bootstrapped least absolute shrinkage and selection operator (LAASO) regression have been presented for modeling the relation between capacity fade rate output and stress factor inputs and for stress factor ranking. LASSO, an extension of least squares regression, is specifically designed for feature ranking due to the addition of penalty on model parameters. LASSO is well-suited for cases where the number of features (stress factors) is higher than the number of samples (test conditions).

The results from these algorithms provide quantitative evidence that neither the main effects nor the interaction effects of charge C-rate and depth of discharge (DOD) feature in the top 3 significant stress factors for capacity fade in the graphite-$LiCoO_2$ batteries. An increase of 10 $^oC$ in temperature and reduction of charge cut-off to 0.05C will cause the capacity fade rate to increase approximately 1.5 times compared to that at 25 $^oC$, 0.5C discharge, 0.8C charge, 0.2C charge cut-off, and 100% DOD cycling condition as per the linear regression model parameters. Considering the proposed approach do not require the knowledge of battery chemistry, it can also be used for chemistries other than graphite-$LiCoO_2$. Early identification of the significant factors for any new battery type can prevent wastage of resources spent conducting large and futile design of experiments. Once the factor ranking list is determined, either the highest ranked factor or a combination of the first two ranked factors can be used with three levels for future accelerated degradation testing and for developing a nonlinear capacity fade model.

# Chapter 6: Role of Open Rest Condition

This study focuses on the effect of rest time after full charge operation on the degradation of graphite/$LiCoO_2$ pouch batteries under four different temperatures. Relation between rest time and battery state of charge has been investigated to understand how the rest time plays a role in battery degradation. A capacity fade trend modeling analysis has been conducted and applied to the experimental data of graphite/$LiCoO_2$ pouch batteries from five different manufacturers.

## 6.1 Experimental Design and Procedure

A test matrix was designed to study the effects of open rest time after full charge on graphite/$LiCoO_2$ battery capacity fade under four different ambient temperatures. Table 1 lists the tests that were conducted. The open rest time durations were 0.17 h, 2 h, 6 h, 12 h, 24 h, 360 h. One float rest time condition of 240 h was also included.

Except for the 360 h and 240 h (float) tests, all other tests described in Table 6.1 involve continuous cycling of Li-ion batteries under the specified stress factors. The cycling profile includes charge and discharge operations. The charging operation was conducted using constant current constant voltage (CCCV) standard charge algorithm. The battery was charged using 0.8C constant charge C-rate up to the end-of-charge voltage (4.4 V), followed by the 'top-up' using constant voltage charging until the charging current drops below C/20. The discharge operation was performed using 0.5C constant discharge C-rate until the end-of-

discharge voltage of 3 V was reached. Rest times after discharge were kept constant at 0.17 h, and rest times after charge were chosen as per Table 6.1.

**Table 6.1.** Tests matrix.

| **Ambient Temperature (°C)** | **Rest Time after Full Charge** | | | | | | | **Remarks** | **Characterization Tests for "True" Capacity Measurement** |
|---|---|---|---|---|---|---|---|---|---|
| | 0.17 h (open) | 2 h (open) | 6 h (open) | 12 h (open) | 24 h (open) | 360 h (simulates open storage) | 240 h (simulates float storage) | | |
| 25 | × | | | | × | | | Group 1- 3 samples per test case, tests conducted by battery manufacturers | Average of capacities of 5 full cycles in the beginning, 2 full cycles at regular intervals with 2nd cycle capacity considered as true capacity |
| 35 | × | | | × | × | | | | |
| 45 | × | | | × | × | | | | |
| 55 | × | | | × | × | | | | |
| 45 | | * | * | | | | | Group 2 - 2 samples per test case, tests conducted by the authors | Average of capacities of 5 full cycles in the beginning, 2 full cycles at regular intervals with 2nd cycle capacity considered as true capacity |
| 45 | + | | | | + | + | + | Group 3 - 2 samples per test case, tests conducted by the authors | 1 full cycle in the beginning and at regular intervals |
| 55 | + | | | | + | | | | |

The battery characterization testing was conducted at the beginning of the tests described in Table 6.1 to set up the baseline and intermediately between those tests for comparison with baseline characteristics. The characterization testing included the measurements of "true" battery discharge capacity. This true value of discharge capacity was defined as a standard condition for comparison across different tests in Table 6.1. Discharge capacity measurement tests were conducted by cycling the battery at room temperature (25 ± 3 °C) using a standard

full charge/discharge cycle. The battery was charged at 0.8C constant current up to the end-of-charge voltage (4.4 V), followed by constant voltage charging until the charging current dropped below C/20. After 0.17 h of rest after the charging, the battery was discharged at 0.5C constant current up to the end-of-discharge voltage (3 V). After discharge, a 0.17 h rest period was provided before charging the battery for the next cycle.

## 6.2 Results and Discussion

The results for commercial graphite/$LiCoO_2$ pouch batteries from Manufacturer A are presented in this section. These batteries have a minimum capacity of 2.72 Ah at the constant discharge C-rate of 0.2C and in the voltage range of 3 V to 4.4 V. The energy dispersive X-ray spectroscopy of the positive electrode indicates the presence of iron (Fe) as well in very small amounts (<1.5 weight%). The batteries have a stacked design for electrodes. The electrolyte used in the batteries is proprietary and could not be determined. The separator is polymeric in nature, with a coating of aluminum oxide ($Al_2O_3$) on both sides. The positive and negative current collectors are made of aluminum (Al) and copper (Cu), respectively.

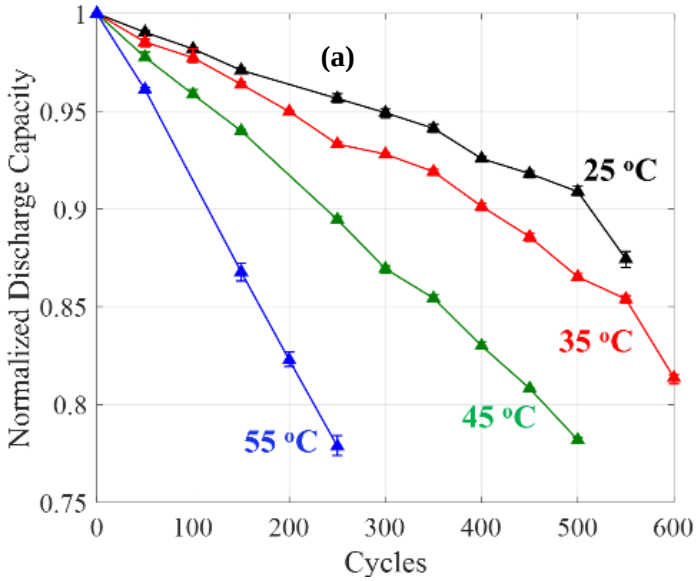

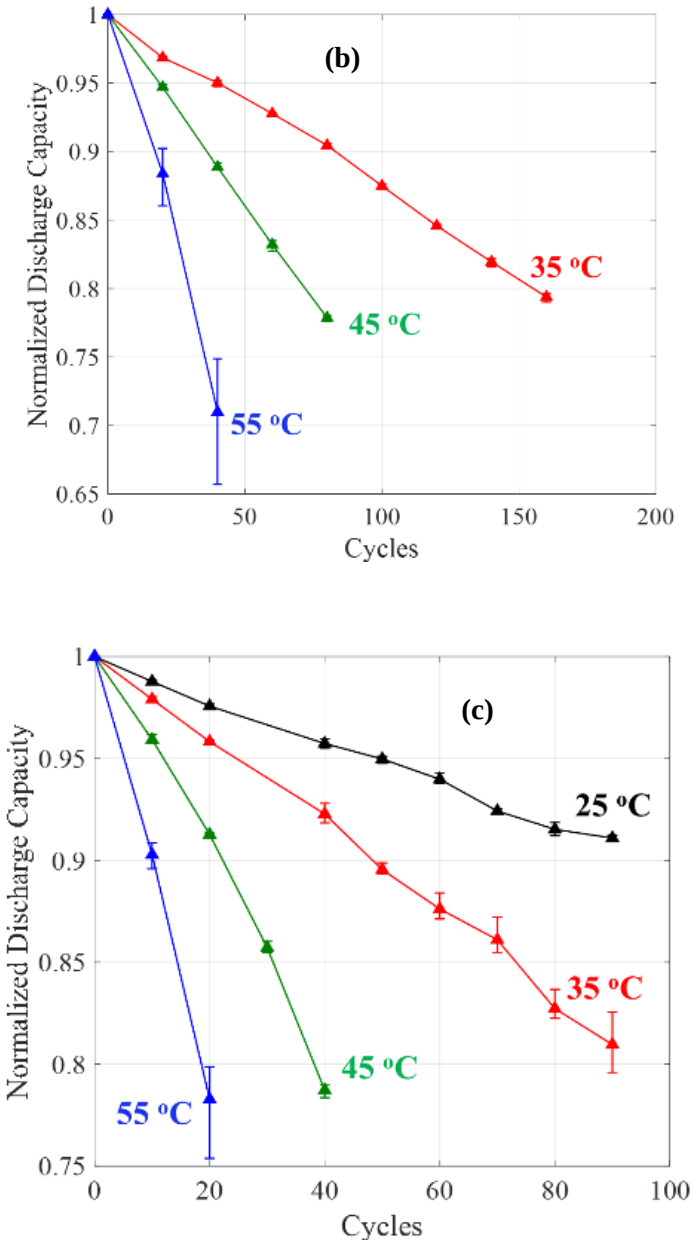


**Figure 6.1.** Variation of normalized discharge capacity with cycles for three different temperatures at a fixed rest time of (a) 0.17 h, (b) 12 h, and (c) 24 h based on data from the group 1.

The discharge capacity measured during the characterization testing was used as a metric for battery degradation. The results from the tests matrix (Table 6.1) can be broken down into two

parts: the effects of ambient temperature at constant rest time and the effects of rest time at constant ambient temperature. Figure 6.1 shows the plots for normalized discharge capacities vs the number of cycles at different temperatures and at three fixed rest times of 0.17 h, 12 h, and 24 h, respectively. Normalized discharge capacity is defined as the ratio of a degraded battery's discharge capacity to its initial discharge capacity, and it decreases with the number of cycles as the battery degrades. In the figure, the error bars show the maximum and minimum normalized discharge capacities among the three batteries (group 1), while the trend line shows the mean. It can be seen from the figure that temperature accelerates the rate of capacity fade at all three above-mentioned rest times. As batteries are electrochemical systems with electrochemical side reactions such as electrolyte reduction at the negative electrode and electrolyte oxidation at the positive electrode, it is expected that temperature should accelerate the rate of these reactions consuming more active lithium, a measure of battery capacity. The variations among degradation trends of 3 batteries under the same conditions are limited.

Similarly, the effects of rest time on battery degradation at fixed temperatures can be studied using Figures 6.2 and 6.3. In the figure, an additional variable of the total number of days has also been added in the plots as the cycles with different rest time may not be comparable among different tests due to the inclusion of long rest periods in conditions. Also, the inclusion of the number of days is required to understand the applicability of the rest time stress factor for accelerating the battery life testing. It is clear from Figures 6.2a, c, e and 6.3a, c that when cycles are considered as X-axis variables, the capacity fade rate increases and the number of cycles to reach a predefined threshold decreases significantly (almost 11 times at 55 $^{o}$C for 80% normalized discharge capacity threshold) with the increase in rest time after full charge. However, the same data with a different X-axis variable of time (Figures 6.2b, d, f and 6.3b) paints a different picture of the effects of rest time.

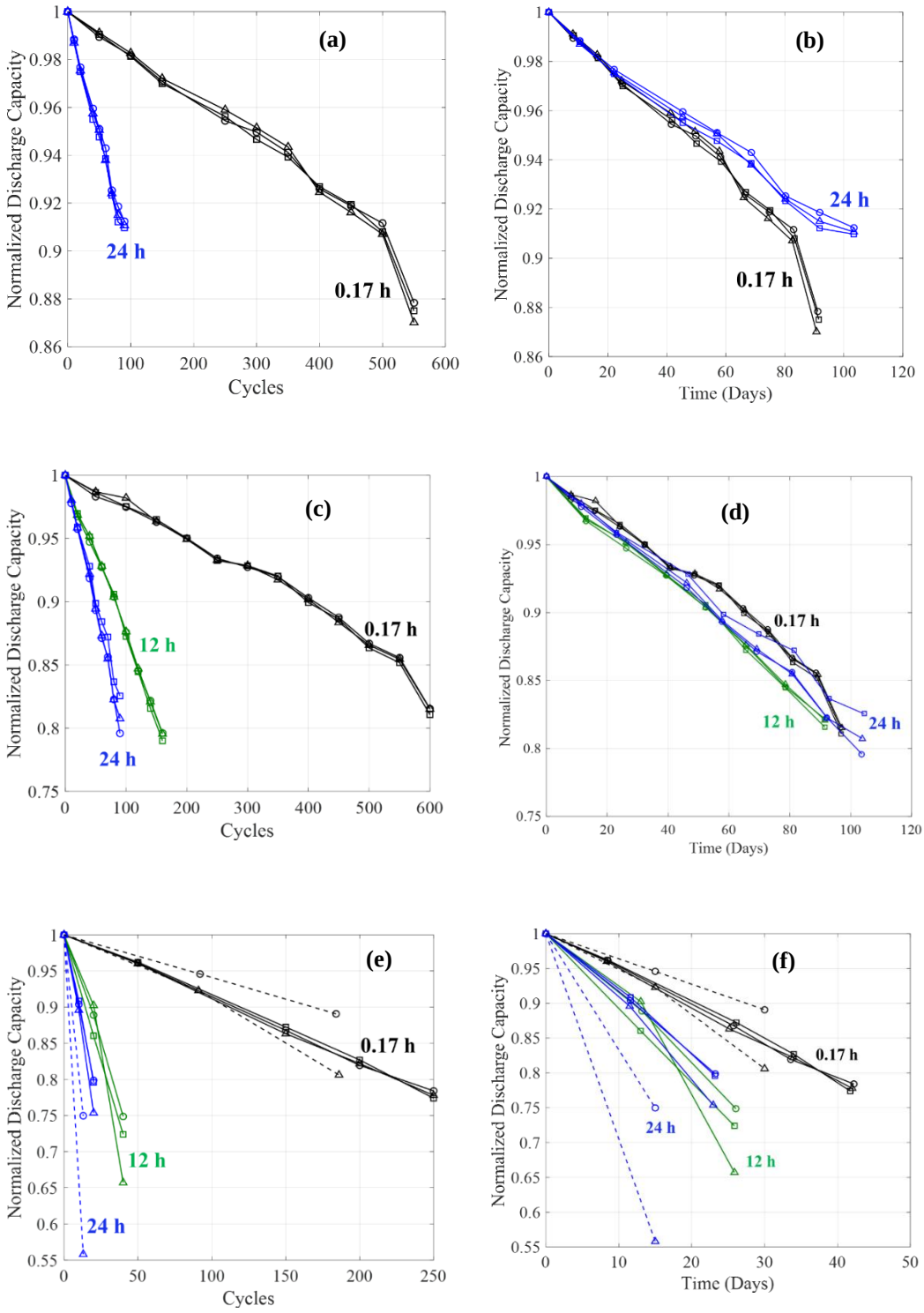


**Figure 6.2.** Effects of rest time on normalized discharge capacity using data from group 1 (solid lines – 3 samples) and group 3 (dashed lines – 2 samples) at (a) 25 $^{o}$C vs cycles, (b) at

25 $^{o}$C vs time, (c) at 35 $^{o}$C vs cycles, (d) at 35 $^{o}$C vs time, (e) at 55 $^{o}$C vs cycles, and (f) at 55 $^{o}$C vs time.

At 25 $^{o}$C the batteries under 24 h show lesser capacity fade per day compared to that for 0.17 h test. At 35 $^{o}$C, batteries under the different rest times show a similar capacity fade per day while those under 45 $^{o}$C and 55 $^{o}$C show an accelerated capacity fade rate at 12 h and 24 h rest conditions, leading to a roughly one-third time reduction as compared to 0.17 h test samples reaching 80% capacity. Hence normalized discharge capacity vs time trends for different rest times are strongly affected by the temperature in terms of their relative positioning (capacity fade rate). Some of the capacity fade trends at 12 h and 24 h continue to overlap even at elevated temperature conditions of 45 $^{o}$C and 55 $^{o}$C, suggesting that beyond a threshold value, rest time may not accelerate the degradation. These results raised the question if there was a lower value of rest time that could provide the same acceleration as that observed for 12 h and 24 h cases. To answer this question, additional tests at 2 h and 6 h rest periods (group 2) were added at 45 $^{o}$C temperature.

Figure 6.3a, b also shows additional trends at 2 h and 6 h rest periods at 45 $^{o}$C. Only 2 samples per test case were possible due to the limited availability of battery samples. With cycles as the X-variable, the capacity fade trends for 2 h and 6 h lie between those of 0.17 h and 12 h, indicating a monotonic increase in capacity fade rate with increasing rest time after charge. However, by considering the time (days) as the X-variable, one of the samples for the 6 h case shows an overlapping trend with those for 12 h and 24 h cases, and the other overlaps with those from the 2 h test case. Capacity fade trends for samples from the 2 h rest period test lie between those of samples from 0.17 h and samples from 12 h rest period tests. Comparing the time to reach 80% of initial capacity, there is a difference of roughly 10 days between the trends at 2 h and those at 24 h rest period.

The capacity fade acceleration with respect to time seems to follow an asymptotic (limiting) behavior as the rest time is increased up to 24 h. However, the data from group 1 and group 2 did not reveal whether this asymptotic behavior would continue even for longer rest durations of the battery in fully charged open and float conditions. Hence, the tests under group 3 were added for 360 h and 240 h (float) operations at 45 $^{o}$C. Tests for 0.17 h, 24 h at 45 $^{o}$C and 55 $^{o}$C were also added in this stage to prepare samples that could later be used for the investigation of degradation mechanisms.

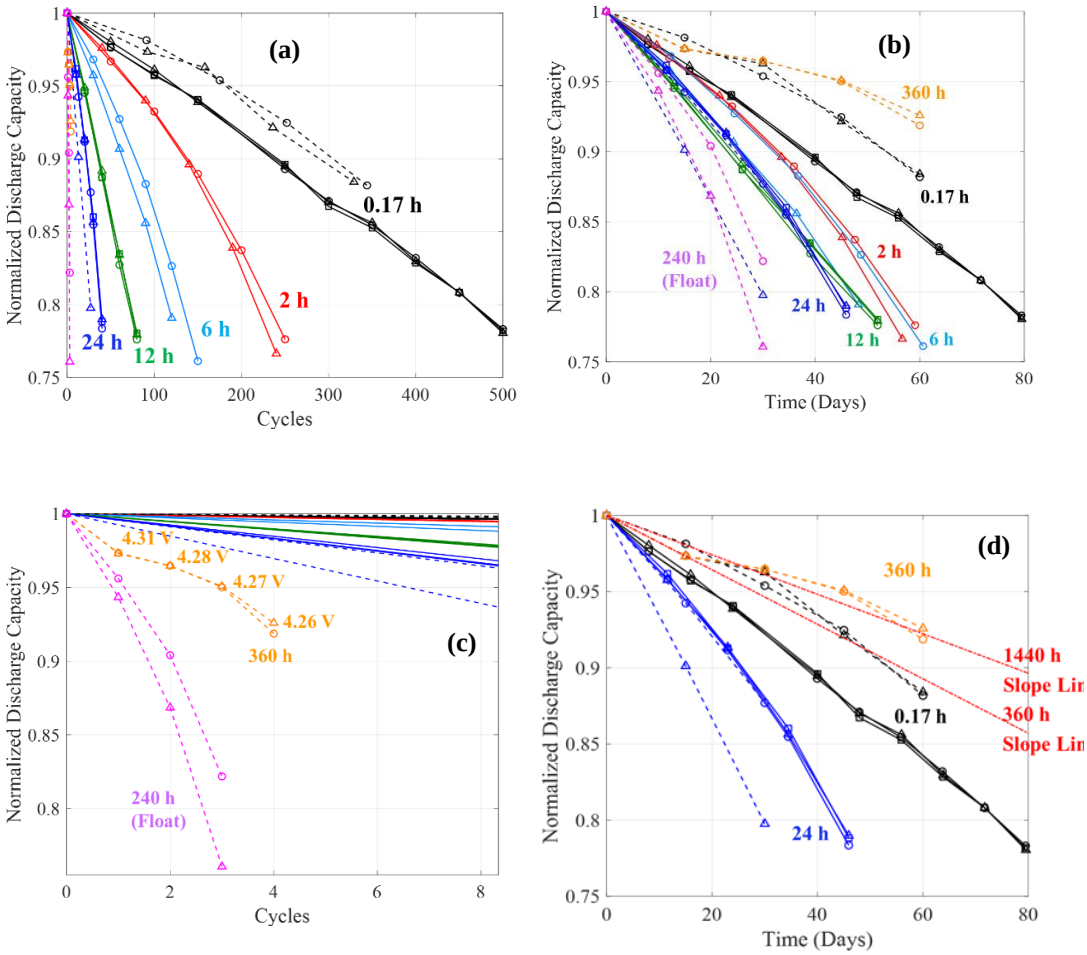

**Figure 6.3.** Normalized discharge capacity vs a) and c) cycles, b) test time (days) for all the tests (group 1 and group 2 - solid lines, group 3 - dashed lines) at 45 $^{o}$C, and d) 360 h test with slope lines indicating the possible capacity fade paths with constituting cycles of 15 days open rest and 60 days open rest after full charge.

In the 240 h (float) test, batteries were first charged using a CCCV profile up to 4.4 V and then left connected under constant voltage of 4.4 V during the entire test period except for the characterization cycles after every 10 days (240 h). In the 360 h test, batteries were initially charged using a CCCV profile of cycling tests up to 4.4 V (C/20 charge cut-off current) and then left open during the rest period of 360 h. In order to make the 360 h test similar to open storage operation, the batteries were charged after each characterization test only up to the terminal voltage recorded immediately before starting that characterization test. For example, if the terminal voltage dropped from 4.4 V to 4.31 V in the first 15 days (360 h), then after the characterization test, the battery was charged only up to 4.31 V. A CCCV charge profile with C/100 charge cut-off current was used to charge the batteries under 360 h test after the second and later characterization tests. A lower charge cut-off current of C/100 was chosen instead of C/20 to minimize charge redistribution related voltage drop.

360 h and 240 h (float) tests have been shown in Figure 6.3a, c with four and three (characterization) cycles, respectively. With an X-axis of cycles, the 360 h test follows the monotonically increasing relationship between capacity loss rate and rest time. However, with an X-axis of time, the 360 h test exhibits the lowest capacity fade rate, and the 240 h (float) test exhibits the highest capacity fade rate (Figure 6.3b). All other cycling tests with various rest periods lie in-between these two tests in terms of capacity fade per day. In Figure 6.3a, b the capacity loss trends for 0.17 h rest period case for group 1 and group 3 do not overlap. One of

the reasons for this mismatch is an interruption of cycling for 5-6 days for 0.17 h rest period case for group 3, and hence the batteries remained in open storage condition for that duration, resulting in the deceleration of the degradation process. Additionally, the differences in the capacity loss trends for group 1 and group 3 for 0.17 h and 24 h rest period cases are expected from the variations among samples and capacity characterization intervals (Figures 6.2e, f and 6.3a, b).

The 360 h test provides an interesting opportunity to study the effects of rest time after full charge on capacity fade trends. This test with a characterization test interval of 15 days can be considered as a combination of cycling tests with 4 different rest periods of 15 days, 30 days, 45 days, and 60 days (Figure 6.3d). It shows that beyond a certain value of rest time, capacity fade per day decreases with the increase in the rest time. At 25 $^{o}$C and 35 $^{o}$C, even 24 h rest condition shows lesser or similar capacity fade per day respectively compared to 0.17 h test indicating that the rest time beyond which the capacity fade per day starts to decrease is a function of temperature.

### *6.2.1 Generalization Across Manufacturers*

Pouch batteries from 4 other manufacturers (B, C, D, and E) were cycled under test conditions for group 1 in Table 6.1. Three samples were tested under each condition. The capacity fade trends of batteries are presented in Figures 6.4-6.7. In each figure, the error bars show the maximum and minimum normalized discharge capacities among the three samples, while the trend line shows the mean. While the batteries from these manufacturers are mostly based on graphite/$LiCoO_2$ electrode chemistry, they may differ in terms of various inactive materials as well as electrode additives. All these batteries are rated for the end-of-charge voltage of 4.4 V. They have minimum capacities of respectively 3.27 Ah, 4.41 Ah, 4.45 Ah, and 4.45 Ah at the constant discharge C-rate of 0.2C and in the voltage range of 3 V to 4.4 V.

Figures 6.4-6.7 show that the capacity fade rate with respect to cycles increases almost non-linearly with the increase in rest time at all the three temperatures. The batteries from Manufacturers B and D show better capacity retention compared to those from Manufacturer A at 25 $^{o}$C, 35 $^{o}$C, and 45 $^{o}$C. However, the capacity fade rate is sharply accelerated at 55 $^{o}$C for these manufacturers. The batteries from Manufacturer E exhibit better capacity retention compared to those from Manufacturer A at 35 $^{o}$C, 45 $^{o}$C, and 55 $^{o}$C. Data at 25 $^{o}$C was not available for this manufacturer. The batteries from Manufacturer C have almost a similar capacity fade behavior as those from Manufacturer A.

The batteries from different manufacturers show differences in the capacity fade rates of individual tests, 55 $^{o}$C temperature vs 35 $^{o}$C temperature performances, which are expected given the inherent differences in their mostly inactive materials and design. However, they show consistent behavior in terms of effects of rest time on capacity fade rate at all four temperatures, confirming the generalization of the results in this study.

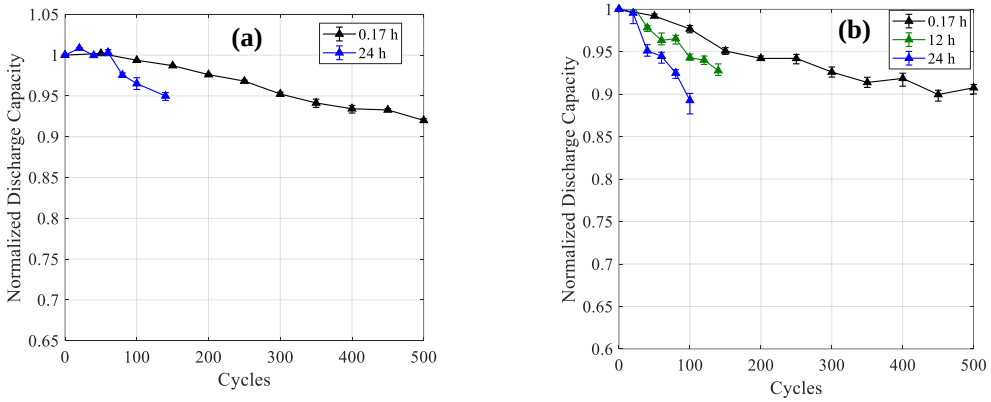

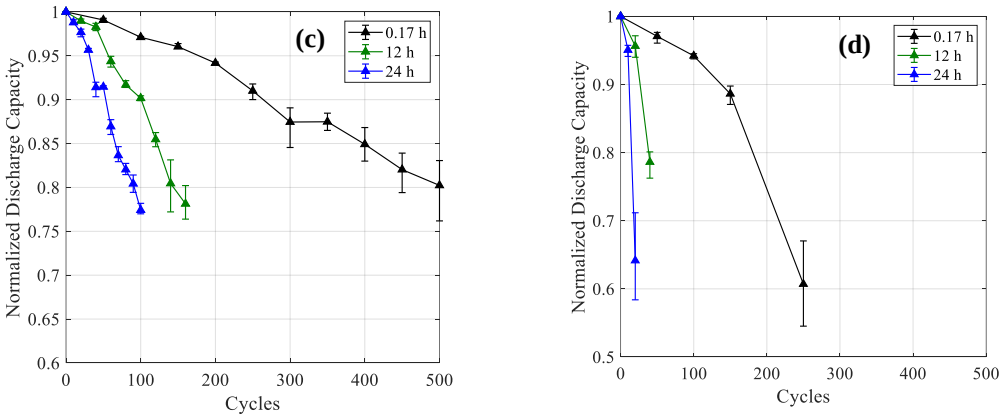


**Figure 6.4.** Normalized discharge capacity vs cycles for Manufacturer B at a) 25 $^{o}$C, b) 35 $^{o}$C, c) 45 $^{o}$C, and d) 55 $^{o}$C.

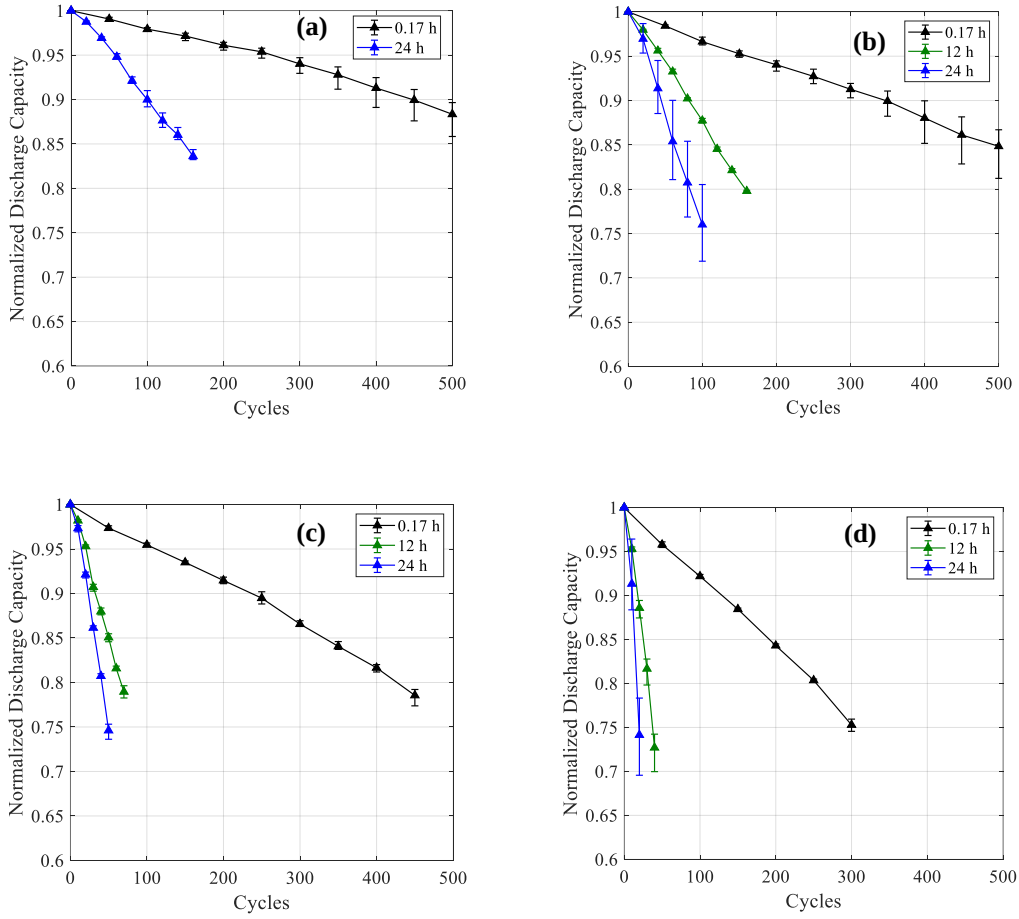

**Figure 6.5.** Normalized discharge capacity vs cycles for Manufacturer C at a) 25 $^{o}$C, b) 35 $^{o}$C, c) 45 $^{o}$C, and d) 55 $^{o}$C.

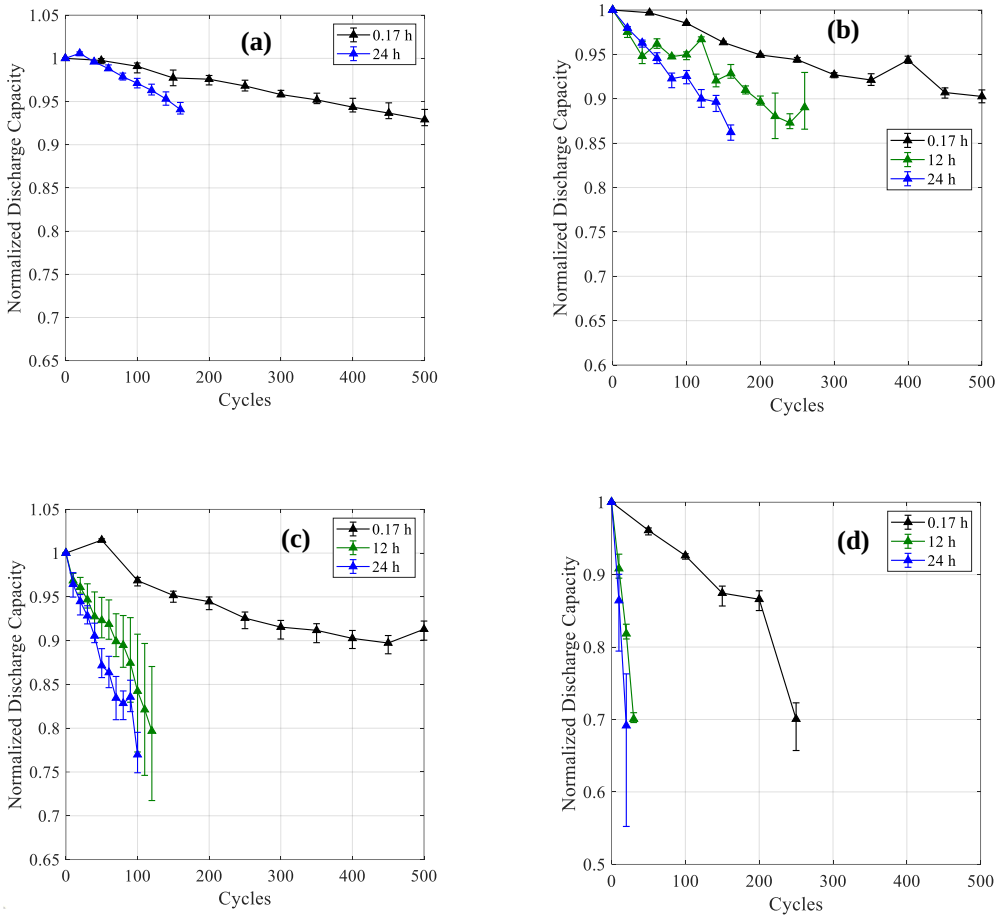


**Figure 6.6.** Normalized discharge capacity vs cycles for Manufacturer D at a) 25 $^{o}$C, b) 35 $^{o}$C, c) 45 $^{o}$C, and d) 55 $^{o}$C.

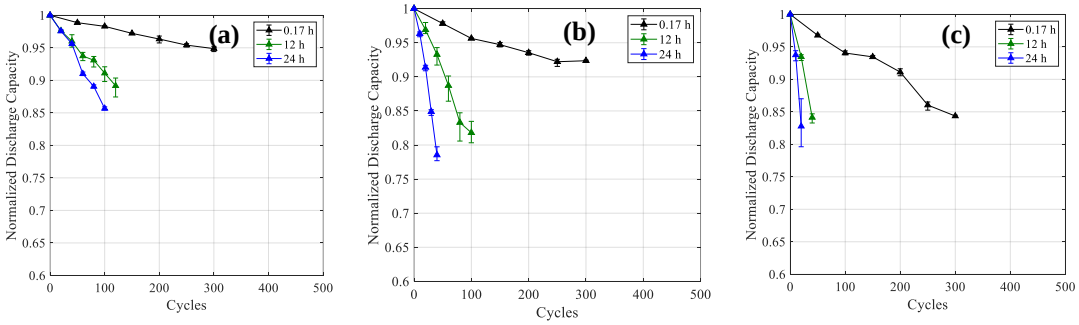

**Figure 6.7.** Normalized discharge capacity vs cycles for Manufacturer E at a) 35 $^{o}$C, b) 45 $^{o}$C, and c) 55 $^{o}$C.

### *6.2.2 Rest Time and State of Charge*

Increasing the rest time after full charge will affect the average SOC of battery during cycling. Average SOC has been shown to affect the battery degradation in the literature [36][28]. In order to understand the capacity fade behavior average, SOC values have been calculated for the batteries under different rest time-based cycling conditions using the following equation:

$$\overline{SOC}_n = \frac{1}{T_n}.\int_o^{T_n} SOC(t).dt \tag{6.1}$$

where $\overline{SOC}_n$ is the average SOC, and $T_n$ is the test time for cycle n. SOC(t) is the battery SOC at time t during the cycle n. SOC has been estimated as follows:

$$SOC(t) = \begin{cases} 0 & during\ rest\ after\ full\ discharge\ (I = 0) \\ \frac{\int I(t).dt}{Q_{cn}} & during\ charging\ (CC\ and\ CV)\ process \\ \frac{V(t)-2.596}{1.804} & during\ rest\ after\ full\ charge\ (I = 0,\ V \geq 4.35V) \\ \frac{V(t)-3.161}{1.222} & during\ rest\ after\ full\ charge\ (I = 0,\ V < 4.35V) \\ SOC(t_{SOD}) - \frac{\int I(t).dt}{Q_{cn}} & during\ discharging\ (CC)\ process \end{cases} \tag{6.2}$$

where I(t) is the magnitude of battery current, and V(t) is the battery terminal voltage at time t. $Q_{cn}$ is the charge capacity during cycle n. The time of the start of discharge during cycle n is represented as $t_{SOD}$. During the cycling tests (Table 6.1), rest after full discharge is fixed at 0.17

h, and the SOC during this period is assumed to be zero. During the charge/discharge process, the SOC has been calculated using standard Coulomb counting method. At the end of the charge process—defined as a reduction in charge current up to C/20 during the CV phase except for the float test—the terminal voltage has been considered as an approximation to open-circuit voltage (OCV). A piecewise linear curve fit between OCV-SOC test data (at 30 $^{o}$C) above 80% SOC is used for estimating approximate SOC during rest after full charge operation.

In Equation (6.1), the integration term is also of interest as it represents SOC weighted total time of each cycle and contain the information of the SOC vs time relation during the entire cycle. It can be defined as follows:

$$t_{SOC,n} = \int_{o}^{T_n} SOC(t).dt = \overline{SOC}_n * T_n \tag{6.3}$$

In order to capture the entire SOC vs time operation of batteries, the % ratio of total time spent by batteries between a SOC range to the total testing time is plotted vs different SOC ranges in the increments of 5% between 0% and 100% SOC. Figure 6.8 shows that distributions of time over SOC ranges follow similar shapes, with the mode occurring in the 95%-100% SOC range for all the tests except the 360 h test. While Figure 6.8 has been drawn using the raw data of one of the samples for each test condition, other tested samples under same rest time condition also show closely similar profiles. The % of time spent in the 95%-100% SOC range increased as the rest time is increased from 0.17 h (~17%) to 24 h (~88%). However, the batteries under 360 h test did not follow this increasing trend and spent roughly equal % of time in the 95%-100% SOC range as by those under 0.17 h rest condition. The mode for open storage test occurred in the 90%-95% SOC range. The batteries under 360 h test spent ~70% less time in the 95%-100% SOC range compared to those under 24 h rest condition. This distribution of

time over SOC ranges presents an interesting overview of how the combination of rest time and number of cycles can be used to increase or decrease the exposure of battery to high SOC region.

Figure 6.8 also shows average SOC and SOC weighted total cycle time, $t_{SOC}$, parameters for the first cycle. It was observed that the average SOC mostly increases with the number of cycles, however, the change remains less than 5% for all the cycling tests during the entire testing. For a given rest time condition, the average SOC values for all the samples remain within 2% across all the temperatures. Equation (6.2) does not define the average SOC for batteries under float tests as they continue to charge beyond the C/20 charge cut-off threshold used as a marker for 100% SOC. Average SOC increases with an increase in the rest time after full charge condition. The 0.17 h test case has the lowest average SOC of ~53%, and the 24 h test case has an average SOC of ~92%. However, the difference between the average SOC values of 24 h rest condition and 360 h (open storage) condition is less than 1% despite a large difference in rest periods after full charge.

Contrary to the variation in average SOC with cycles, SOC weighted total cycle time remains almost constant over cycles. Over cycles as the battery degrades, average SOC parameter increases due to longer constant voltage phase and cycle time, $T_n$ (Equation (3)), decreases keeping the value of $t_{SOC,n}$ nearly constant. Value of SOC weighted total cycle time also remains constant across different battery samples and temperatures for the same rest time condition. Hence this parameter can be tied to specific open rest duration and used to explain the effects of open rest time condition.

Figure 6.8 also provides interesting insights on whether cycles are playing any role in the degradation. Batteries under 360 h test spent 100% of their time above 90%, while this % goes down to ~24% for batteries under 0.17 h rest condition Since exposure to higher SOC for longer durations promote more degradation, the 360 h test is expected to have higher capacity fade

rate compared to the 0.17 h rest test. Still, the batteries under 0.17 h rest condition show higher capacity fade rate in Figure 6.3b compared to that under 360 h test confirming the role of number of cycles in the degradation of batteries under 0.17 h rest condition. Charge-discharge operations resulted into the temperature rise of the batteries up to 7 $^{o}$C above the ambient temperature during each cycle.

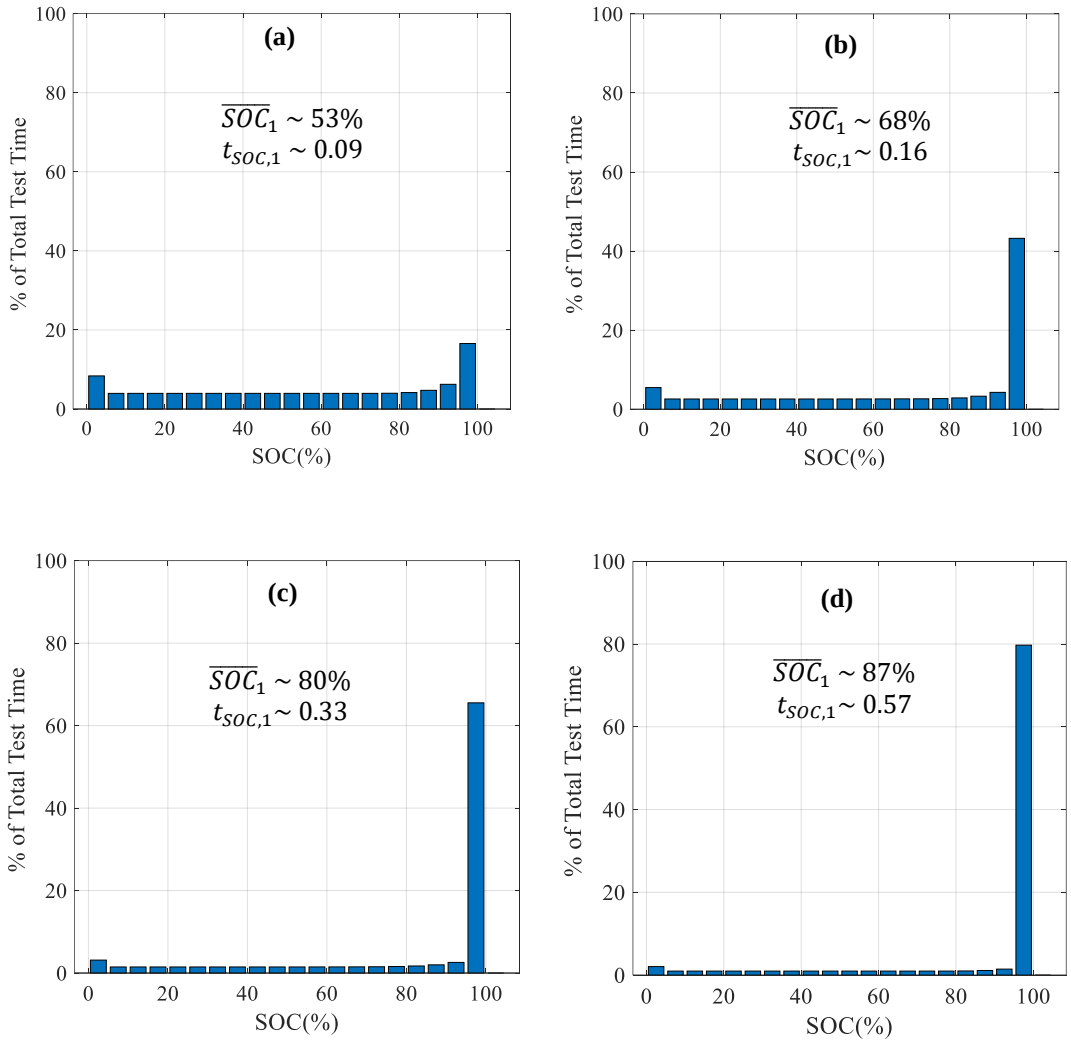

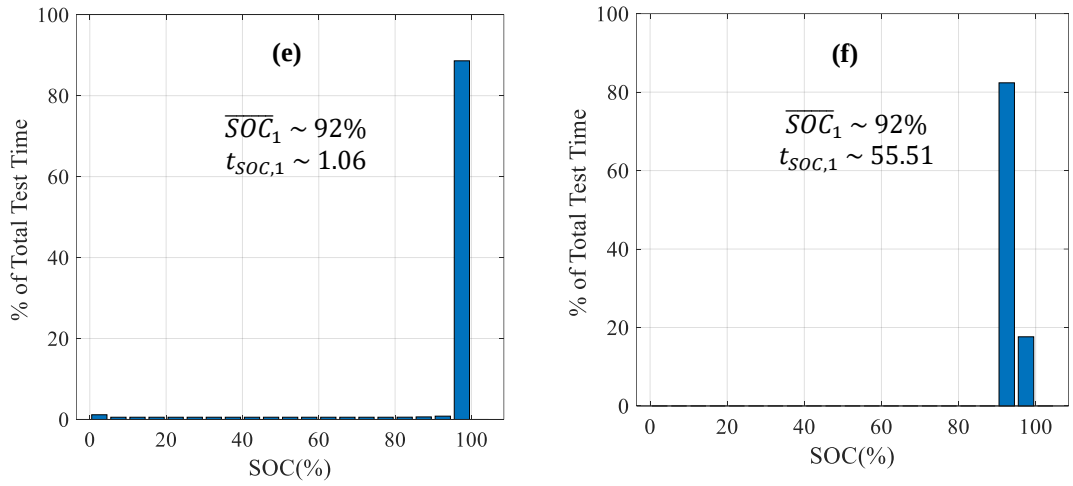


**Figure 6.8.** Distribution of time over different SOC ranges in the increments of 5% for tests with rest times of a) 0.17 h, b) 2 h, c) 6 h, d) 12 h, e) 24 h, and f) 360 h at 45 $^{o}$C.

## 6.3 Capacity Fade Trend Modeling

In the cycle testing of batteries with different ambient temperatures and rest times, the capacity fade data can be plotted either in terms of the number of cycles or test time (days). However, the number of cycles is more relevant from the perspective of determining the mechanical degradation in the batteries. Based on the observation of all normalized discharge capacity *vs* cycles plots (Figures 6.2 and 6.3), the batteries do not exhibit a two-stage degradation process with a clear knee point [35]. Rather, their capacity loss shows an approximately linear trend with cycles suggesting a constant degradation rate, γ, for a given test condition. An empirical curve fit for the capacity fade data can be considered as follows:

$$\frac{\Delta C}{C_o} = \gamma n^{\alpha} \tag{6.4}$$

where $C_o$ is the initial capacity (Ah), $\Delta C$ is the capacity loss (Ah), $\gamma$ is the degradation rate, and n is the number of cycles. If the hypothesis of constant degradation rate is true, then $\alpha$ should be close to 1. Mechanical degradation such as particle cracking, if present, or interface layer cracking is expected to promote further chemical degradation in the form of a side-reaction between the electrodes and electrolyte. The constant degradation rate, $\gamma$, can be considered as the measure of chemical degradation in each cycle, which should be a function of ambient temperature, $T$, and battery SOC during the cycle and the per-cycle time parameters. The expected chemical degradation mechanisms including SEI layer formation on the negative electrode and cobalt dissolution on the positive electrode at high voltages (4.3 V *vs* Li) operation [23] are electrochemical in nature and can be represented by exponential dependency between the degradation rate, $\gamma$, and the reciprocal of the ambient temperature, $T$. In order to capture the entire SOC vs time relation, SOC weighted total cycle time, $t_{SOC,n}$ can be used. A linear relationship between capacity fade and average SOC has been suggested in [36] for graphite – $LiCoO_2$ batteries and the capacity fade with time is also close to linear in Figures 6.2 and 6.3. Hence $\ln(\gamma)$ can be modeled using a linear equation as follows:

$$\ln(\gamma) = a + \frac{b}{T} + c.\ln\left(t_{SOC,n}\right) \tag{6.5}$$

$$\ln\left(\frac{\Delta C}{C_o}\right) = a + \frac{b}{T} + c.\ln\left(t_{SOC,n}\right) + \alpha.\ln\left(n\right) \tag{6.6}$$

Since test matrix (Table 6.1) was conducted at different points in time, on probably different lots, and by using different characterization intervals and hence the battery degradation observations for a given test may have some correlation between them. A random intercept model was chosen, where model parameter $a$ could vary across different tests considering

variations in capacity measurements, ambient temperatures, and batteries. The random intercept model can be described as follows:

$$\ln\left(\frac{\Delta C_{ij}}{C_{o_{ij}}}\right) = a + r_i + \frac{b}{T_{ij}} + c.\ln\left(t_{SOC,n,ij}\right) + \alpha.\ln\left(n_{ij}\right) + e_{ij} \quad (6.7)$$

$$r_i \sim N(0, \sigma_r^2), \qquad e_{ij} \sim N(0, \sigma_e^2)$$

where $\Delta C_{ij}$ is the capacity loss for jth battery in the ith test; $r_i$ is the test random effect for intercept; and $e_{ij}$ is the individual battery residual. $r_i$ and $e_{ij}$ are independent of each other. The float test data was not used for fitting as SOC could not be defined as per Equation (6.2). The value of $t_{SOC,n}$ parameter remains nearly constant over cycles for a given rest time condition and hence this constant value represented by $t_{SOC}$ parameter for all the samples under same rest time condition was used for the model fitting. Using random intercept model across test number variable, i, following equation for $\gamma$ can be obtained where the fixed effect of intercept, $a$, has been shown:

$$\ln\left(\frac{\Delta C}{C_o}\right) = 16.52 - \frac{7007.2}{T} + 0.89 * \ln(t_{SOC}) + 1.02 * \ln(n) \quad (6.8)$$

$$\gamma = 1.50 \times 10^7 * (t_{SOC})^{0.89} * \exp\left(-\frac{7007.2}{T}\right)$$

$$\sigma_r = 0.35, \qquad \sigma_e = 0.11$$

The random intercept model can fit all the experimental data well (adjusted $R^2 \sim 0.98$) for the cycling and open storage tests. The 95% confidence interval for $\sigma_r$ is [0.26, 0.50], which does

not include 0 indicating the statistical significance of random effect term. Figure 6.9 compares fitted curves (dashed lines) vs test data (solid lines). It can be observed that model fitting results in a value of parameter α close to 1, confirming the constant degradation rate. As per [41], [42], the constant degradation rate can emanate from kinetically limited electrochemical degradation mechanisms including SEI layer formation and cobalt dissolution. Hence the model also provides certain inference on the nature of mechanisms in the batteries. Value of parameter *b* becomes slightly less compared to the linear (b = 1) relation suggested in [36].

Characterization cycles, which have same profile as 0.17 h test, were not counted for the model fit as they were conducted at room temperature and would result in negligible degradation. Number of characterization cycles in any of the tests did not exceed 30, which would translate to less than 1% degradation (capacity fade at 30 cycles under 25 $^{o}$C, 0.17 h test in Figure 4a). In 360 h test, 4 characterization cycles would translate to ~0.15% of capacity fade. In 360 h test, battery voltage continues to drop for the entire testing of 60 days similar to an open storage test resulting in varying degradation rate between each characterization interval of 360 h. Hence while fitting the model, 360 h test has been considered as one cycle test with 60 days of rest time after full charge considering an average constant degradation rate of $\gamma_{av}$ throughout the test.

The mean equation of the random intercept degradation model described in Equation (6.8) has been used to fit the mean (3 samples) capacity fade data from graphite/$LiCoO_2$ batteries from the four manufacturers. While fitting a constant degradation rate has been assumed by fixing the value of α equal to 1. All the fits (Figure 6.9c, d, e and f) provided decent adjusted $R^2$ values of 0.70, 0.96, 0.86, 0.96, indicating good generalization capabilities of model across commercial batteries from different manufacturers.

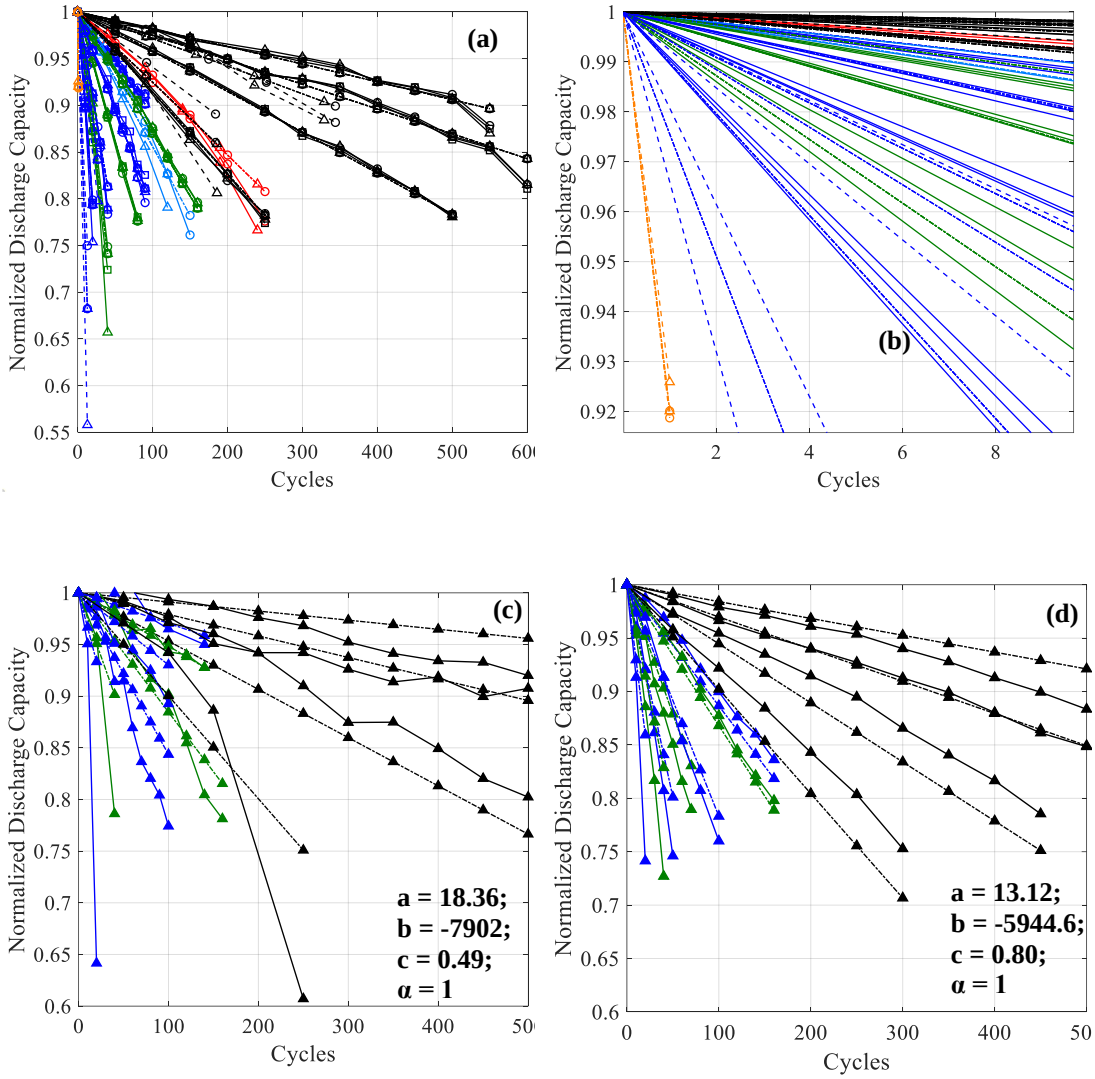
(a)
Normalized Discharge Capacity
Cycles
(b)
Normalized Discharge Capacity
Cycles
(c)
a = 18.36;
b = -7902;
c = 0.49;
α = 1
Normalized Discharge Capacity
Cycles
(d)
a = 13.12;
b = -5944.6;
c = 0.80;
α = 1
Normalized Discharge Capacity
Cycles

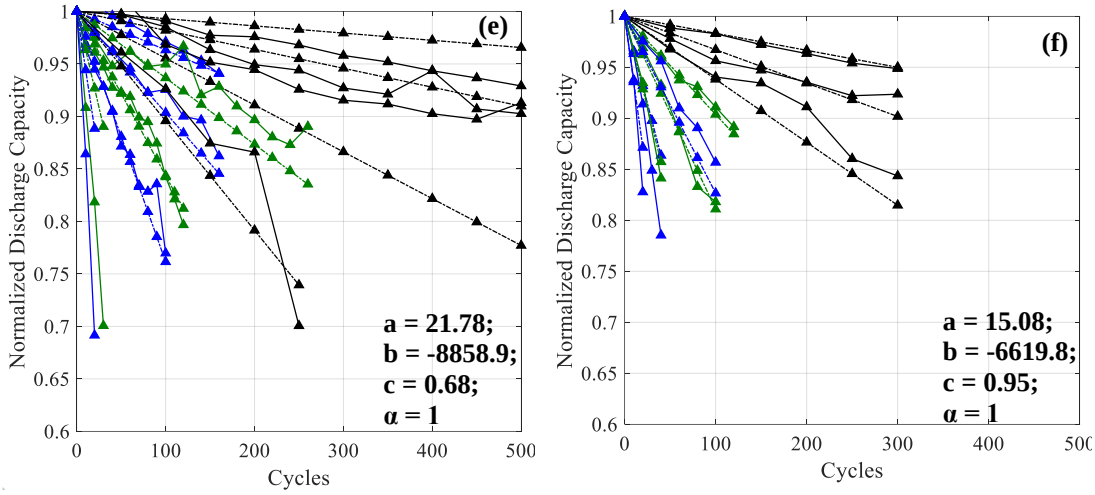


**Figure 6.9.** Normalized discharge capacity vs cycles plots for actual (- and -- lines) and fitted (-.- lines) trends. a) Manufacturer A all tests using random intercept model (Equation (8)), b) zoomed-in plot for Manufacturer A, (c) Manufacturer B (d) Manufacturer C, (e) Manufacturer D, and (f) Manufacturer E.

## 6.4 Implications of Test Results

The results from this study prove that the rest time after charge affects the graphite/$LiCoO_2$ battery capacity fade rate and the effects of rest time are a function of temperature. Considering the wide-scale applicability of graphite/$LiCoO_2$ batteries especially in portable electronic devices like smartphones and laptops, the results are significant for the development of battery management system algorithms and the accelerated battery qualification test programs. Capacity fade trends from this study also highlight the rapid capacity fade of state-of-the-art 4.4 V end-of-charge voltage rated commercial graphite/$LiCoO_2$ batteries. Figure 6.2b shows that if these batteries are used in an electronic device and are kept at 25 $^{o}$C for an open rest

duration of 24 h after full charge, they will lose ~9% of their capacity in less than 4 months. At 35 $^{o}$C, another reasonably expected operating temperature for portable devices, this capacity loss can rise to ~20%. Even for the best performing batteries from Manufacturers B and D, the capacity loss at 35 $^{o}$C, 24 h condition is ~10% in just 4 months. As more and more portable electronic device manufacturers adopt these batteries due to their higher energy density, the long-term performance degradation of these batteries still cannot match with the expected usage life of the devices.

From battery management algorithm design point of view, the results show that the user behavior of keeping the electronic devices connected to charger for long durations such as 24 h will not accelerate the degradation of the batteries compared to user behavior of immediately removing the electronic device from charger after the battery is fully charged as long as the devices are being operated close to 25 $^{o}$C – 35 $^{o}$C temperature range. However, if the devices are kept plugged-in to charger for long durations at elevated temperatures such as 45 $^{o}$C or higher, then the battery degradation rate will increase. These elevated temperature conditions can occur in portable devices due to the internal electronics heating or in vehicles being charged outside in the daylight. Hence the battery management algorithm will have to allow the discharge of batteries to some extent even while plugged-in to limit the exposure of battery to high SOC regions (Figure 6.8) for long durations.

Accelerated battery qualification testing is used to reduce the testing time and is of great value to the industry in the continually shrinking product development cycle. The results from this study show that open rest time condition can be used to accelerate the capacity fade rate of batteries. While the increase in open rest time after full charge always reduced the number of cycles to reach a threshold capacity loss, its effects on reduction in test time were only observable at elevated temperatures of 45 $^{o}$C and 55 $^{o}$C. The open rest time of 24 h after full charge can reduce the test time by more than a month compared to 0.17 h rest time at 45 $^{o}$C. At

55 $^{o}$C, 24 h rest condition can cause the capacity degradation up to 20% in just 20 days significantly reducing the testing time.

The study also confirmed the applicability of temperature and float condition to accelerate the battery testing. Using model Equation (6.8), acceleration factors corresponding to temperature and rest time can be determined. Since batteries from all the manufacturers follow constant capacity fade rate with respect to cycles (α = 1), acceleration factors can be obtained by calculating the ratio of degradation rate, γ, at different stress conditions as follows:

$$AF_{Temp} = \frac{\gamma_{T_a}}{\gamma_{T_b}} = \exp\left(-7007.2 * \left(\frac{1}{T_a} - \frac{1}{T_b}\right)\right) \tag{6.9}$$

$$AF_{rest} = \frac{\gamma_{rest_a}}{\gamma_{rest_b}} = \left(\frac{t_{SOC,a}}{t_{SOC,b}}\right)^{0.89} \tag{6.10}$$

where AF represents the acceleration factor in terms of reduction in number of cycles and *a* and *b* subscripts refer to accelerated and normal (base) levels of stress.

# Chapter 7: Failure Analysis

Failure analysis of cell samples conducted to understand the effects of rest time on degradation mechanisms. Analysis included differential voltage analysis of full cell to non-destructively infer the individual electrode degradation causes, cell disassembly, X-ray diffraction (XRD) to understand electrode structural degradation and to identify nature of possible surface depositions, scanning electron microscopy (SEM) to inspect surface morphologies of electrodes, and energy dispersive X-ray spectroscopy (EDX) to identify elemental composition of electrodes and surface deposits.

## 7.1 Differential Voltage Analysis

Differential voltage analysis has been used in the literature to identify degradation mechanisms in Li-ion batteries non-destructively [64]–[68]. This analysis utilizes OCV-Q curves to obtain *dV/dQ* curves, which are characterized by the Y-axis of *dV/dQ* and the X-axis of Q, capacity (Ah). *dV/dQ* curves show peaks associated with phase transition in electrode materials as a function of state of lithiation of electrodes [65]. As the battery degrades, features such as location of the peaks, distance between the peaks, intensity of the peaks, and presence of the peaks can be used to identify degradation mechanisms associated with the individual electrodes of the battery.

For a full cell, *dV/dQ* curve can be described by the following equation:

$$\frac{dV}{dQ} = \frac{1}{m_p} \cdot \frac{dV_p}{dq_p} - \frac{1}{m_n} \cdot \frac{dV_n}{dq_n} \tag{7.1}$$

where V is the open-circuit voltage of the full cell (volts), Q is the full battery capacity (Ah), $m_p$ is the active mass (g), $V_p$ is the potential (volts) and $q_p$ is the specific capacity ($Ahg^{-1}$) of the positive electrode, $m_n$ is the active mass (g), $V_n$ is the potential (volts) and $q_n$ is the specific capacity ($Ahg^{-1}$) of the negative electrode. In order to prevent the influence of impedance on the voltage curve features and obtain a good approximation to OCV of the cell, charge and discharge currents of the order of C/20 or lower have been recommended [65], [67], [68]. However, the measurement data at slow charge/discharge rates is very noisy and hence smoothing operation is required to obtain clear features/peaks on the *dV/dQ* curves [65], [69]. In this study, the *dV/dQ* curves have been obtained from the charging voltage curves with 1 Hz of sampling frequency, and the smoothing was conducted using the method proposed in [69], which combines the moving average method with the Gaussian filter. The sizes of the moving average window and Gaussian filter window were chosen as 1500 and 500, respectively, based on a trial-and-error method to prevent lack of clarity of features (under-smoothing) and loss of features (over-smoothing).

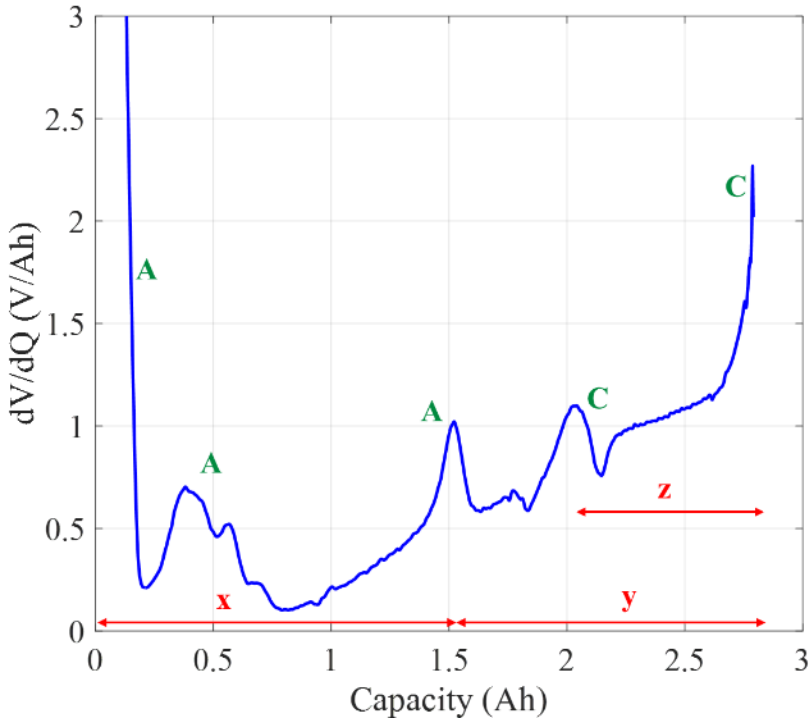


**Figure 7.1.** *dV/dQ* curve of a fresh full cell with individual electrode peaks.

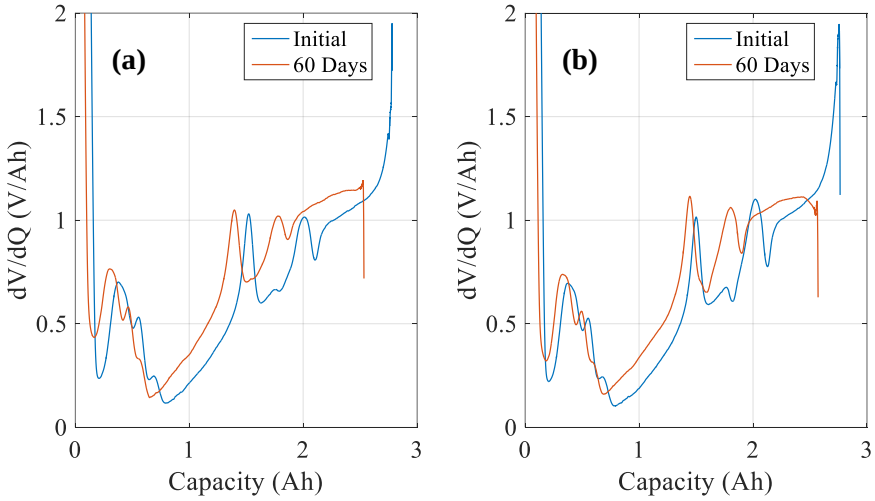

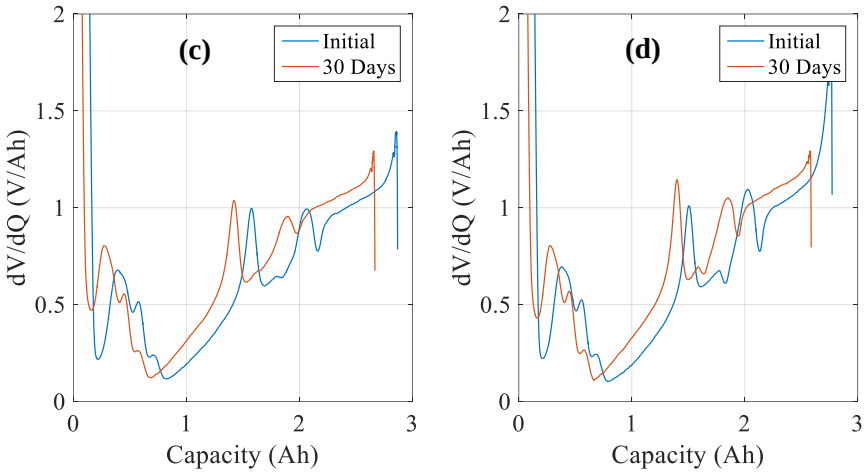
(c)
Initial
30 Days
dV/dQ (V/Ah)
Capacity (Ah)


(d)
Initial
30 Days
dV/dQ (V/Ah)
Capacity (Ah)

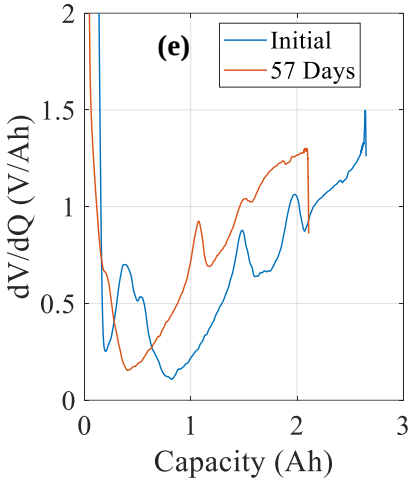
(e)
Initial
57 Days
dV/dQ (V/Ah)
Capacity (Ah)

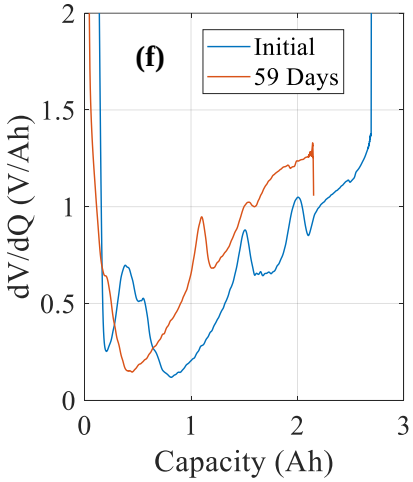
(f)
Initial
59 Days
dV/dQ (V/Ah)
Capacity (Ah)

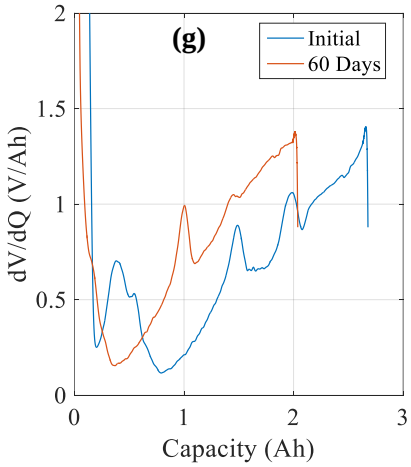
(g)
Initial
60 Days
dV/dQ (V/Ah)
Capacity (Ah)

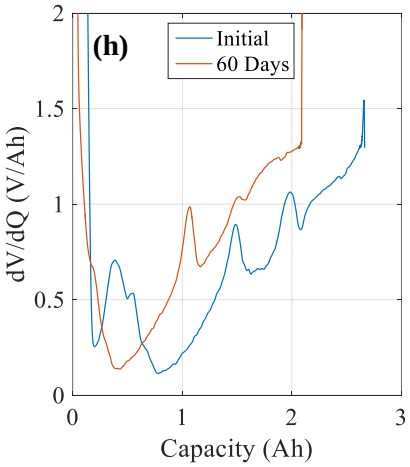
(h)
Initial
60 Days
dV/dQ (V/Ah)
Capacity (Ah)

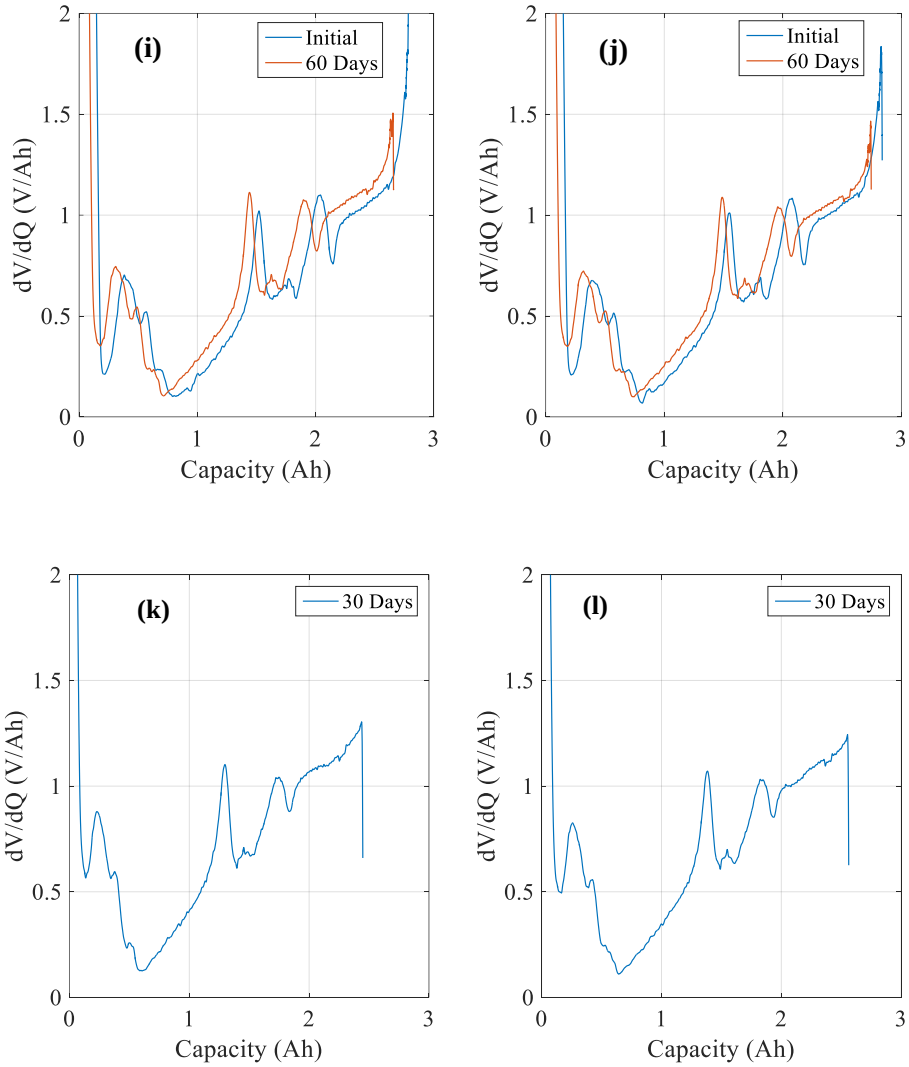


**Figure 7.2.** *dV/dQ* curves for samples under + and * tests at 45 ºC using C/20 and C/10 charge data, respectively: (a) 10 minutes - sample 1, (b) 10 minutes - sample 2, (c) 24 hour - sample 1, (d) 24 hour - sample 2, (e) 2 hour - sample 1, (f) 2 hour - sample 2, (g) 6 hour - sample 1, (h) 6 hour - sample 2, (i) 360 h – sample 1, (j) 360 h – sample 2, (k) 240 h (float) – sample 1, (l) 240 h (float) storage – sample 2.

Due to the wide applicability of graphite/$LiCoO_2$ batteries, the *dV/dQ* curves of individual electrodes (half cells) are easily available in the literature [64], [68] and can be used to understand the *dV/dQ* curves of the full cells employed in this study. The *dV/dQ* curve of full cell shows three distinct peaks (A, A, C) in addition to the start of charge process (A) and end of charge (C) as shown in Figure 7.1. 'A' refers to peaks or features corresponding to anode or negative electrode and 'C' refers to features associated with the cathode or positive electrode. The distance between these peaks/features represented by *x*, *y* and *z* in Figure 7.1 can indicate the individual electrode capacity loss and side-reactions [67]. The distance *x* between two farthest peaks/features 'A' represents the negative electrode (graphite) capacity. Similarly, the distance *z* between two 'C' marked peaks/features represents the positive electrode ($LiCoO_2$) capacity. The distance *y* between 'A' and 'C' marked peaks/features represents the relative shifting of the voltage curves of the two electrodes and indicates capacity loss due to side-reactions. These three distances can be used to compare fresh and degraded electrodes under different rest time conditions.

Figures 7.2 and 7.3 show the *dV/dQ* curves of batteries under + and * tests at the beginning and at the end of the testing to study the battery degradation mechanisms except for 240 h (float) test for which the initial data was not collected due to a human error. The end of the testing has been decided based on 60 days of testing or drop to roughly 80% of initial capacity at C/2 discharge rate for at least 1 sample, whichever occurred earlier. While C/20 has been used for obtaining the charge curves for batteries under '+' tests, a higher current of C/10 was used for 2 tests cases marked by '*' due to planning error. A higher charge current can lead to shift in peak positions due to the impedance effects as well as to the loss of some features. However, C/10 charge curve can still provide some useful features on *dV/dQ* curve after the application of smoothing method [69] with a smaller window size/s (moving average window – 750, Gaussian filter window – 500) compared to that used for the C/20 charge curves.

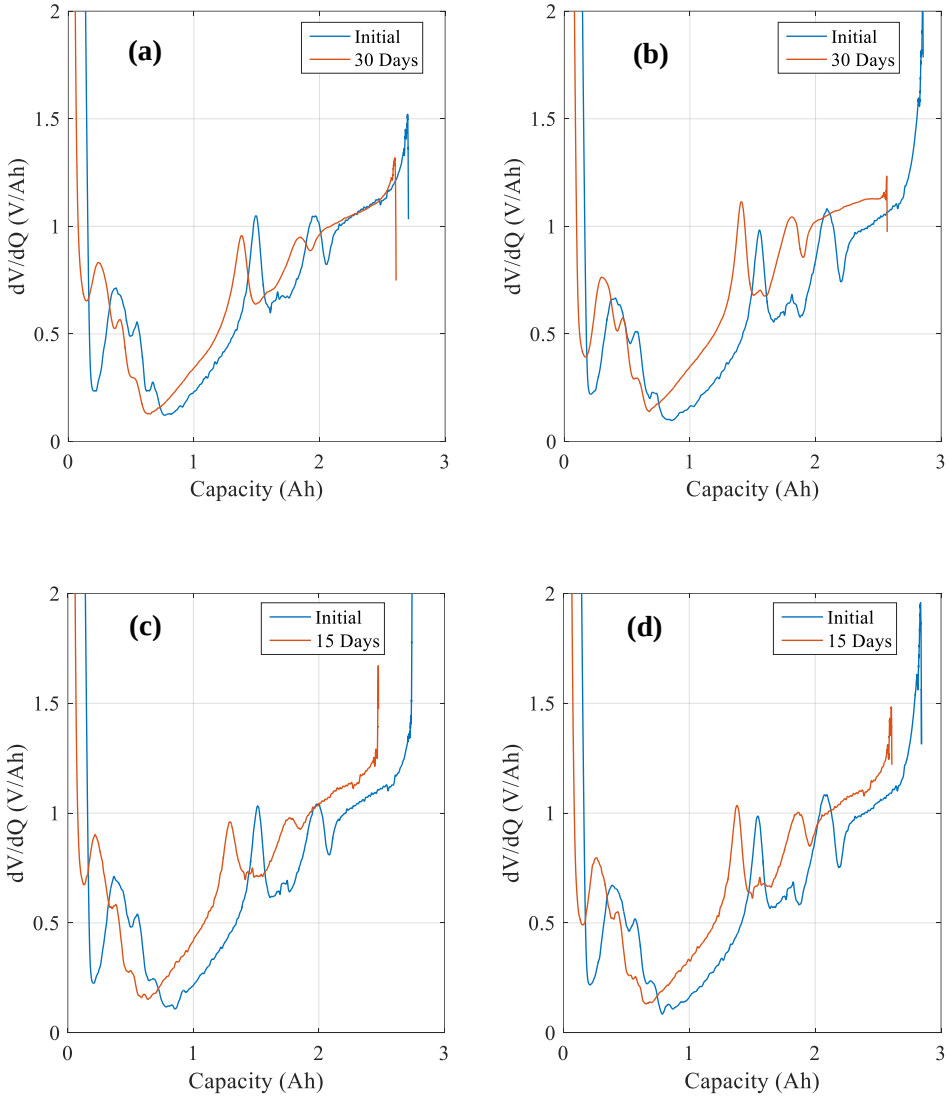


**Figure 7.3.** *dV/dQ* curves for samples under + tests at 55 $^{o}$C using C/20 charge data: (a) 10 minutes - sample 1, (b) 10 minutes - sample 2, (c) 24 hour - sample 1, (d) 24 hour - sample 2.

Figures 7.4 and 7.5 compare the average (2 samples) reductions in distances *x*, *y* and *z* per day for different tests. These reductions have been normalized with respect to time considering the differences in the total test durations among the tests (Table 2). The bar heights in Figure 7.4

cannot be compared with those in Figure 7.5 due to the differences in the C-rates used to obtain OCV-Q curves for. It can be observed that for 0.17 h rest and 360 h tests change in *z* distance is roughly zero indicating no significant active material loss on the positive electrode. However, the active material loss of positive electrode was higher for rest duration of 24 h and 240 h (float). While batteries under 24 h test are charged back to 4.4 V after just 24 h of rest and a full cycle, the 240 h (float) test always maintains the battery voltage at 4.4 V. Hence longer exposure to high state of charge regions (close to 4.4 V) accelerated the positive electrode degradation. 360 h test despite having a longer rest duration allowed the battery voltage to drop during the entire testing similar to an open storage test and thus minimizing the damage to the positive electrode. For all the tests except 45 $^{o}$C, 0.17 h rest reduction in the *x* distance was highest suggesting the battery degradation was dominated by the active material loss of the negative electrode. This loss of active material of the negative electrode was increased by 24 h rest, float condition, and higher temperature of 55 $^{o}$C.

The shift in electrode balancing changing the active lithium ion inventory (reduction in *y* distance) was observed in the all the test cases. 45 $^{o}$C, 2 h and 6 h tests exhibited a reduction in all three distances indicating active material loss in both the electrodes and shift in the electrode balancing. For these two tests as well the battery degradation was dominated by the negative electrode active material loss.

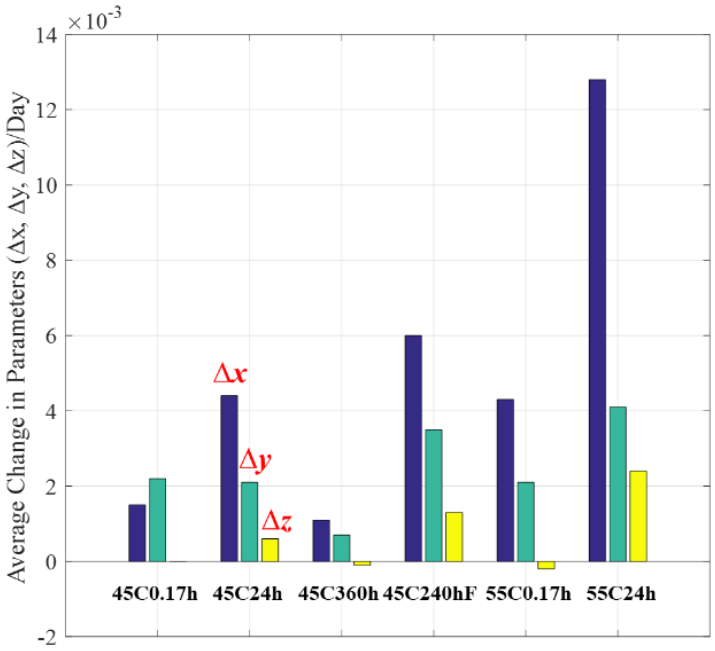


**Figure 7.4.** Change in *x*, *y* and *z* parameters for different test conditions at 45 °C and 55 °C.

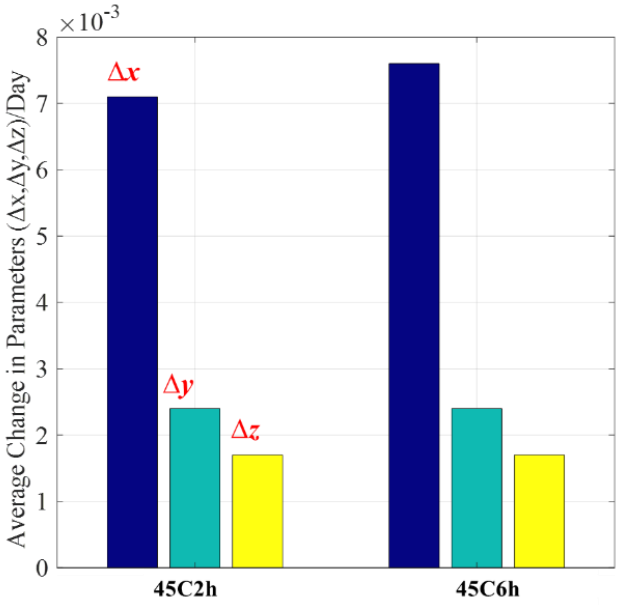


**Figure 7.5.** Change in *x*, *y* and *z* parameters for different test conditions at 45 °C 2 h and 6 h.

## 7.2 Disassembly Procedure

Battery disassembly was conducted to prepare electrode samples for the XRD, SEM and EDX analysis. Before the disassembly, the batteries were discharged at room temperature (25 ± 3 $^{o}$C) up to their manufacturer specified end-of-discharge voltage of 3 V using the 0.5C discharge current. The discharge process was conducted to reduce the energy stored in the battery and prevent any hazardous situation such as thermal runaway during the disassembly procedure. After the discharge process batteries were transferred to an Argon filled glovebox with regulated oxygen (< 3 ppm) and moisture (< 0.5 ppm) content to prevent any reactions of lithium metal and electrolyte salt. Glovebox also adds an extra layer of safety between the operator and the battery during the disassembly process.

The batteries used in this study were pouch batteries with soft polymeric outer jacket (casing) which can be easily cut by a scissor. On the side of the pouch batteries, this jacket contains extra loose material and a seam where the polymeric jacket is vacuum-heat-sealed during the battery manufacturing process. This loose jacket area on one of the sides of the battery was cut using a scissor to open the outer jacket. The jacket was carefully removed to expose the electrode stack of battery wrapped in the separator. This battery had a stack design of electrode with 15 separate pieces of each negative and positive electrodes coated with active material on both the sides. The positive and negative electrodes were arranged in alternate fashion with separator providing the insulation between them.

Once the electrode stack wrapped in the separator was taken out of the outer jacket, the separator sheet was unrolled to obtain the negative electrode and the positive electrode pieces. While removing the separator, caution should be taken to use minimum force to prevent the transfer of material from electrodes to separator or vice versa. Small pieces (~2 cm × 2 cm,

roughly the size of a penny) of both the negative and positive electrodes were cut out from different locations inside the battery and were used for the XRD, SEM and EDX analysis.

## 7.3 X-ray Diffraction Technique

Electrode pieces from disassembled samples were scanned under X-ray diffraction (XRD) machine. A Bruker D8 Advance x-ray powder diffractometer with a LynxEye position sensitive detector was used for these measurements. The X-ray source was a CuKα sealed x-ray tube with a wavelength of 1.5406 Å. Each scan was from 8-70 2θ, with a 0.02 step size and a 0.3 time per step with no rotation of sample. Rietveld refinements were carried out using Bruker TOPAS software. XRD is a useful tool for studying the bulk electrode degradation and identifying damage to electrode crystal structure and presence of amorphous or crystalline films on top of the electrodes. XRD analysis confirmed that the negative electrode was graphite with P63/mmc structure and positive electrode was $LiCoO_2$ with $R\bar{3}m$ hexagonal structure.

Figure 7.6 shows the spectra for the electrodes from fresh and degraded samples. Fresh here refers to the samples from "as received" battery which had undergone formation cycles and had been stored for probably months (~3.77 V) without any charge-discharge operation. On negative electrode, peaks corresponding to graphite and copper current collector were observed. On the positive electrode peaks corresponding to $LiCoO_2$ and $Al_2O_3$ were observed. $Al_2O_3$ was observed on top of most of the positive electrode and possibly came from the $Al_2O_3$ coated separator side facing the positive electrode. In Figure 7.6 c, d, g, h, k and l, peaks corresponding to graphite and $LiCoO_2$ have been zoomed-in to understand the effects of degradation on electrode active materials. It is clear from Figure 7.6 c, g and k that the peaks for graphite in fresh and degraded samples lie at the same angle indicate no changes in crystal symmetry. However, the intensity of the peak decreases possibly due to the deposits on top of the negative electrode. Since no new peaks were observed in the XRD diffractograms of

degraded negative electrodes except for the one from 45 $^{o}$C, 24 h test, the deposits are possibly made of amorphous materials. The extra peak in the negative electrode sample from 45 $^{o}$C, 24 h test did not match with any compound in the XRD software database.

On the positive electrode side, the changes in the $LiCoO_2$ peak are characterized by both the reduction in intensity and shift for degraded samples (Figure 7.6 d, h and l). The reduced intensity indicates the possibility of interfacial reaction products on the positive electrode as well. Rietveld refinements were additionally used to quantify damage in terms of lattice parameters and confirm if the peaks were able to fit with graphite and $LiCoO_2$ lattice structure. In hexagonal crystal structures only *a* and *c* lattice constants are defined. For graphite negative electrode, *a* and *c* parameters for degraded cells do not change significantly from those of fresh cell and remain within $\pm$ 0.01 range. For $LiCoO_2$ positive electrode, parameter *a* remains roughly constant, however there is a discernible change in the *c* parameter which corresponds to interlayer distance in the $LiCoO_2$ structure. The degraded sample showed increase in the *c* parameter as compared to that in the fresh samples (Figure 7.7) and increase is highest at 55 $^{o}$C, 24h test case. However, this increase may be associated with the lesser lithium content [22] in the degraded positive electrode even in the discharge state (0.5C discharge to 3 V) due to the impedance related polarization.

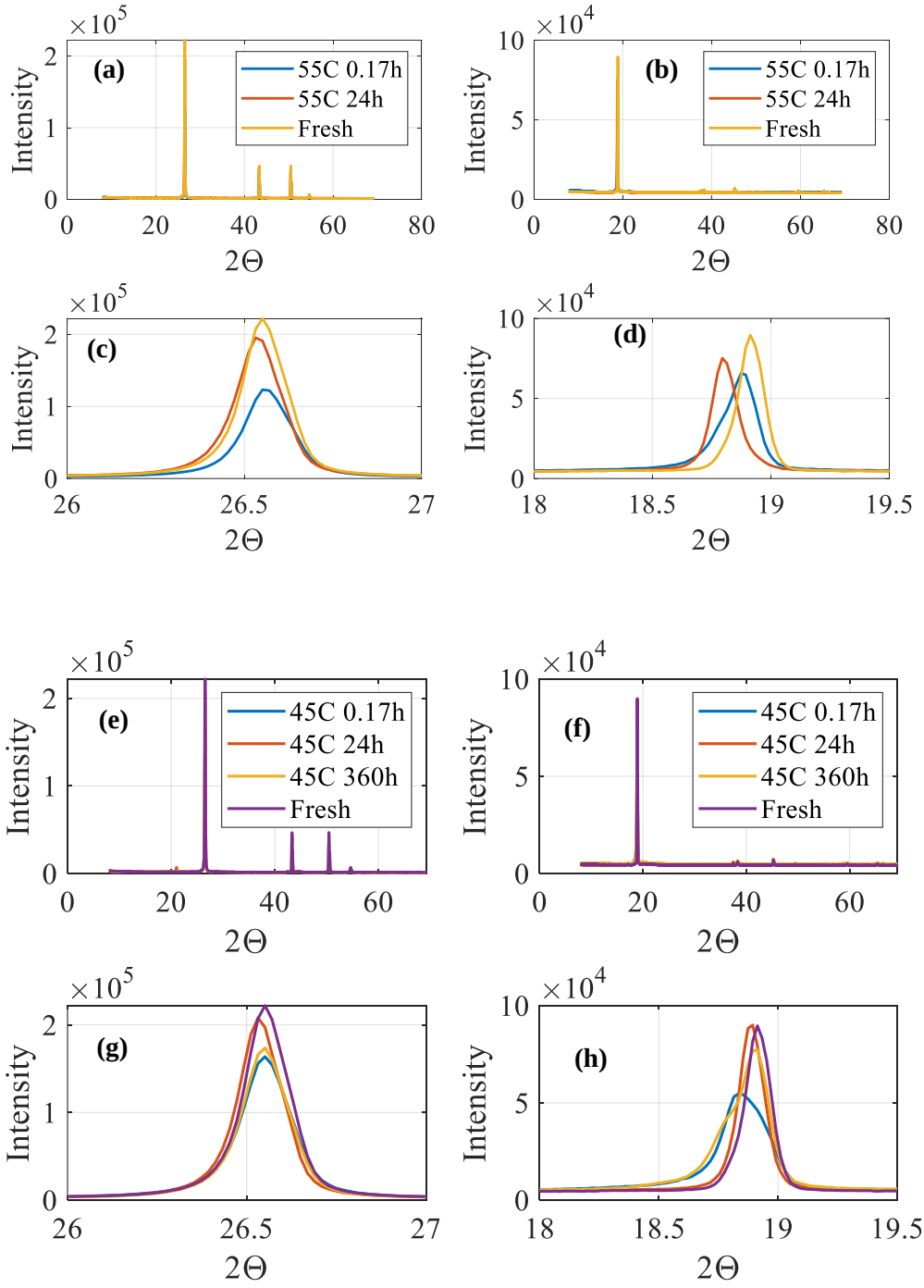
(a)
55C 0.17h
55C 24h
Fresh
Intensity
2Θ
(b)
55C 0.17h
55C 24h
Fresh
Intensity
2Θ
(c)
Intensity
2Θ
(d)
Intensity
2Θ
(e)
45C 0.17h
45C 24h
45C 360h
Fresh
Intensity
2Θ
(f)
45C 0.17h
45C 24h
45C 360h
Fresh
Intensity
2Θ
(g)
Intensity
2Θ
(h)
Intensity
2Θ

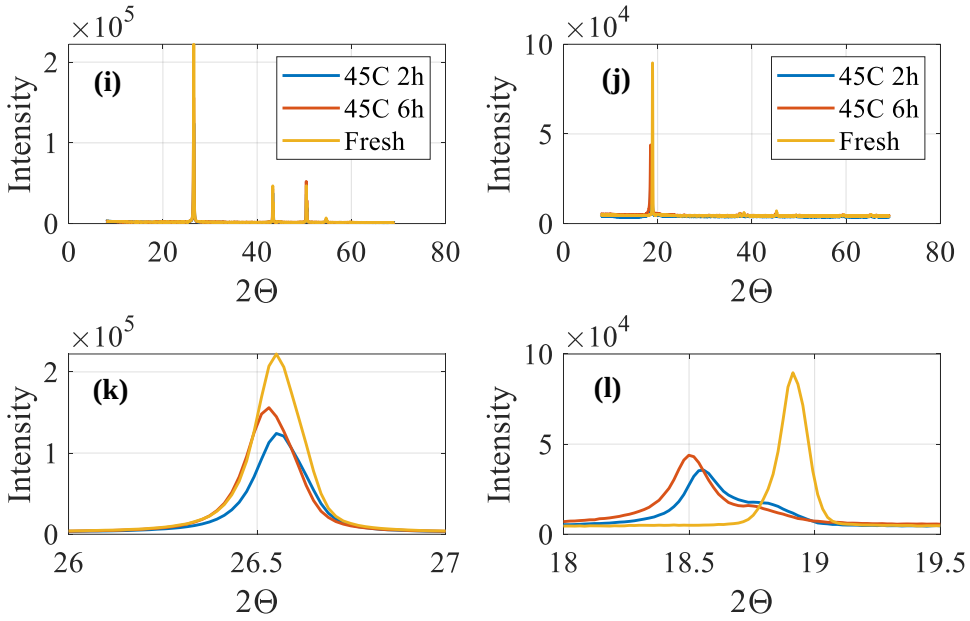


**Figure 7.6.** XRD patterns for the electrodes of sample 1 under + and * tests and fresh sample after disassembly in the fully discharged state: a, e, i) full patterns of negative electrode for different tests, b, f, j) full patterns of positive electrode for different tests, c, g, k) zoomed-in peak of graphite in negative electrode, d, h, l) zoomed-in peak of $LiCoO_2$ in positive electrode.

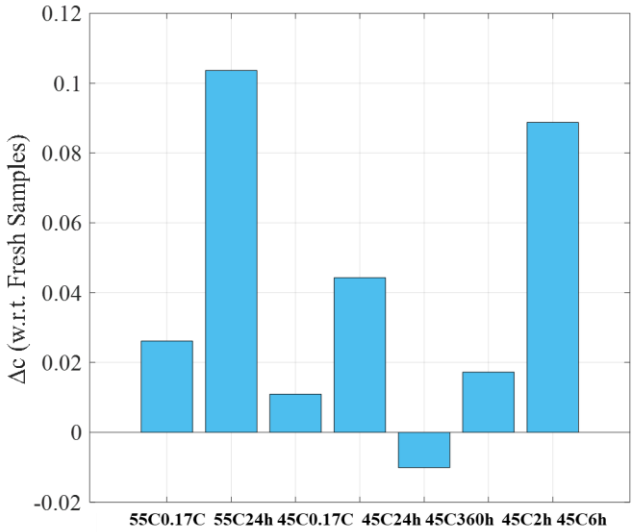


**Figure 7.7.** Change in the c parameter of $LiCoO_2$ lattice.

## 7.4 Scanning Electron Microscopy – Energy Dispersive X-ray Spectroscopy

This study uses the secondary electron mode of SEM in combination with EDX, to identify changes in the surface morphologies and elemental compositions of degraded electrodes compared to that of fresh (as received) samples. After the battery disassembly, 2 pieces (~2 cm × 2 cm, roughly the size of a penny) of each electrode from 2 different locations inside the battery were cut out and observed under SEM and EDX. Since only negative electrode samples of degraded batteries showed variations in surface morphologies compared to fresh one, 1 whole negative electrode piece (~7.1 cm × 3.8 cm) from the electrode stack of the degraded batteries was taken out and observed thoroughly in all directions at more than 10 locations under the SEM.

SEM images of the negative electrode of the fresh battery show graphite particles (Figure 7.8a, b). Brighter fine particles were observed on top of the darker graphite particles (Figure 7.8b), which also showed presence of aluminium (Al) in EDX. A comparison of these particles with the SEM images of the separator (Figure 7.9) showed their resemblance with the $Al_2O_3$ coating of the separator indicating the transfer of coating particles to the negative electrode. While a great care was taken to separate the negative electrode and separator, it is not clear if this transfer of coating particles occurred before or during the disassembly. The EDX spectrum of negative electrode (Figure 7.8c) showed the presence of carbon (C), oxygen (O), copper (Cu), fluorine (F), phosphorous (P), sulfur (S), and aluminium (Al).

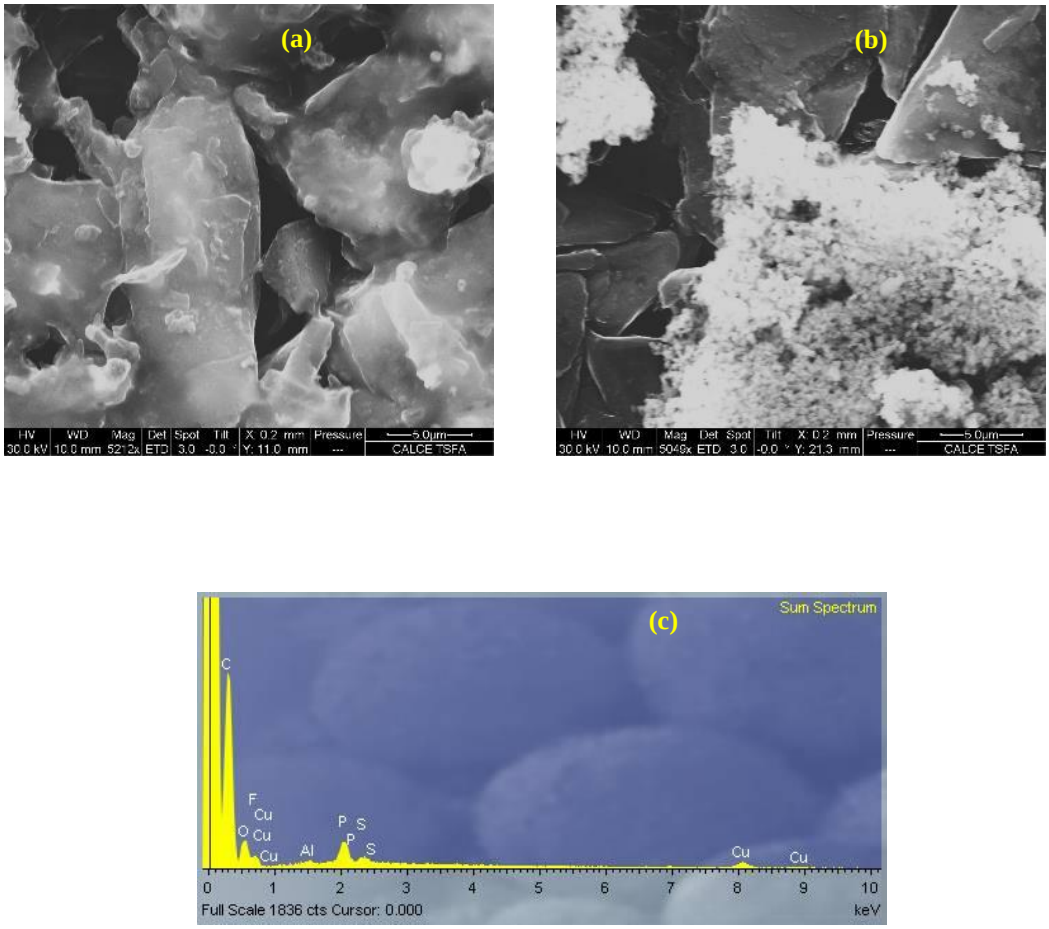


**Figure 7.8.** a) and b) SEM images of negative electrode samples and c) EDX spectrum of negative electrode sample from a fresh battery.

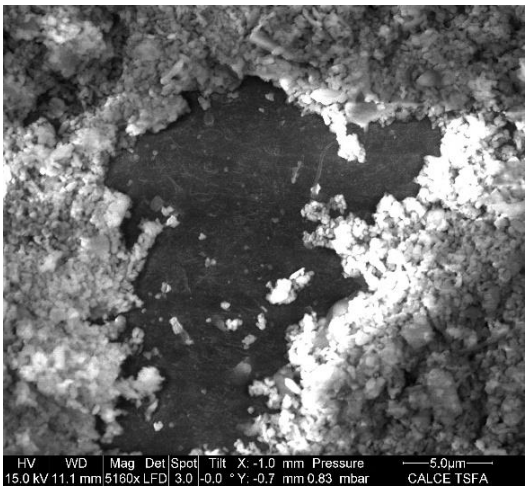

**Figure 7.9.** An SEM image of the separator showing the areas with and without the $Al_2O_3$ coating.

Figures 7.10-7.12 show the SEM images of negative electrodes from degraded batteries under different test conditions. The brighter particles on top of the relatively darker graphite particles indicate the deposits. Within a given SEM image, a multiple point EDX spectrum analysis revealed the presence of aluminium in the brighter particle deposits. A major difference from the fresh samples lied in the level of coverage of these deposits and lack of visibility of clear separation of graphite particles on the degraded negative electrodes. An approximate quantitative analysis in terms of the percentage of negative electrode SEM images where the brighter deposits were distributed over more than 50% of the area of the image showed that this percentage increased from 38% to 83% on increasing the rest time from 0.17 h to 24 h and from 0% to 100% between 360 h to 240 h (float) condition at 45 $^{o}$C. These changes in percentage correlate well with the negative electrode active material loss for the corresponding test in differential voltage analysis results. The deposits can hinder the diffusion paths of lithium ions into the graphite rendering some of the graphite material as inactive and causing the active material loss.

EDX detected the same chemical elements (C, O, Cu, Al, P, F, and S) on all the degraded negative electrode samples as those detected for the fresh one except for one new element of cobalt (Co). The only source of cobalt in the battery is the positive electrode, and hence the results confirm the interfacial reactions between electrolyte and positive electrode, dissolution of cobalt from the positive electrode, and transport of cobalt to the negative electrode. Irrespective of the duration of the rest time after full charge all the degraded samples observed the cobalt dissolution-migration-deposition process. It has been shown in the literature that transition metals like manganese (Mn) can transfer to the negative electrode, disrupt the SEI layer, and aid in the thickening of deposits on the negative electrode leading to rapid capacity

fade of graphite [18]. Hence the interfacial reaction on positive electrode and electrolyte interface are also further promoting the degradation of the negative electrode, which provides a possible explanation for the differential voltage analysis results showing the higher capacity fade of graphite negative electrode compared to that of the $LiCoO_2$ positive electrode in all the degraded samples.

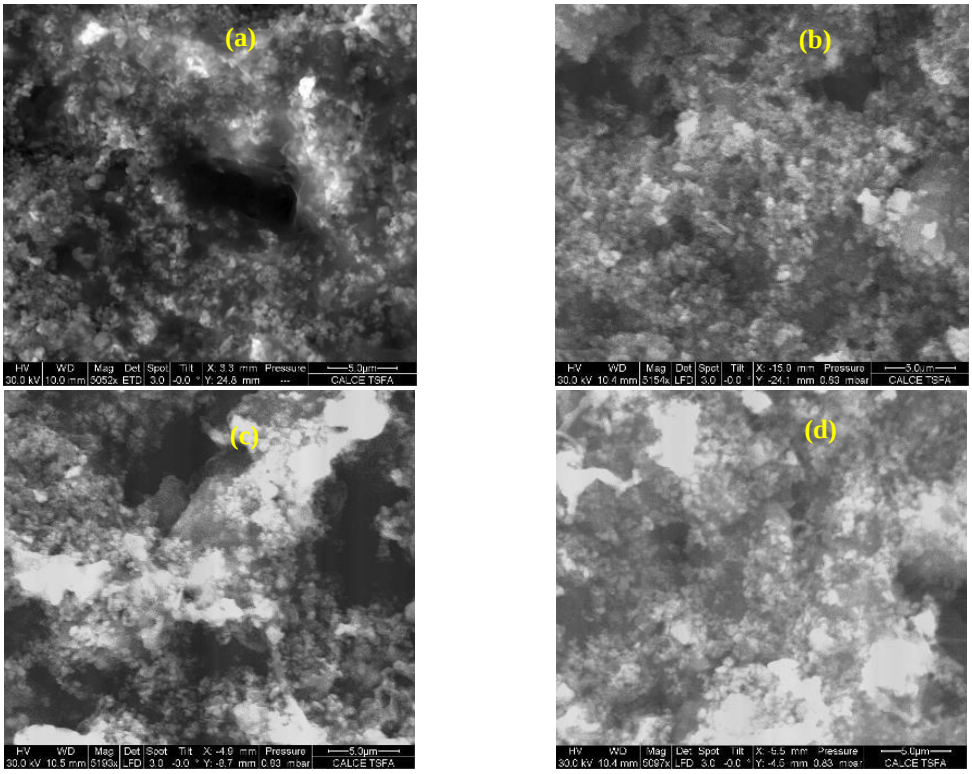


**Figure 7.10.** SEM images of negative electrode samples from a battery tested under a, b) 0.17 h, c), d) 24 h at 55 ºC.

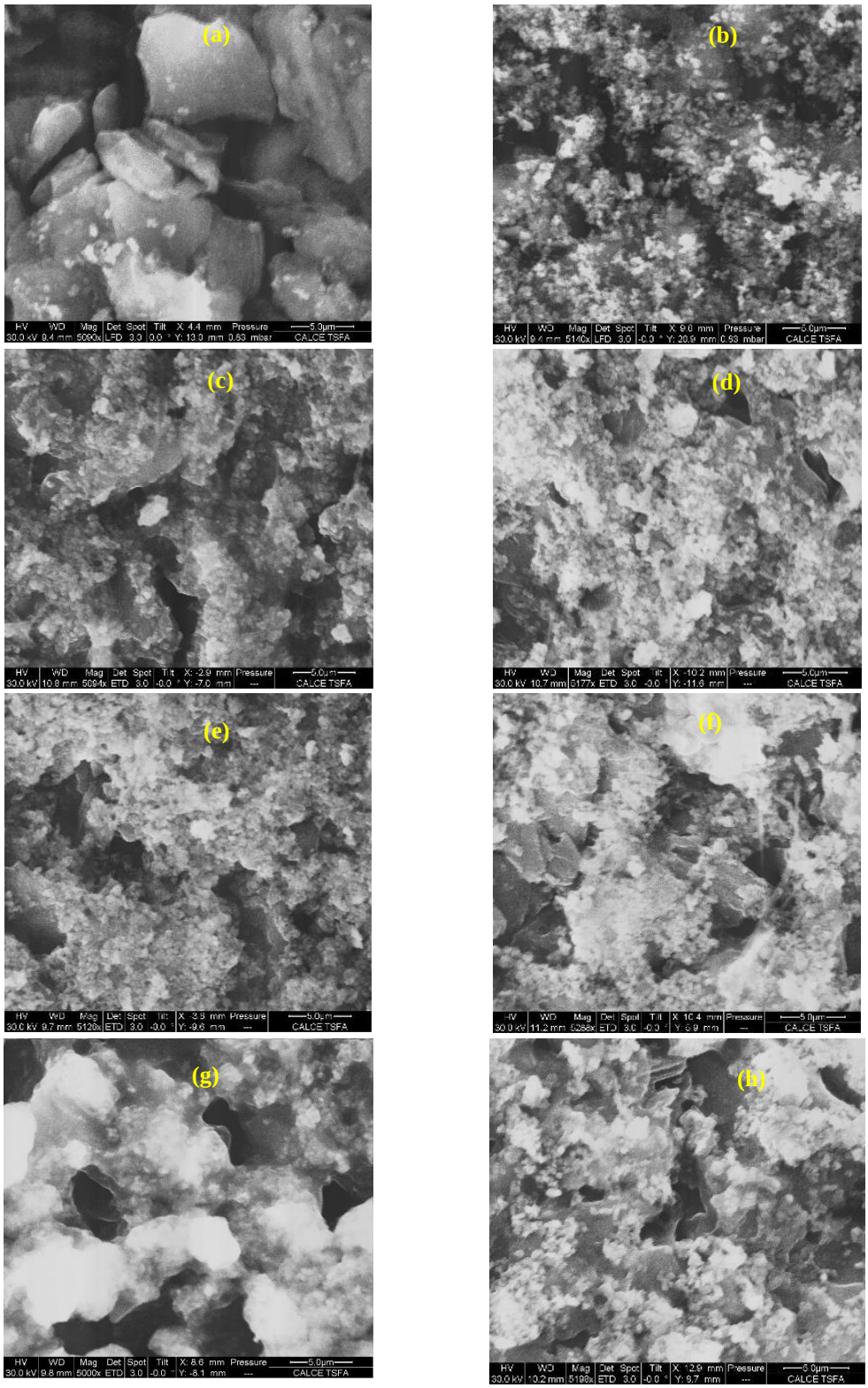


**Figure 7.11.** SEM images of negative electrode samples from a battery tested under a, b) 0.17 h, c, d) 2 h, e, f) 6 h, g, h) 24 h at 45 ºC.

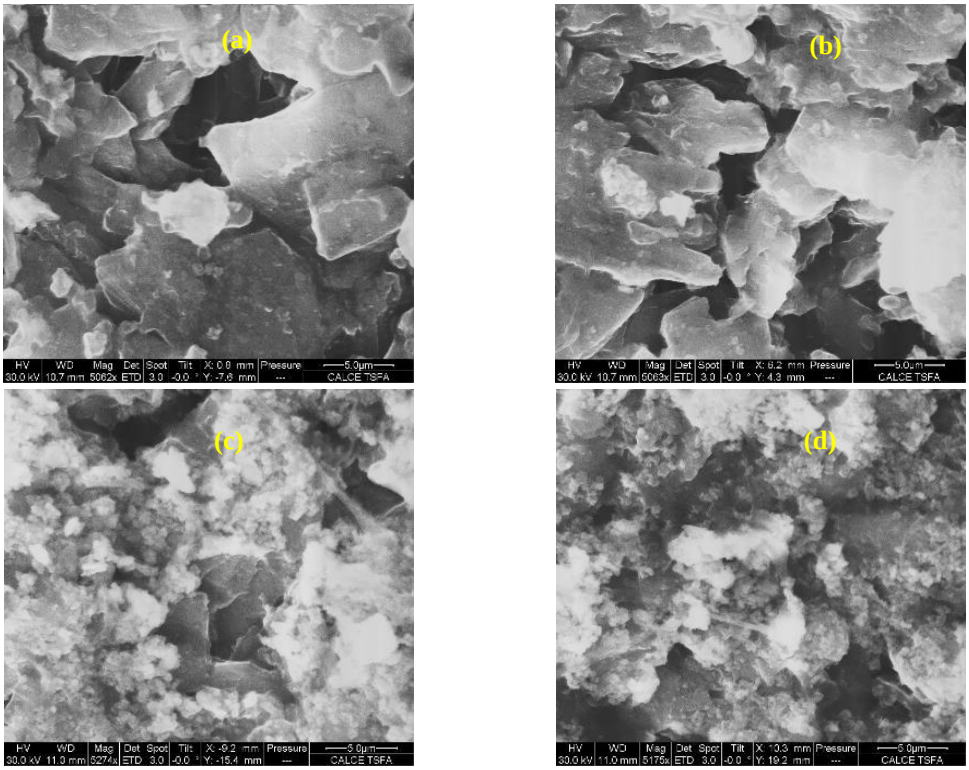


**Figure 7.12.** SEM images of negative electrode samples from a battery tested under a, b) 360 h and c, d) 240 h (float) at 45 ºC.

Figure 7.13 shows SEM images and EDX spectrums of positive electrode samples from fresh batteries. The $Al_2O_3$ residue was found on many of the positive electrode surfaces with particles similar to the coating of the separator (Figure 7.9). The EDX spectrum of positive electrode showed the presence of carbon (C), oxygen (O), cobalt (Co), iron (Fe), aluminium (Al), and phosphorous (P). Iron was present in a very small quantity (<1.5 weight%) and was possibly used for stabilizing the high-voltage operation of $LiCoO_2$.

Figures 7.14 shows SEM images of the degraded positive electrode samples from the batteries under different rest conditions. There was no sign of surface degradation, cracks, or surface deposits on any of the degraded positive electrode. The surfaces with full $Al_2O_3$ particle coverings showed neither $LiCoO_2$ particles nor any relevant degradation information and hence

their SEM images have not been added here. The EDX spectrums of degraded positive electrode samples did not show any new elements compared with those on the fresh positive electrode samples.

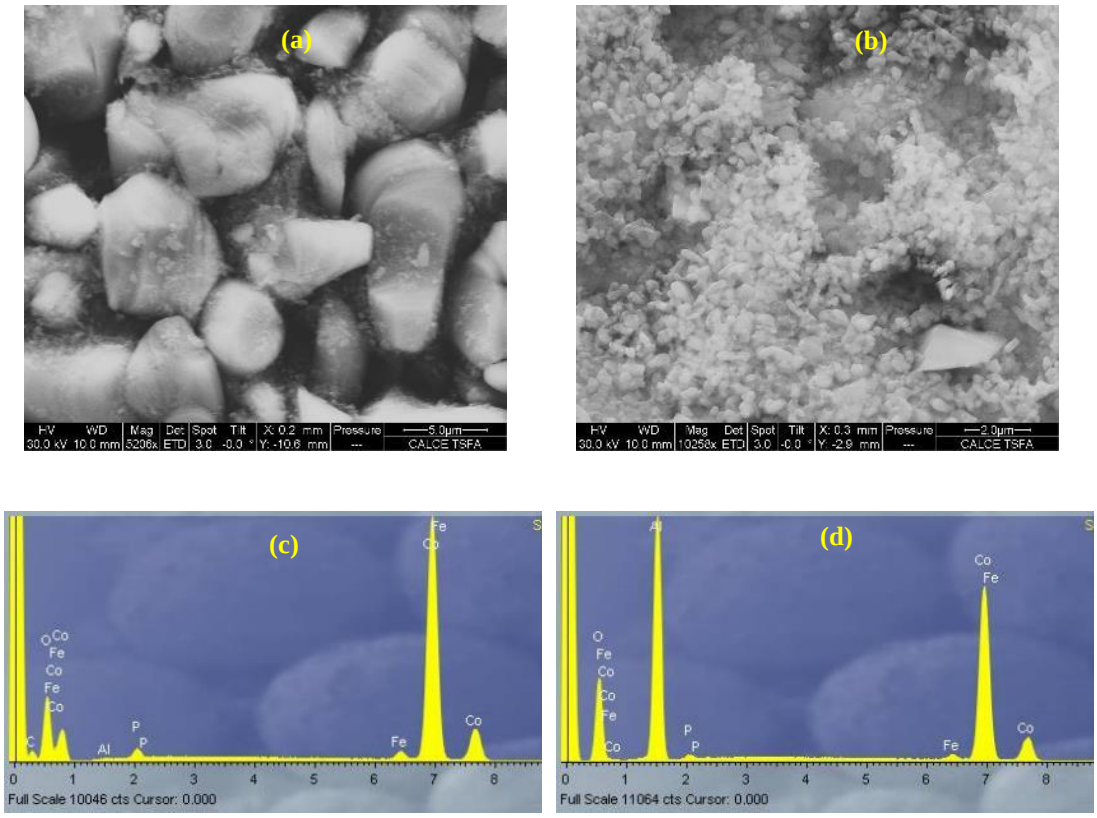


**Figure 7.13.** a, b) SEM images of positive electrode samples and c, d) EDX spectrum of positive electrode samples for fresh (as received) battery.

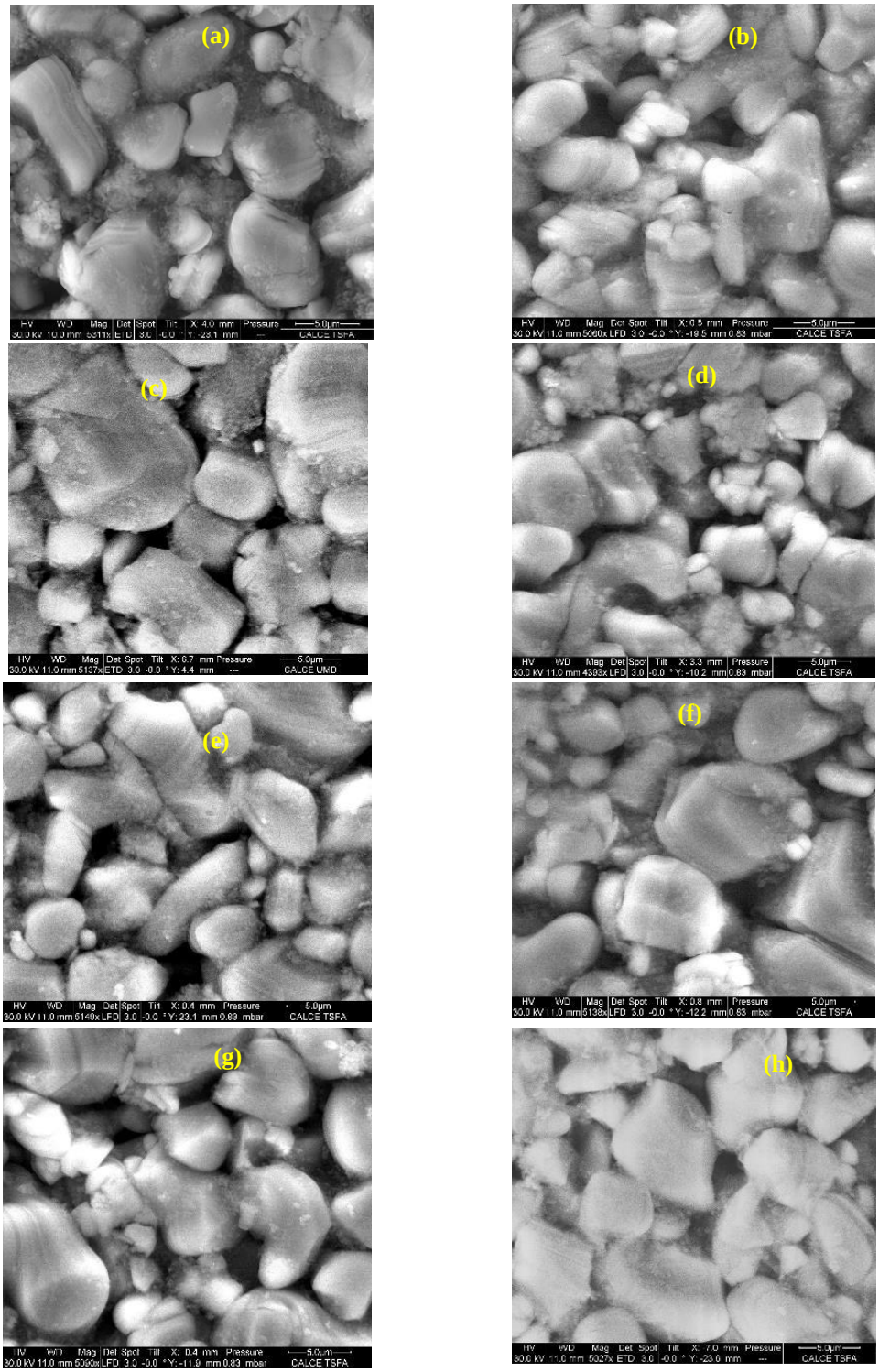


**Figure 7.14.** SEM images of positive electrode samples from batteries tested under a) 55 $^{o}$C, 0.17 h, b) 55 $^{o}$C, 24 h, c) 45 $^{o}$C, 0.17 h, d) 45 $^{o}$C, 24 h, e) 45 $^{o}$C, 2 h, f) 45 $^{o}$C, 6 h, g) 45 $^{o}$C, 360 h, and h) 45 $^{o}$C, 240 h (float) test conditions.

# Chapter 8: Conclusions

This dissertation presents a long-term degradation study on graphite/$LiCoO_2$ commercial pouch batteries to determine the effects of open rest time after full charge on the capacity fade at four different ambient temperatures (25 $^{o}$C, 35 $^{o}$C, 45 $^{o}$C, and 55 $^{o}$C). The results showed that capacity fade per cycle increased monotonically with the increase in the rest time after full charge during the charge-discharge cycling. Increase in the rest time from 0.17 h to 24 h reduced the number of cycles to reach 80% capacity by at least a factor of ~6 at all the tested temperatures above 25 $^{o}$C. However, the capacity fade per day (time), a critical metric for accelerated battery testing, did not monotonically increase with the increase in the rest time. At 25 $^{o}$C, the batteries under 0.17 h and 24 h rest conditions showed negligible difference in their capacity loss after 60 days and at 45 $^{o}$C, batteries under 0.17 h rest showed at least 5% more capacity loss compared to batteries under 360 h rest after 60 days.

An investigation into SOC vs time profiles of batteries under different rest time conditions revealed that an optimal combination of number of cycles and rest time can prolong the exposure of batteries to high SOCs causing more capacity fade. While the batteries with shorter rest duration of 0.17 h underwent more cycles, they spent only 17% of test time in 95%-100% SOC range, which is shorter compared to that (~88%) of batteries under 24 h tests. The batteries under 360 h test with just 4 characterization cycles, a test simulating 360 h, also spent only ~18% of time in the 95%-100% SOC range indicating that longer rest duration at the cost of fewer cycle will not prolong exposure to high SOCs.

The capacity fade had a linear relationship with number of cycles with the constant slope, γ, representing the degradation in each cycle. The slope γ was fitted as a function of temperature (exponential) and SOC weighted total cycle time (power law), a parameter used to describe SOC vs time relation for a given rest time. This model equation was able to describe the experimental data of graphite/$LiCoO_2$ batteries from 5 different manufacturers.

This study utilizes rest time after full charge as an operational parameter to establish a connection between battery continuous cycling (0.17 h) and 360 h operations (360 h) and associated battery capacity fade. It also highlights the performance limitations (~10% capacity loss at 35 $^oC$, 24 h condition in 4 months) the state-of-the-art 4.4 V end-of-charge voltage rated commercial batteries. The implications of this work are pertinent for both the smart battery charging algorithms and battery accelerated test planning. The study shows that keeping the devices plugged-in to charger for long durations such as 24 h will reduce the battery life compared to removing and using the devices immediately after full charge only at the elevated temperatures such as 45 $^oC$ or above. However, this trend will reverse if plugged-in time is continued to increase. More investigation and experimentations with rest durations intermediate to 24 h and 360 h will be required to determine the rest time where this trend reversal takes place. Additionally, it would also be valuable to study the role of rest time after different charge states (<100% SOC) to answer if the accelerating effects of rest periods on capacity fade at elevated temperatures can be completely eliminated using a derated end-of-charge condition.

Degradation mechanisms of graphite/$LiCoO_2$ batteries were investigated using three different techniques. Differential voltage analysis of batteries and a comparison of peak shifts indicated the degradation mechanisms were shift in electrode balancing and active material loss of the electrodes. The battery degradation was dominated by the graphite negative electrode active material loss for all the tests except for the 0.17 h rest at 45 $^oC$ where capacity loss based on

the shift in electrode balancing was more dominant. The $LiCoO_2$ positive electrode active material loss was increased by extending the rest time from 0.17 h to 24 h and raising the temperature. The float condition also accelerated the positive electrode active material loss, while the 360 h condition representing 360 h behavior had a negligible effect.

X-ray diffraction analysis of the degraded electrode samples showed that the peak intensities decreased with respect to the peaks for fresh electrode samples indicating the presence of amorphous deposits. Scanning electron microscopy images showed major surface modifications of only the negative electrodes from degraded batteries. These surface modifications/deteriorations were more pronounced longer rest durations than 0.17 h, and float conditions. Energy dispersive X-ray spectroscopy analysis detected cobalt on the negative electrodes of all the degraded (tested) batteries, confirming the loss of cobalt from the positive electrode and its transport to the negative electrode. Aluminum was also observed in the deposits on top of the negative electrode.

The results from this study confirmed that there was no observable mechanical degradation in the form of surface and bulk electrode particle cracks and the performance of the batteries degraded through chemical degradation mechanisms. Interfacial reactions between electrolyte and positive electrode not only resulted in the loss of its capacity in most degraded batteries but also led to the dissolution of cobalt, which further migrated to the negative electrode and possibly played a role in the surface deposits and higher capacity loss of the negative electrode compared to the positive electrode in all the degraded batteries. Presence of aluminum in the surface deposits of the negative electrodes raises a question on the stability of $Al_2O_3$ separator coating especially at high potentials and will require additional investigation.

# Bibliography


[1] "This Month in Physics History: March 20, 1800: Volta describes the electric battery," *APS News*, 2006. [Online]. Available: https://www.aps.org/publications/apsnews/200603/history.cfm. [Accessed: 19-Mar-2018].

[2] "The market for lithium-ion battery is expected to register a CAGR of approximately 22%, during the forecast period (2019 | Markets Insider." [Online]. Available: https://markets.businessinsider.com/news/stocks/the-market-for-lithium-ion-battery-is-expected-to-register-a-cagr-of-approximately-22-during-the-forecast-period-2019-1028690618. [Accessed: 17-Nov-2019].

[3] "A Behind the Scenes Take on Lithium-ion Battery Prices | BloombergNEF." [Online]. Available: https://about.bnef.com/blog/behind-scenes-take-lithium-ion-battery-prices/. [Accessed: 17-Nov-2019].

[4] "Lithium Ion Battery Market | Size, Share and Market Forecast to 2024 | MarketsandMarkets™." [Online]. Available: https://www.marketsandmarkets.com/Market-Reports/lithium-ion-battery-market-49714593.html. [Accessed: 17-Nov-2019].

[5] J. Christensen and J. Newman, "Stress generation and fracture in lithium insertion materials," *J Solid State Electrochem*, vol. 10, pp. 293–319, 2006, doi:

10.1007/s10008-006-0095-1.

[6] M. Broussely, P. Biensan, F. Bonhomme, P. Blanchard, S. Herreyre, K. Nechev, and R. J. Staniewicz, “Main aging mechanisms in Li ion batteries,” *Journal of Power Sources*, vol. 146, no. 1–2, pp. 90–96, Aug. 2005, doi: 10.1016/J.JPOWSOUR.2005.03.172.

[7] J. Vetter, P. Novák, M. R. Wagner, C. Veit, K.-C. Möller, J. O. Besenhard, M. Winter, M. Wohlfahrt-Mehrens, C. Vogler, and A. Hammouche, “Ageing mechanisms in lithium-ion batteries,” *Journal of Power Sources*, vol. 147, no. 1–2, pp. 269–281, Sep. 2005, doi: 10.1016/J.JPOWSOUR.2005.01.006.

[8] C. Hendricks, N. Williard, S. Mathew, and M. Pecht, “A failure modes, mechanisms, and effects analysis (FMMEA) of lithium-ion batteries,” *Journal of Power Sources*, vol. 297, pp. 113–120, Nov. 2015, doi: 10.1016/J.JPOWSOUR.2015.07.100.

[9] “Voltaiq survey on battery industry finds analytical challenges and resource constraints as major obstacles to product development - Green Car Congress.” [Online]. Available: https://www.greencarcongress.com/2019/06/20190626-voltaiq.html. [Accessed: 17-Nov-2019].

[10] K. Edström, M. Herstedt, and D. P. Abraham, “A new look at the solid electrolyte interphase on graphite anodes in Li-ion batteries,” *Journal of Power Sources*, vol. 153, no. 2, pp. 380–384, Feb. 2006, doi: 10.1016/J.JPOWSOUR.2005.05.062.

[11] H. J. Ploehn, P. Ramadass, and R. E. White, “Solvent Diffusion Model for Aging of Lithium-Ion Battery Cells,” *Journal of The Electrochemical Society*, vol. 151, no. 3, p. A456, Mar. 2004, doi: 10.1149/1.1644601.

[12] E. Peled and S. Menkin, “Review—SEI: Past, Present and Future,” *Journal of The Electrochemical Society*, vol. 164, no. 7, pp. A1703–A1719, Jun. 2017, doi:

10.1149/2.1441707jes.

[13] I. Laresgoiti, S. Käbitz, M. Ecker, and D. U. Sauer, “Modeling mechanical degradation in lithium ion batteries during cycling: Solid electrolyte interphase fracture,” *Journal of Power Sources*, vol. 300, pp. 112–122, Dec. 2015, doi: 10.1016/J.JPOWSOUR.2015.09.033.

[14] J. Christensen and J. Newman, “A Mathematical Model of Stress Generation and Fracture in Lithium Manganese Oxide,” *Journal of The Electrochemical Society*, vol. 153, no. 6, p. A1019, Jun. 2006, doi: 10.1149/1.2185287.

[15] R. Kostecki and F. Mclarnon, “Microprobe study of the effect of Li intercalation on the structure of graphite,” doi: 10.1016/S0378-7753(03)00287-8.

[16] J. B. Goodenough and K. S. Park, “The Li-ion rechargeable battery: A perspective,” *Journal of the American Chemical Society*, vol. 135, no. 4. pp. 1167–1176, 30-Jan-2013, doi: 10.1021/ja3091438.

[17] J. B. Goodenough and Y. Kim, “Challenges for rechargeable Li batteries,” *Chemistry of Materials*, vol. 22, no. 3. pp. 587–603, 09-Feb-2010, doi: 10.1021/cm901452z.

[18] W. Li, B. Song, and A. Manthiram, “High-voltage positive electrode materials for lithium-ion batteries,” *Chemical Society Reviews*, vol. 46, no. 10. Royal Society of Chemistry, pp. 3006–3059, 21-May-2017, doi: 10.1039/c6cs00875e.

[19] M. Gauthier, T. J. Carney, A. Grimaud, L. Giordano, N. Pour, H. H. Chang, D. P. Fenning, S. F. Lux, O. Paschos, C. Bauer, F. Maglia, S. Lupart, P. Lamp, and Y. Shao-Horn, “Electrode-Electrolyte Interface in Li-Ion Batteries: Current Understanding and New Insights,” *Journal of Physical Chemistry Letters*, vol. 6, no. 22. American Chemical Society, pp. 4653–4672, 19-Nov-2015, doi: 10.1021/acs.jpclett.5b01727.

[20] W. Li, A. Dolocan, P. Oh, H. Celio, S. Park, J. Cho, and A. Manthiram, “Dynamic behaviour of interphases and its implication on high-energy-density cathode materials in lithium-ion batteries,” *Nature Communications*, vol. 8, no. 1, pp. 1–10, Apr. 2017, doi: 10.1038/ncomms14589.

[21] R. Imhof and P. Novák, “Oxidative Electrolyte Solvent Degradation in Lithium-Ion Batteries: An In Situ Differential Electrochemical Mass Spectrometry Investigation,” *Journal of The Electrochemical Society*, vol. 146, no. 5, p. 1702, May 1999, doi: 10.1149/1.1391829.

[22] J. N. Reimers and J. R. Dahn, “Electrochemical and In Situ X-Ray Diffraction Studies of Lithium Intercalation in LixCoO2,” *Journal of The Electrochemical Society*, vol. 139, no. 8, p. 2091, Aug. 1992, doi: 10.1149/1.2221184.

[23] G. G. Amatucci, J. M. Tarascon, and L. C. Klein, “Cobalt dissolution in LiCoO2-based non-aqueous rechargeable batteries,” *Solid State Ionics*, vol. 83, no. 1–2, pp. 167–173, Jan. 1996, doi: 10.1016/0167-2738(95)00231-6.

[24] R. V. Chebiam, A. M. Kannan, F. Prado, and A. Manthiram, “Comparison of the chemical stability of the high energy density cathodes of lithium-ion batteries,” *Electrochemistry Communications*, vol. 3, no. 11, pp. 624–627, Nov. 2001, doi: 10.1016/S1388-2481(01)00232-6.

[25] S. S. Choi and H. S. Lim, “Factors that affect cycle-life and possible degradation mechanisms of a Li-ion cell based on LiCoO2,” *Journal of Power Sources*, vol. 111, no. 1, pp. 130–136, Sep. 2002, doi: 10.1016/S0378-7753(02)00305-1.

[26] G. Ning, B. Haran, and B. N. Popov, “Capacity fade study of lithium-ion batteries cycled at high discharge rates,” *Journal of Power Sources*, vol. 117, no. 1–2, pp. 160–169, May 2003, doi: 10.1016/S0378-7753(03)00029-6.

[27] J. Wang, P. Liu, J. Hicks-Garner, E. Sherman, S. Soukiazian, M. Verbrugge, H. Tataria, J. Musser, and P. Finamore, “Cycle-life model for graphite-LiFePO4 cells,” *Journal of Power Sources*, vol. 196, no. 8, pp. 3942–3948, Apr. 2011, doi: 10.1016/J.JPOWSOUR.2010.11.134.

[28] M. Ecker, N. Nieto, S. Käbitz, J. Schmalstieg, H. Blanke, A. Warnecke, and D. U. Sauer, “Calendar and cycle life study of Li(NiMnCo)O 2 -based 18650 lithium- ion batteries,” *Journal of Power Sources*, vol. 248, pp. 839–851, 2014, doi: 10.1016/j.jpowsour.2013.09.143.

[29] J. Wang, J. Purewal, P. Liu, J. Hicks-Garner, S. Soukazian, E. Sherman, A. Sorenson, L. Vu, H. Tataria, and M. W. Verbrugge, “Degradation of lithium ion batteries employing graphite negatives and nickel–cobalt–manganese oxide + spinel manganese oxide positives: Part 1, aging mechanisms and life estimation,” *Journal of Power Sources*, vol. 269, pp. 937–948, Dec. 2014, doi: 10.1016/J.JPOWSOUR.2014.07.030.

[30] T. Guan, P. Zuo, S. Sun, C. Du, L. Zhang, Y. Cui, L. Yang, Y. Gao, G. Yin, and F. Wang, “Degradation mechanism of LiCoO 2 /mesocarbon microbeads battery based on accelerated aging tests,” *Journal of Power Sources*, vol. 268, pp. 816–823, 2014, doi: 10.1016/j.jpowsour.2014.06.113.

[31] D.-I. Stroe, M. Swierczynski, A.-I. Stan, R. Teodorescu, and S. J. Andreasen, “Accelerated Lifetime Testing Methodology for Lifetime Estimation of Lithium-Ion Batteries Used in Augmented Wind Power Plants,” *IEEE Transactions on Industry Applications*, vol. 50, no. 6, pp. 4006–4017, Nov. 2014, doi: 10.1109/TIA.2014.2321028.

[32] Y. Cui, C. Du, G. Yin, Y. Gao, L. Zhang, T. Guan, L. Yang, and F. Wang, “Multi-stress factor model for cycle lifetime prediction of lithium ion batteries with shallow-

depth discharge," *Journal of Power Sources*, vol. 279, pp. 123–132, Apr. 2015, doi: 10.1016/J.JPOWSOUR.2015.01.003.

[33] I. Baghdadi, O. Briat, J.-Y. Delétage, P. Gyan, and J.-M. Vinassa, "Lithium battery aging model based on Dakin's degradation approach," *Journal of Power Sources*, vol. 325, pp. 273–285, Sep. 2016, doi: 10.1016/J.JPOWSOUR.2016.06.036.

[34] Y. Wu, P. Keil, S. F. Schuster, and A. Jossen, "Impact of Temperature and Discharge Rate on the Aging of a LiCoO2 /LiNi0.8Co 0.15Al0.05O2 Lithium-Ion Pouch Cell," *Journal of The Electrochemical Society*, vol. 164, no. 7, pp. A1438–A1445, May 2017, doi: 10.1149/2.0401707jes.

[35] W. Diao, S. Saxena, and M. Pecht, "Accelerated cycle life testing and capacity degradation modeling of LiCoO2-graphite cells," *Journal of Power Sources*, vol. 435, p. 226830, 2019, doi: 10.1016/j.jpowsour.2019.226830.

[36] S. Saxena, C. Hendricks, and M. Pecht, "Cycle life testing and modeling of graphite/LiCoO2cells under different state of charge ranges," *Journal of Power Sources*, vol. 327, 2016, doi: 10.1016/j.jpowsour.2016.07.057.

[37] S. Saxena, Y. Xing, D. Kwon, and M. Pecht, "Accelerated degradation model for C-rate loading of lithium-ion batteries," *International Journal of Electrical Power and Energy Systems*, vol. 107, pp. 438–445, May 2019, doi: 10.1016/j.ijepes.2018.12.016.

[38] M. Doyle, "Modeling of Galvanostatic Charge and Discharge of the Lithium/Polymer/Insertion Cell," *Journal of The Electrochemical Society*, vol. 140, no. 6, p. 1526, 1993, doi: 10.1149/1.2221597.

[39] T. F. Fuller, "Simulation and Optimization of the Dual Lithium Ion Insertion Cell," *Journal of The Electrochemical Society*, vol. 141, no. 1, p. 1, 1994, doi: 10.1149/1.2054684.

[40] G. Ning and B. N. Popov, “Cycle Life Modeling of Lithium-Ion Batteries,” *Journal of The Electrochemical Society*, vol. 151, no. 10, p. A1584, Oct. 2004, doi: 10.1149/1.1787631.

[41] F. M. Kindermann, J. Keil, A. Frank, and A. Jossen, “A SEI Modeling Approach Distinguishing between Capacity and Power Fade,” *Journal of The Electrochemical Society*, vol. 164, no. 12, pp. E287–E294, Jan. 2017, doi: 10.1149/2.0321712jes.

[42] J. M. Reniers, G. Mulder, and D. A. Howey, “Review and Performance Comparison of Mechanical-Chemical Degradation Models for Lithium-Ion Batteries,” *Journal of The Electrochemical Society*, vol. 166, no. 14, pp. A3189–A3200, Jan. 2019, doi: 10.1149/2.0281914jes.

[43] “A Designer’s Guide to Lithium Ion (Li-ion) Battery Charging | DigiKey.” [Online]. Available: https://www.digikey.com/en/articles/a-designer-guide-fast-lithium-ion-battery-charging. [Accessed: 30-Apr-2020].

[44] M. Reichert, D. Andre, A. Rösmann, P. Janssen, H.-G. Bremes, D. U. Sauer, S. Passerini, and M. Winter, “Influence of relaxation time on the lifetime of commercial lithium-ion cells,” *Journal of Power Sources*, vol. 239, pp. 45–53, Oct. 2013, doi: 10.1016/J.JPOWSOUR.2013.03.053.

[45] M. Rashid and A. Gupta, “Effect of Relaxation Periods over Cycling Performance of a Li-Ion Battery,” *Journal of The Electrochemical Society*, vol. 162, no. 2, pp. A3145–A3153, Jan. 2015, doi: 10.1149/2.0201502jes.

[46] K. J. Nelson, J. E. Harlow, and J. R. Dahn, “A Comparison of NMC/Graphite Pouch Cells and Commercially Available LiCoO2/Graphite Pouch Cells Tested to High Potential,” *Journal of The Electrochemical Society*, vol. 165, no. 3, pp. A456–A462, Feb. 2018, doi: 10.1149/2.0041803jes.

[47] M. Broussely, S. Herreyre, P. Biensan, P. Kasztejna, K. Nechev, and R. . Staniewicz, "Aging mechanism in Li ion cells and calendar life predictions," *Journal of Power Sources*, vol. 97–98, pp. 13–21, Jul. 2001, doi: 10.1016/S0378-7753(01)00722-4.

[48] J. Christensen and J. Newman, "A mathematical model for the lithium-ion negative electrode solid electrolyte interphase," *Journal of The Electrochemical Society*, vol. 151, no. 11, pp. A1977–A1988, Oct. 2004, doi: 10.1149/1.1804812.

[49] "Introduction to the Generalized Eyring Life-Stress Relationship." [Online]. Available: https://www.weibull.com/hotwire/issue74/relbasics74.htm. [Accessed: 30-Mar-2020].

[50] "8.1.5.2. Eyring." [Online]. Available: https://www.itl.nist.gov/div898/handbook/apr/section1/apr152.htm. [Accessed: 30-Mar-2020].

[51] L. A. Escobar and W. Q. Meeker, "A Review of Accelerated Test Models," *Statistical Science*, vol. 21, no. 4, pp. 552–577, 2006, doi: 10.1214/088342306000000321.

[52] J. C. Pinheiro, D. M. Bates, and J. C. Pinheiro, "Approximations to the Log-Likelihood Function in the Nonlinear Mixed-Effects Model," *Journal of Computational and Graphical Statistics*, vol. 4, no. 1, p. 12, Mar. 1995, doi: 10.2307/1390625.

[53] M. J. Lindstrom and D. M. Bates, "Nonlinear Mixed Effects Models for Repeated Measures Data," *Biometrics*, vol. 46, no. 3, p. 673, Sep. 1990, doi: 10.2307/2532087.

[54] W. Q. Meeker, L. A. Escobar, and C. J. Lu, "Accelerated Degradation Tests: Modeling and Analysis," 1999.

[55] C. J. Lu and W. Q. Meeker, "Using Degradation Measures to Estimate a Time-to-Failure Distribution," *Technometrics*, vol. 35, no. 2, p. 161, May 1993, doi:

10.2307/1269661.

[56] J. P. Royston, “Some Techniques for Assessing Multivarate Normality Based on the Shapiro- Wilk W,” *Applied Statistics*, vol. 32, no. 2, p. 121, 1983, doi: 10.2307/2347291.

[57] S. Korkmaz, D. Goksuluk, and G. Zararsiz, “MVN: An R Package for Assessing Multivariate Normality.”

[58] W. Prochazka, G. Pregartner, and M. Cifrain, “Design-of-Experiment and Statistical Modeling of a Large Scale Aging Experiment for Two Popular Lithium Ion Cell Chemistries,” *Journal of The Electrochemical Society*, vol. 160, no. 8, pp. A1039–A1051, 2013, doi: 10.1149/2.003308jes.

[59] L. Su, J. Zhang, C. Wang, Y. Zhang, Z. Li, Y. Song, T. Jin, and Z. Ma, “Identifying main factors of capacity fading in lithium ion cells using orthogonal design of experiments,” *Applied Energy*, vol. 163, pp. 201–210, 2016, doi: 10.1016/j.apenergy.2015.11.014.

[60] G. James, D. Witten, T. Hastie, and R. Tibshirani, “Linear Regression,” in *An Introduction to Statistical Learning*, Springer New York, 2013, pp. 59–126.

[61] F. Nie, H. Huang, X. Cai, and C. Ding, “Efficient and Robust Feature Selection via Joint 2,1-Norms Minimization,” in *Advances in Neural Information Processing Systems 23 (NIPS 2010)*, 2010.

[62] R. Tibshirani, “Regression Shrinkage and Selection Via the Lasso,” *Journal of the Royal Statistical Society, Series B*, vol. 58, pp. 267--288, 1994.

[63] T. Hastie, R. Tibshirani, and M. Wainwright, *Statistical learning with sparsity: The lasso and generalizations*. CRC Press, LLC, 2015.

[64] K. Honkura and T. Horiba, “Study of the deterioration mechanism of LiCoO2/graphite cells in charge/discharge cycles using the discharge curve analysis,” *Journal of Power Sources*, vol. 264, pp. 140–146, Oct. 2014, doi: 10.1016/j.jpowsour.2014.04.036.

[65] I. Bloom, A. N. Jansen, D. P. Abraham, J. Knuth, S. A. Jones, V. S. Battaglia, and G. L. Henriksen, “Differential voltage analyses of high-power, lithium-ion cells 1. Technique and application,” *Journal of Power Sources*, vol. 139, no. 1–2, pp. 295–303, Jan. 2005, doi: 10.1016/j.jpowsour.2004.07.021.

[66] H. Kato, Y. Kobayashi, and H. Miyashiro, “Differential voltage curve analysis of a lithium-ion battery during discharge,” *Journal of Power Sources*, vol. 398, pp. 49–54, Sep. 2018, doi: 10.1016/j.jpowsour.2018.07.043.

[67] P. Keil and A. Jossen, “Calendar Aging of NCA Lithium-Ion Batteries Investigated by Differential Voltage Analysis and Coulomb Tracking,” *Journal of The Electrochemical Society*, vol. 164, no. 1, pp. A6066–A6074, Oct. 2017, doi: 10.1149/2.0091701jes.

[68] H. M. Dahn, A. J. Smith, J. C. Burns, D. A. Stevens, and J. R. Dahn, “User-Friendly Differential Voltage Analysis Freeware for the Analysis of Degradation Mechanisms in Li-Ion Batteries,” *Journal of The Electrochemical Society*, vol. 159, no. 9, pp. A1405–A1409, Jan. 2012, doi: 10.1149/2.013209jes.

[69] Y. Li, M. Abdel-Monem, R. Gopalakrishnan, M. Berecibar, E. Nanini-Maury, N. Omar, P. van den Bossche, and J. Van Mierlo, “A quick on-line state of health estimation method for Li-ion battery with incremental capacity curves processed by Gaussian filter,” *Journal of Power Sources*, vol. 373, pp. 40–53, Jan. 2018, doi: 10.1016/j.jpowsour.2017.10.092.